UNIVERSITÀ DEGLI STUDI DI NAPOLI "FEDERICO II"

Facoltà di Scienze MM.FF.NN. Dipartimento di Scienze Fisiche

PhD Thesis in Fundamental and Applied Physics

XXIV Cycle - November 2011

Mitigation of Laser Beam Perturbations in the Virgo and Advanced-Virgo Gravitational Waves Detectors

Coordinator:

Prof. Raffaele Velotta

Supervisor:

Dr. Enrico Calloni

Author:

Maria Parisi

to Fabio and

my little jewel

Contents

Introduction

The present work has been carried out in the frameworks of the Virgo experiment and tha Advanced Virgo (AdV) project, a Virgo detector upgrade to a second generation instrument.

The Virgo experiment is a long 3 Km baseline interferometric antenna for gravitational waves (GWs) detection,located within the site of EGO, European Gravitational Observatory, based at Cascina (Pisa, Italy).

Gravitational waves were first predicted by Einstein's Theory of General Relativity, published in 1918. These waves are perturbations in the curvature of space-time propagating at the speed of light. Indirect evidence of their existence has been obtained in 1992 via observations of a binary pulsar system (PSR 1913+16) by Hulse and Taylor.

However, direct detection of gravitational waves has not been obtained yet.

Research is now focused on achieving direct detection of gravitational waves, giving a new way of observing astronomical events in the universe. Gravitational waves are quadrupole in nature, causing tidal strains in space time. The weak nature of gravity means that the magnitude of these strains is very small. Only astrophysical sources are likely to produce waves of sufficient amplitude to be detected on Earth. In the frequency band of a few Hz to a few kHz, the expected strain amplitude for violent sources is of the order of 10^{-22}.

Detection is most likely to be achieved using long baseline interferometers. Currently several such detectors are in operation worldwide, including Virgo , built in a collaboration involving the Italian Institute of Nuclear Physics (INFN) and the French Center National of Recherches Scientific (CNRS). In USA the LIGO detector network has three large interferometric detectors - two interferometers share the same vacuum tube with 4 km and 2 km arms length, and the remaining with 4 km length. In German, the GEO600 a 600 meters long detector is located near Hannover.

Since 2011 Virgo completed four scientific data taking periods (Virgo Science Run -VSR 1 to 4) and the next recent one has been just closed. The first three periods were carried out in partial or complete coincidence with similar runs of the LIGO [1] detectors. The use of three detectors at the same time allows a reduction of background events by selecting only those events with triple coincidence. Furthermore it allows a (non-optimal) reconstruction of the sky location of the source. Between VSR2 and VSR3 the Virgo detector has been upgraded by replacing the last stage of each suspension chain (the payload). The mirrors were previously suspended using steel wires. The new suspensions system is made with fused silica fibers monolithically bonded to the mirror itself. Such monolithic suspensions were installed with the goal of reducing the thermal noise contribution to the detector sensitivity and to test this new technology in view of the Advanced Virgo upgrade [2]. The fourth science run ended on September 2011. Recently the interferometer has been shutdown to start the construction of Advanced Virgo. The goal is to improve the design sensitivity of the detector of a factor 10 with respect to the first generations.

During the last run, Virgo was near the design curve of sensitivity, in this condition the interferometer, besides the isolation from the fundamental noises, must work in conditions of extreme precision, especially in terms of alignments. For example, one

important technical noise source is the fluctuation in position and direction of laser beam (beam jitter): the angular jitter of the Virgo input laser, even if cleaned by an input mode-cleaner at the level of $10^{-11} rad/\sqrt{Hz}$, imposes that the mirrors of the cavities must be aligned with an accuracy of the order of $3 \times 10^{-9} rad$.
The first part of the PhD work has been addressed to model analytically the w2hole chain of beam jitter noise propagation from the laser to the set requirements for various sub systems and propose/test new improvements in the design according to the better overall understanding of this issue. Starting from the Virgo optical layout, a preliminary step has been to evaluate, how the seismic vibrations of the optical injection system are coupled to the TEM00 input beam. A second step has been to evaluate how these effects propagate in the main interferometer (ITF) and affect the dark-fringe carrying the GW signal. The goal has been to propose suitable optimization for Virgo and to set some parameters and requirements in order to obtain a beam jitter noise low enough to be compliant with Adv-Virgo sensitivity.
The second part has been dedicated to the effects of thermal deformations of the Adv-Virgo optics. In fact, in second generation of GW ITF, the use of high power laser (200W for project Advanced VIRGO) and the non zero absorption coefficient of the optics causes a local heating and consequently a wavefront geometric deformation of the reflected and transmitted beams.
A possible solution is represented by an active system that controls and corrects the wavefront distortions.
In particular, in the thesis, it has been studied and tested a suitably deformable mirror, actuated by an heather array, as a compensator for the beam deformations. The system has shown performances in terms of efficiency, checking the system stability, linearity and measurements repeatability.

The outline of this thesis is the following:

- The first two chapters are of an introductory nature. Chapter one is dedicated to the basic theory of gravitational waves and the possible astrophysical sources. Chapter two describes the principles behind the gravitational waves interferometric detection, in detail the Virgo detector and the Advanced Virgo project.

- The chapter three reports the beam jitter noise contribution in Virgo and Ad-Virgo, how it is limiting the dark fringe sensitivity, the principles of the techniques used to evaluate this technical noise to set some requirements to Adv-Virgo sensitivity.

- The following chapters describe the effect on Virgo optics using an high power laser and report the study and development of the active optics system for the correction of the thermally induced slow beam wavefront distortions.
  Theses distortions can be compensated using deformable mirrors driven by thermal actuators. In this thesis a prototype of a thermally deformable mirror (TDM) is described, and first results are presented.

Several appendices describes some ancillary topics that are relevant for all of the work of this thesis.

Chapter 1

Gravitational Waves

In the Einstein's theory of the General Relativity it is presented the concept of Gravitational Waves (GWs), small perturbations of Minkowski metric[4][5][6][7][8] . By the experimental results of R.A. Hulse and J. H. Taylor [9][10][11][12] it has been indirectly proven their existence but there is still no direct observation. The goal of this chapter is to briefly introduce the theory of gravitational radiation describing the Einstein field equations and their linearized form within the weak field approximation. Finally it is reported an outline of the generation mechanism and the possible astrophysical sources.

1.1 Einstein's Equations within Weak Field Approximation

The gravitational waves existence was predicted by Albert Einstein in a note entitled Näherungsweise-Feld der Integration der Gravitation gleichungen [13] (approximate integration of the gravitational field equations) presented to Königlich Preussichen Academy of Sciences, at the meeting physical and mathematical in its class, held in

Berlin on June 22, 1916.

We recall the equations of the gravitational field proposed by Einstein, which describe the evolution of the geometry of space-time:

$$R_{\mu\nu} - \frac{1}{2} g_{\mu\nu} R = \frac{8\pi G}{c^4} T_{\mu\nu} \tag{1.1}$$

where $g_{\mu\nu}$ represents the metric tensor which describes the geometry of space-time, the stress-energy tensor $T_{\mu\nu}$ describes the matter energy-momentum densities and fluxes and R is the scalar curvature and it is obtained by the contraction of the Ricci tensor $R_{\mu\nu}$ that is defined as the contraction of Riemann tensor $R_{\mu\nu\rho\sigma}$.

In the note referred to above, Einstein shows that these equations, in the "weak-field" approximation, take a simplified form. Indeed, under this assumption, we can write the metric tensor as the sum of flat space tensor $\eta_{\mu\nu}$ plus a perturbative term $h_{\mu\nu}$ much less than 1:

$$g_{\mu\nu} = \eta_{\mu\nu} + h_{\mu\nu} \qquad\qquad |h_{\mu\nu}| \ll 1 \tag{1.2}$$

$$\eta_{\mu\nu} = \begin{pmatrix} -1 & 0 & 0 & 0 \\ 0 & 1 & 0 & 0 \\ 0 & 0 & 1 & 0 \\ 0 & 0 & 0 & 1 \end{pmatrix}$$

In this way the equations 1.1 can be linearized by expanding the tensor $R_{\mu\nu}$ to the first order in $h_{\mu\nu}$.

In particular, it can be shown (see [14][15] for a detailed discussion) that there exists a particular choice of coordinates, corresponding to the Lorentz gauge for the metric, where the Einstein's equations in vacuum ($T = 0$) reduce to

$$\begin{aligned} &\Box h_{\mu\nu} = \left[\nabla^2 - (1/c^2) d^2/dt^2\right] h_{\mu\nu} = 0 \\ &\text{with the additional constraint: } \partial_\mu h^\mu_\nu = \frac{1}{2} \partial_\nu h^\mu_\mu \end{aligned} \tag{1.3}$$

These two equations are very similar to the ones that describe the propagation of electro-magnetic radiation, and therefore they can be solved by a packed of plane waves with wave-vector k_λ:

$$h_{\mu\nu} = \varepsilon_{\mu\nu} \exp(ik_\lambda x^\lambda) + \varepsilon^*_{\mu\nu} \exp(-ik_\lambda x^\lambda) \tag{1.4}$$

with

$$k_\lambda k^\lambda = 0 \qquad\qquad k_\mu \varepsilon^\mu_\nu = \frac{1}{2} k_\nu \varepsilon^\mu_\mu \tag{1.5}$$

The tensor $\varepsilon_{\mu\nu}$ describes the wave polarization and thanks to gauge invariance $\varepsilon_{\mu\nu}$ has six independent degree of freedom.
The choice of the gauge doesn't fix uniquely the solution, in particular it is always possible to reduce $\varepsilon_{\mu\nu}$ to a traceless tensor and transverse to the direction of wave propagation (TT gauge).
In the case of a wave that propagates in the z direction, i.e. with $k^\mu = (k, 0, 0, k)$, we have:

$$\varepsilon_{\mu\nu} = h_+ \varepsilon^+_{\mu\nu} + h_\times \varepsilon^\times_{\mu\nu} \tag{1.6}$$

with $\varepsilon^+ = \begin{pmatrix} 0 & 0 & 0 & 0 \\ 0 & 1 & 0 & 0 \\ 0 & 0 & -1 & 0 \\ 0 & 0 & 0 & 0 \end{pmatrix}$ $\qquad$ $\varepsilon^\times = \begin{pmatrix} 0 & 0 & 0 & 0 \\ 0 & 0 & 1 & 0 \\ 0 & 1 & 0 & 0 \\ 0 & 0 & 0 & 0 \end{pmatrix}$

The requirements 1.5 show that the gravitational waves are perturbations of the gravitational field spreading out in space at the speed of light. From the expressions of ε^+ and $\varepsilon^\times$ one can show that the two polarizations are rotated by $\pi/4$.
Therefore, the gravitational field, under the weak field hypotheses, is described by a massless particle of spin 2: the graviton.

1.2 Effects on free-falling particles

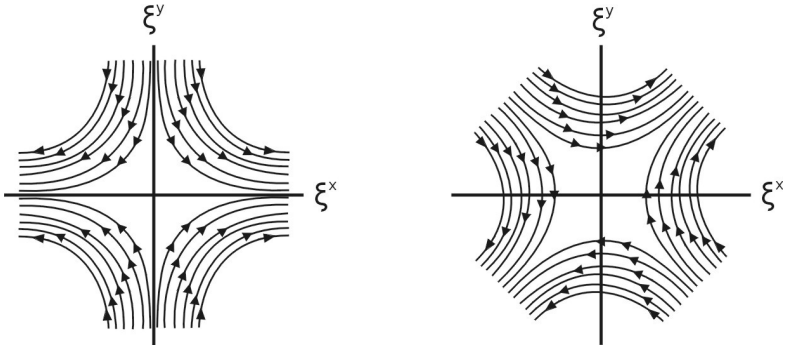

Figure 1.1: *The lines of forces of a gravitational wave for the two polarization states: (+) (left panel) and (x) (right panel). The orientation of the field lines changes every half period producing the deformations as in Figure 1.2.*

To understand the effect of a gravitational wave over a set of particles in free-fall, we need to recall the geodesic deviation equation. If $\xi^\alpha = x_2^\alpha - x_1^\alpha$ is the quadrivector distance between two masses in free-fall, we can write the following equation:

$$\frac{d^2\xi^i}{d\tau^2} + R^i_{0j0}\xi^j = 0 \tag{1.7}$$

which is the classical tidal force equation. It is possible to demonstrate that in TT gauge the relation $R_{i0j0} = 1/2\, h_{ij,00}$ is true, by this the Eq. 1.7 becomes:

$$\frac{d^2\xi^i}{d\tau^2} = 1/2\, h_{ij,00}\xi_j \tag{1.8}$$

where $\xi^i = x_1^i - x_2^i$. The solution of the 1.8 is:

$$\delta\xi_i = \frac{1}{2} h_{ij}\xi_j \tag{1.9}$$

Therefore, by the Eq. 1.9 the effect of a gravitational wave over two masses in free-fall is to change the relative distance along the directions perpendiculars to the

wave propagation direction (see Fig. 1.1 and Fig. 1.2).

Any point accelerates in the directions of the arrows, and the denser are the lines, the strongest is the acceleration. Since the acceleration is proportional to the distance from the center of mass, the force lines get denser as one moves away from the origin. For the polarization (x) the force lines undergo a 45° rotation.

For example, assuming a plus-polarized gravitational wave traveling along the z direction, the effect on the metric is given by:

$$ds^2 = c^2 dt^2 + (1 + h_+)\, dx^2 + (1 - h_+)\, dy^2 \tag{1.10}$$

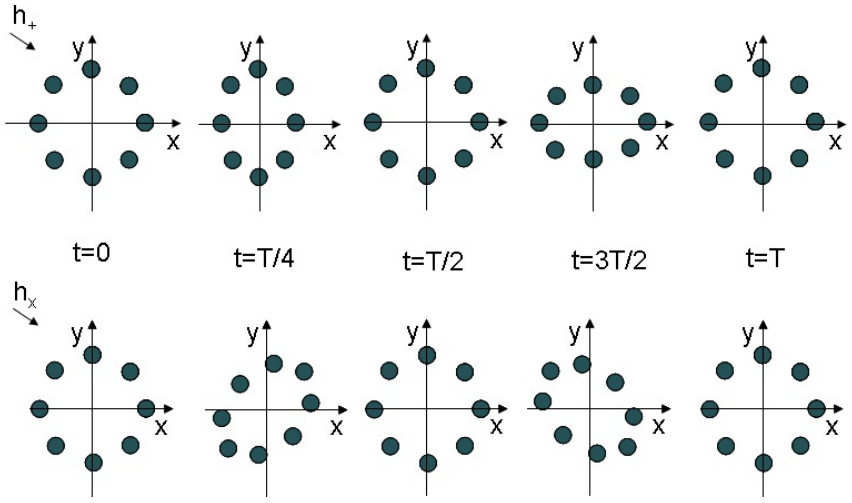

Figure 1.2: *The effect of a gravitational wave over a circular set of masses varying on time.*

1.3 Gravitational waves generation

In this paragraph we describe the possible sources of gravitational waves in the frequency band (from few Hz to few kHz) of interest for ground based interferometers.

To obtain the equations that govern the emission of gravitational waves we consider the linearization of equation 1.1 with $T_{\mu\nu} \neq 0$ and we obtain:

$$\Box h_{\mu\nu} = -\frac{16\pi G}{c^4}[T_{\mu\nu} - \frac{1}{2}\eta_{\mu\nu}T^{\lambda}_{\lambda}] \tag{1.11}$$

The solution will be:

$$h_{\mu\nu} = \frac{4G}{c^4}\int d^3\overrightarrow{x}\frac{[T_{\mu\nu} - 1/2\eta_{\mu\nu}T^{\lambda}_{\lambda}]_{t-r/c}}{|\overrightarrow{x} - \overrightarrow{x'}|} \tag{1.12}$$

From this equation we see that the stress-energy tensor causes a perturbation of the metric of space-time that is the action of gravitational waves generated.

Under the hypothesis that the source dimension R are much smaller than the distance from the observation point, it is possible to perform a multi-pole expansion of the Eq. 1.12 like for electromagnetic waves. From the conservation of momentum and angular momentum laws, we obtain that the first non-null term is the quadrupole momentum:

$$h^{TT}_{jk} = \frac{2G}{rc^4}\left(\frac{d^2I^{TT}_{jk}}{dt^2}\right)_{t-r/c} \tag{1.13}$$

where

$$I_{jk} = \int d^3\overrightarrow{x}\rho\left(x_jx_k - \frac{1}{3}|\overrightarrow{x}|^2\right) \tag{1.14}$$

The power emitted is:

$$\frac{dE}{dt} = \frac{1}{5}\frac{G}{c^5}\sum_{jk}\left|\frac{d^3I_{jk}}{dt^3}\right|^2 \tag{1.15}$$

As the power emitted of the gravitational waves is inversely-proportional to c^5, its effect is very weak. In addition, the lowest order of the radiation is caused by the change of the quadrupole moment, a spherically or axially moving system does not emit gravitational waves.

Using the Eq. 1.15 we can estimate the order of magnitude of the intensity of such radiation given the quadrupole momentum of a body of mass M and size R. It is

clear that in laboratory one can not generate strong enough gravitational radiation to be detectable on earth, as it can be seen considering the classic example of a bar in rotation. Consider a steel bar of 1 m radius and 20 m long rotating with angular velocity $\varpi = 4.4 cycles/s$ without breaking around an axis perpendicular to its length, one obtain:

$$\frac{dE}{dt} = -\frac{32}{5}\frac{G}{c^5} I^2 \varpi^6 = -2.2 \cdot 10^{-22} \text{erg } s^{-1} \tag{1.16}$$

where I is the moment of inertia with respect to the rotation axis, G is the gravitational constant and c is the speed of light. The value obtained is extremely low and very far from any possibility of detection. So gravitational waves can not be issued in the laboratory but by compact and massive cosmic objects (blacks holes, pulsars ...).

Indeed, consider a body of mass M and dimension R, and suppose that the quadrupole momentum vary on a time scale T. We have:

$$\frac{dE}{dt} \sim \frac{1}{5}\frac{G}{c^5}\left(\frac{MR^2}{T^6}\right)^2 \sim L_0 \left(\frac{v}{c}\right)^6 \left(\frac{r_{Sch}}{R}\right)^2 \tag{1.17}$$

where $L_0 = 3.6 \cdot 10^{59} \, erg \, s^{-1}$ e r_{Shc} is the Schwarzschild radius of the body ($r_{Shc} = GM/c^2$).

1.4 Sources of gravitational waves

Our efforts will be now concentrated on the detection of gravitational waves generated by astrophysics sources. The universe becomes our laboratory.

GWs are classified into three types according to the wave form:

1. Periodic GW sources: spinning neutron stars (pulsars).

The temporal behavior of these sources is sinusoidal with frequency f constant over time of the order of observation time.

2. Burst GW sources: supernova explosion, final coalescence of compact binary systems.
   The duration of these events is smaller than observation time.

3. Stochastic GW sources: cosmological sources related to the Big-Bang
   Their amplitude vary casually.

So the gravitational wave sources are classified through the lasting of the signal. The temporal behavior of a gravitational wave is important because it allows us to compare its amplitude with the level of noise of the antenna with which ones tries to detect it. This noise level is expressed as a density Spectral linear equivalent $\widetilde{h}_n(f)$ frequency-dependent. The amplitude of a gravitational wave can be compared with the noise once you know the bandwidth Δf.
In the case of wave pulses of duration τ, if we assume that the wave is spread over a bandwidth $\Delta f \sim 1/\tau$, the signal to noise ratio (which defines the sensitivity of the detector) is given by:

$$\frac{S}{N} = \frac{h}{\widetilde{h}_n(\Delta f)}\sqrt{\tau} \tag{1.18}$$

In contrast, in the case of periodic waves of frequency f_0, if the bandwidth of the wave is very small so the limit is represented by the observation time T of the signal, ie $\Delta f = 1/T$:

$$\frac{S}{N} = \frac{h}{\widetilde{h}_n(f_0)}\sqrt{T} \tag{1.19}$$

1.4.1 *Periodic sources*

Pulsars

Pulsars with an asymmetric mass distribution with respect the rotation axis emit GWs at frequency twice of the rotating frequency. The amplitude of the wave depends on the momentum of inertia of the star I_{zz}, on the distance from the Earth r, on the ellipticity ϵ in the equatorial plane and on the frequency emission f. We can estimate that:

$$h \sim 8 \cdot 10^{-19} \epsilon \left(\frac{I_{zz}}{10^{38} Kgm^2}\right) \left(\frac{f}{1KHz}\right)^2 \left(\frac{10Kpc}{r}\right) \tag{1.20}$$

Generally, since the ellipticity is small (about $\epsilon = 10^{-5}$), the amplitude is very small, but the periodicity allows to integrate over a sufficiently long time to improve the sinal-to-noise ratio. An example interesting in our galaxy is the Crab pulsar. The emission frequency is 60 Hz, the estimated amplitude is of the order of 10^{-24}.

Binary stars

Ordinary binary stars are one of the most reliably understood sources for periodic gravitational waves. Binary system composed by two coalescent strongly compact, as two neutron stars (NS), two black holes (BH) or a neutron star and a black hole lose considerable energy by means of gravitational radiation.

Binary stars typically have orbital periods larger than an hour and, correspondingly, gravitational wave frequencies $\leq 10^{-3} Hz$. This means that only space-based detectors will be able to detect them by integrating over long time periods.

These systems are very important for the physics community, because in 1993 J.H.Taylor and R.A. Hulse [9][10][11][12] gained the nobel price, obtaining an indirect evidence of the existence of gravitational waves by observation of a pulsar. They observed that the orbital period decay of the binary system PSR 1913+16 was

perfectly in agreement with the results predicted by gravitational wave emission. The frequency of the emitted wave is a double of the orbital one, and it increases the closer the two bodies become, until they merge together. The lifetime of these objects can be of millions of years (for the PSR 1913+16 is 10^8 years), but the gravitational radiation can be detected directly only in the last minutes of their life, when the orbital frequency is above several hertz and amplitude large enough to be detected.

1.4.2 *Burst sources*

Supernovae explosion

The supernovae explosions are the result of the gravitational collapse of nuclei of stars enough massive. They have all the attributes associated with a good gravitational wave source: they weigh several solar masses, they are compact and they experience large accelerations. However gravitational radiation only couples to a changing quadrupole moment and, hence, if a supernova collapse and the subsequent explosion have an axial symmetry, no gravitational waves are emitted.

If the explosion have a no-axial symmetry, f is the inverse of the time of collapse (of the order of 1 kHz) and ΔE_{gw}'s the energy emitted as gravitational radiation, we have:

$$h \sim 2.7 \cdot 10^{-20} \left(\frac{\Delta E_{gw}}{M_\odot c^2}\right)^{1/2} \left(\frac{1kHz}{f}\right)^{1/2} \left(\frac{10Mpc}{r}\right) \tag{1.21}$$

where r is the distance between Earth and source and M_0 is the solar mass. Some models give values for axial symmetry $\Delta E_{gw}/M_\odot c^2$ in the range from $5 \cdot 10^{-3}$ to 10^{-5}. If this event happens in our galaxy, $r = 10Kpc$, the expected signal $h \approx 10^{-17}$, would surely be detectable by current interferometers. Unfortunately, the estimated rate is about one event every thirty years, so it is interesting to estimate the possibility

of detection of gravitational waves emitted by supernovae of nearby galaxies: the Virgo cluster consists of hundreds of galaxies like ours, so in total it is expected some event for year. Given that, their distance from the Earth $10Mpc$ this should be the rate of detection.

Coalescing compact binaries

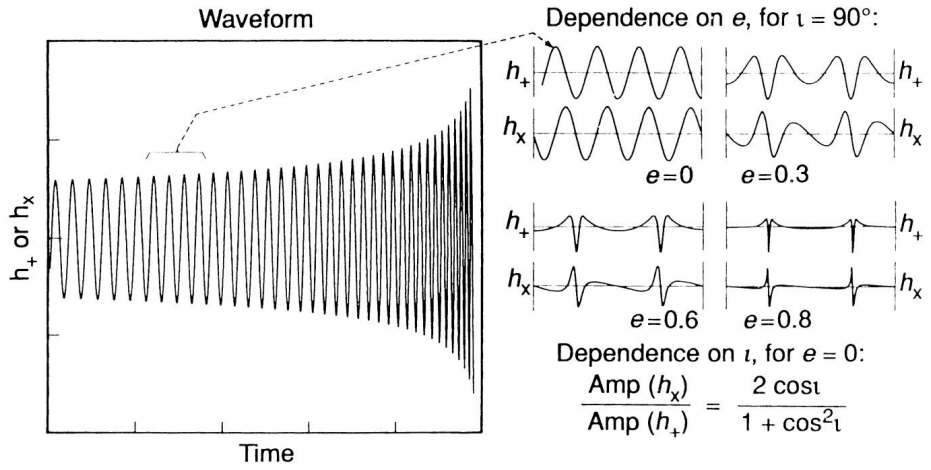

Figure 1.3: *Chirp waveform from an inspiral event of a compact binary system. On the right hand side the dependency of the waveform on the orbital eccentricity e and the orbital inclination i is demonstrated. The plot is taken from Ref.[17].*

Compact binaries are among the best candidates to be first seen by an earth based gravitational-wave antenna. Compact binaries can consist of either two neutron stars, two black holes or one of each. Due to their small size ($\leq$ 20 km in case of a neutron star), they can orbit each other at close range and a high orbital frequency (up to $\approx$ 500 Hz). Being very close and rotating fast means that the second time derivative of the mass quadrupole moment is large and, hence, gravitational waves are emitted with a high efficiency.

Indeed, the radiated energy is so large, that a double neutron star system which is 500 km or 100 km apart will loose all its potential energy within a couple of minutes or seconds, respectively. Since the emission of gravitational wave becomes more efficient at closer range, the waveform is a chirp signal (see Fig. 1.3 and Ref. [16]): increasing both in amplitude and frequency with time, until the two object are close enough to merge. To first order the chirp signal can be described by the change of its frequency over time $\dot{f}$ and by its amplitude A:

$$\dot{f} \propto M_c^{5/3} + f^{11/3} + \begin{pmatrix} \text{relativistic corrections} \\ M_1, M_2, S_1, S_2 \end{pmatrix} \tag{1.22}$$

$$A \propto k_{orbit} M_c^{5/3} + \frac{f^{2/3}}{r} \tag{1.23}$$

with M_c the chirp mass

$$M_c = \frac{(M_1 M_2)^{3/5}}{(M_1 + M_2)^{1/5}} \tag{1.24}$$

f the orbital frequency, M_1, M_2, S_1 and S_2 the mass and spin of the two compact objects, respectively, k_{orbit} a constant accounting for the inclination of the source orbital plane and r the distance to the source. If enough binary systems are detected, one can average over orbital parameters and can use them as standard candles. (One can determine the distance from the second equation using the chirp mass from the first equation.)

Calculating waveforms for coalescing compact binaries is straight forward, if the distance between the two objects is large, but for black hole mergers it is a formidable challenge. The coalescence of two black holes can be roughly divided into three phases:

- inspiral: The two black holes are well separated and the waveform of the emitted gravitational waveform is known,

- merger: The horizons of the two black holes merge together and the calculation of the exact waveform requires extensive simulations on a super computer, and
- ringdown: The two black holes have merged into a single black hole in an excited state which decays by emitting gravitational waves.

1.4.3 *Stochastic background (SGWB)*

The incoherent sum of random gravitational wave signals coming from astrophysical sources generate a stochastic background. But the SGWB have also a cosmological origin that make it very interesting. According to the Big-Bang model and standard inflationary model GWs can be produced by the mechanism of amplification of vacuum fluctuations. Once produced, GWs travel through space-time at the speed of light as we know, and are essentially unaffected by the matter they encounter. As a result, GWs emitted shortly after the Big Bang (and observed today in SGWB) would carry unaltered information about the physical processes that generated them. Therefore the SGWB should carry also a unique signatures from the earliest epochs in the evolution of the Universe, inaccessible to standard astrophysical observations. The SGWB is usually described in terms of the gravitational-wave spectrum:

$$\Omega(f) = \frac{1}{\rho_c}\frac{d\rho_{gw}}{d\log f} \tag{1.25}$$

where ρ_{gw} is the energy density of gravitational radiation contained in the frequency range f to $f + df$ and ρ_c is the critical energy density of the Universe.

Chapter 2

Gravitational Waves interferometric detection: Virgo+ Experiment

In this chapter we describe the GW interferometric detection principle with particular care to the Virgo+ detector [18][19][20][21].
In the previous chapter we have observed that the gravitational waves distort space-time and produce forces in such a way that the distance between free masses will alternately decrease and increase during the passage of a wave (Eq. 1.9 e Fig. 1.2).

The amplitude of gravitational waves, the dimensionless parameter "h", is measured by the relative variation of distance between two free masses. The absolute variation is therefore proportional to the distance between the two masses. It would typically be "as large" as the size of an atom if one could monitor the distance from the earth to the sun, and it would be about one hundred millions times smaller for two points separated by a distance of a few kilometers.
Such a small variation of distance can however be detected through the phenomenon of interference. A laser Michelson interferometer is very sensitive to differential

length variations between its two arms and is ideally suited to the detection of gravitational waves.

In particular, Virgo is very sophisticated Michelson interferometer (see Fig. 2.1) borne by a collaboration between INFN Italian and CNRS French and it is located in Cascina near Pisa (Italy).

The commissioning of the Virgo interferometer begun in 2003. These efforts led,

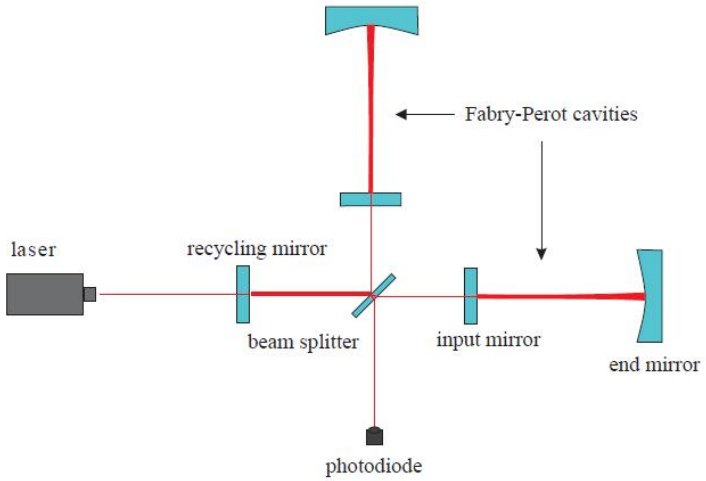

Figure 2.1: *Optical scheme of a Fabry-Perot interferometer with power recycling. The recycling mirror between the laser and the beam splitter reflects the light back to the interferometer which is locked on the dark fringe.*

in 2007, to the first scientific run VSR1 in coincidence with LIGO (Laser Interferometer Gravitational-wave Observatory). After VSR1, during 2008 and half of 2009, the commissioning activity restarted and the interferometer underwent several upgrades to further improve its sensitivity. In July 2009, Virgo started its second science run (VSR2) in coincidence with the sixth science run (S6) of the two 4 km long LIGO interferometers L1 and H1 (located in Livingston Parish -Louisiana- and

Hanford -Washington State- respectively). At the beginning of 2010, the steel wire used for the suspension is replaced with fused silica fibers monolithically bonded to the mirror body [23]. In this way dissipative processes are expected to be largely reduced resulting in lower thermal noise and better sensitivity at low frequency .
At August 2010 there was the VSR3 and in June 2011 Virgo started its fourth science run (VSR4), just completed (September).
In parallel a Advanced Virgo detector is been designed, aiming at a sensitivity 10 times better than Virgo.

2.1 Michelson Interferometer detector

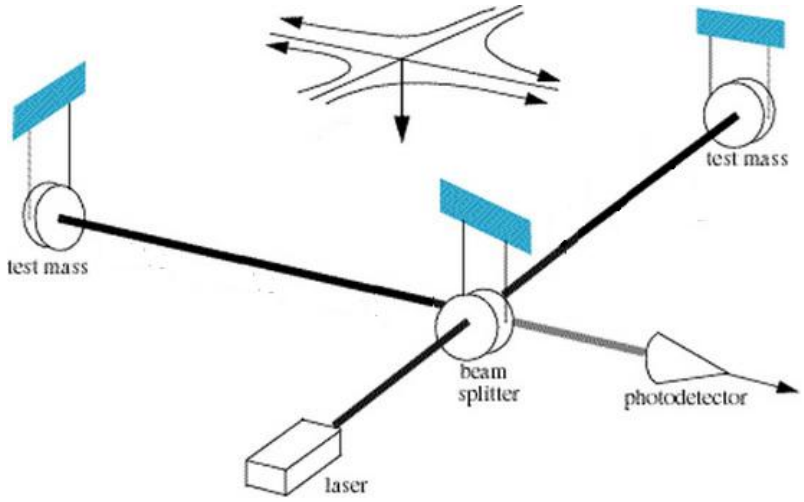

Figure 2.2: *A diagram of a interferometer detector, where the time it takes light to travel between suspended mirrors is measured with high precision using controlled laser light.*

A ground based Michelson interferometer detector may be considered free falling (with respect to the horizontal plane) in a proper range of frequencies, if the mirror

are **"suspended"**(Fig. 2.2).

The method to isolate a test mass m is to connect it to the noisy ground through a spring. The best way to do this is to suspend the test mass as a pendulum. In this case the restoring force is mostly gravitational and the dissipation is minimized. Neglecting the dissipative term, the well known equation of motion of the mass m is:

$$m\ddot{x} + k\,(x - x_0) = F_{ext} \tag{2.1}$$

where k is the spring stiffness ($k = \frac{mg}{l}$), x the suspension position and F_{ext} is an external force applied to the the mass.

In the frequency domain the solution is given by:

$$x(\omega) = \frac{\omega_0^2 x_0(\omega) + F_{ext}(\omega)/m}{\omega_0^2 - \omega^2} \tag{2.2}$$

with $\omega_0 = 2\pi f_0$ and $f_0 = \sqrt{k/m}$ is the oscillator resonant frequency.

For frequencies $\omega >> \omega_0$ this equation becomes:

$$m\omega^2 x(\omega) + F_{ext}(\omega) \approx 0 \tag{2.3}$$

and, getting back to the time domain, we find:

$$m\ddot{x} \approx F_{ext}(t) \tag{2.4}$$

that is, the mass responds to the external force as it was free (see Eq.1.8).

In section 1.2 we calculated the effect of a gravitational wave on free-falling particles. Equation 2.4 shows that a optical components suspended to form pendulums behaves like a freely falling one for frequencies of the impinging gravitational wave above the pendulum resonant frequency. So, above a certain frequency, if a gravitational wave impinges on Michaelson interferometer with suspended mirror, the mirror position will change according to Eq. 1.9

$$\Delta x = \frac{1}{2} hL \tag{2.5}$$

with L the arm length.

For a periodic gravitational waves propagating in the vertical (z) direction and with polarization axes parallel to the arms of the interferometer $\left(h = h_0 e^{-i\Omega t}\right)$, the length variations of the x and y axis will be:

$$\Delta x = \frac{1}{2} h_0 e^{-i\Omega t} \tag{2.6}$$

$$\Delta y = -\frac{1}{2} h_0 e^{-i\Omega t} \tag{2.7}$$

An analogous equation is worth for the optical paths phase difference $\Delta\phi = 4\pi/\lambda\,(\Delta x - \Delta y)$:

$$\Delta\phi = \frac{4\pi L}{\lambda} h_0 e^{-i\Omega t} \tag{2.8}$$

By measuring $\Delta\phi$ it is possible to detect the gravitational wave. From Eq. 2.8 we observe that the phase-difference $\Delta\phi$ is proportional to the arm length of the interferometer. This is the reason for which, compatible with costs, long-arm gravitational wave interferometers (a few Km) have been designed. Consider an interferometer with arm-length of about 3 Km (like Virgo), if it is crossed by a gravitational wave of amplitude 10^{-21} (typical value at 10 Hz), the motion of the mirror is of the order of 10^{-18} m. The weakness of this signals impose the construction of apparatus extremely sensitive and complex.

2.2 Fundamental noises

As previously mentioned, an interferometric detector like VIRGO aims to measure length variations below 10^{-18} m, that is about 1/1000 of a proton diameter. We need a interferometer very sensitive on the frequencies band of the measure. Therefore is very important the analysis and the reductions of the all noise that arise during the detection. The noise sources that limits a detector sensitivity or in general one

interesting signal are really numerous and they can be classified with respect their origin:

- Fundamental noise. Connected with intrinsic limit of the detector. Examples can be seismic noise not completely filtered by the super-attenuators shot-noise that limits the photo-diodes output depending on the level of power hitting them or suspension and mirror thermal noise.

- Control noises. These are those noises reintroduced in the system or amplified by the control loops used to maintain the correct operating point.

- Technical noise. More in general these are those noises coming not from fundamental limits but rather from the actual implementation of the detector. An example is the beam jitter noise, namely how fluctuations of the beam pointing at the interferometer input results in phase noise.

- Environmental noises, like electro-magnetic fields coupling to the detector output or to the coils used for the actuation, or acoustic and seismic vibration outside the vacuum system that can re-enter the interferometer by means of diffused and scattered light.

In particular in next sections we treat the fundamental noise sources and in the next chapter we offer a detailed study of the noise generated by the coupling between the interferometer asymmetries and the input laser beam geometrical fluctuations, or beam jitters.

2.2.1 *Shot-noise and quantum limit*

How predicted by the Heisemberg uncertainty relation, a quantum limit to the precision of position measurements exists.

Actually, the ultimate noise which affects the phase shift at the output of the detector is the photon counting noise $\Delta\phi_{pc}$ due to the anticorrelated fluctuations of the number of photons n in the interferometer arms, according to the uncertainty relation $< \Delta\phi^2 > \cdot < \Delta n^2 > \geq 1$. For a photon coherent state $\Delta n = \sqrt{n}$ and we can write the phase fluctuations due to photons counting error as:

$$< \Delta\phi_{pc}^2 > \approx \frac{1}{n} = \frac{h\nu}{\eta P T} \tag{2.9}$$

where T is the measurement time, h is the Planck's constant, ν is the laser frequency, P is the power of the input laser, η the quantum efficiency of the photodiode so that ηP is the power of the beam entering the interferometer. The linear spectral density of this phase fluctuation is straightforward:

$$\tilde{\Delta\phi_{pc}} = \sqrt{\frac{2h\nu}{\eta P}} \tag{2.10}$$

If we confront this noise with the amplitude of gravitational wave signal given by the equation 2.8, we can find a limit for the minimum value of $\tilde{h}$ allowed:

$$\tilde{h} = \frac{\lambda}{4\pi L}\sqrt{\frac{2\hbar\omega}{\eta P}} \quad \left[\frac{1}{\sqrt{Hz}}\right] \tag{2.11}$$

According to this equation, the level of this noise, usually called shot noise, can be reduced by using longer arms and increasing the power of light circulating into the interferometer.

Virgo and other detectors adopt Fabry-Perot cavities to amplify the phase shift accumulated in the arms and the technique of power- recycling to increase the power inside the ITF. At the same time an increase of the power increases the noise induced by the fluctuations in the radiation pressure on the mirrors of the interferometer. In fact, the mirrors are subject to a force F due to the radiation pressure:

$$F = 2n\frac{\hbar\omega}{c} \tag{2.12}$$

where n is the number of photons which hit the mirror per unit time. Each fluctuation of the photon flux causes a variation of the force F and then a displacement of the mirror. The variation of phase-difference at the output of the interferometer as function of frequency Ω is:

$$\Delta\tilde{\phi} = \frac{4\pi}{\lambda}\frac{\sqrt{8P\hbar\omega}}{M\Omega^2 c} \tag{2.13}$$

where M is the mass of the mirror. In this calculation we supposed the frequency Ω is much greater than the resonance frequency of the pendulum which suspends the mirror. If we sum the two contributions, that is the photons shot-noise and the pressure fluctuations, we have:

$$\Delta\tilde{\phi} = \sqrt{\frac{2\hbar\omega}{\eta P} + \left(\frac{4\pi}{\lambda}\right)^2 \frac{8P\hbar\omega}{(M\Omega^2 c)^2}} \tag{2.14}$$

From this relation we see that it exists an optimal power P_{opt} for which $\Delta\tilde{\phi}$ has a minimum:

$$P_{opt} = \left(\frac{1}{2n}\right)^2 \frac{Mc^2}{\omega}\Omega \quad \Rightarrow \quad \Delta\tilde{\phi_{QL}} = \frac{4\pi}{\lambda}\frac{1}{\eta^{1/4}}\sqrt{\frac{4\hbar}{M\omega^2}} \tag{2.15}$$

The quantity $\Delta\tilde{\phi_{QL}}$ represents the quantum limit to determination of the phase.

2.2.2 *Fabry-Perot cavities and recycling of light*

The shot-noise limited sensitivity of a Michelson depends by the arms length L (Eq. 2.11). In order to amplify the optical path of the light inside the ITF, Fabry-Perot cavities are inserted in the arms (see Fig. 2.1). When the cavity is at resonance the phase shift induced by the gravitational wave's passage is increased, with respect to the single mirror configuration, proportionally to the Finesse $\mathcal{F}$ of the cavity.
The shot-noise limited sensitivity of a Michelson with Fabry-Perot cavities in the arms is:

$$\tilde{h}_{shot} = \frac{\lambda}{4\left(L_1 + L_2\right)\mathcal{F}}\sqrt{\frac{2\hbar\omega}{\eta P}}\sqrt{1 + \left(\frac{f}{f_{FP}}\right)^2} \quad \left[\frac{1}{\sqrt{Hz}}\right] \tag{2.16}$$

where L_1 and L_2 are the lengths of the two cavities and $f_{FP} = c/4L\mathcal{F}$ is the Fabry-Perot cut-off frequency. For Virgo, the Finesse of the Fabry-Perot cavities is $\mathcal{F} = 50$.

In order to increase the power impinging on the BS, the technique of light recycling is applied.
If the interferometer is locked on the dark fringe (required to optimize the interferometer response), most of the power reflected back to the laser can be recycled by inserting an additional mirror between the laser and the beam splitter which reflects back the light towards the interferometer (see Fig. 2.1). The interferometer can be described as a composite mirror which, together with the recycling mirror, forms a recycling cavity to be kept in resonance. With this power recycling technique the power stored into the arms can be increased by a large factor, thus reducing the shot noise level (Eq. 2.11).
With respect to the previous configuration, without PR, the shot-noise limit improves by a factor $1/\sqrt{G_{rec}}$:

$$\tilde{h}_{shot} = \frac{\lambda}{4\left(L_1 + L_2\right)\mathcal{F}}\sqrt{\frac{2\hbar\omega}{\eta G_{rec} P}}\sqrt{1 + \left(\frac{f}{f_{FP}}\right)^2} \quad \left[\tfrac{1}{\sqrt{Hz}}\right] \tag{2.17}$$

G_{rec} is the maximum recycling gain and for Virgo is ≈ 50.
The linear spectral density of the shot noise is of the order of $10^{-23}/\sqrt{Hz}$, two orders of magnitude less than would be obtained in simple Michelson configuration. The shot noise limits the Virgo sensitivity at high frequency, starting from $500 - 600Hz$. The other limiting fundamental noise sources in the low and mid frequency region for this kind of detector are *seismic noise* and *thermal noise*. These are described in the next paragraphs.

2.2.3 *Seismic noise*

A ground based interferometric antenna suffers of the permanent soil vibrations induced by seismic activity, wind, oceans activity and human activity. They are transmitted to the optical components throughout the suspension systems and the resulting noise is the main limitation to the sensitivity of the receiver in the low frequency range (0.1 Hz to 10 Hz) and falls off quickly at higher frequencies.
Typical seismic noise levels are:

$$x(f) \approx \frac{10^{-7}}{f^2} m/\sqrt{Hz} \qquad \textbf{for } 1Hz < f < 10Hz \tag{2.18}$$

If these vibrations propagate to the mirror, producing a displacement $x_{seismic}(f)$, it will be possible to detect a gravitational wave of amplitude $\tilde{h}$ only if $\tilde{h} > x_{seismic}(f)/L$L, independently by the use of techniques of optical amplification of the signal (delay-line or Fabry-Perot).
It follows that it is possible to reduce the effect of vibrations induced by seismic noise only by increasing the interferometer arm-length. But since it is not possible to build interferometer with arm-length greater than a few Km, it is necessary to implement very efficient seismic noise attenuation systems. The typically attenuation systems used consist of a chain of pendula in cascade.
Consider a mirror suspended to a pendulum with elastic constant k, mass m and under a viscous damping b; the mirror displacement $x_{seismic}(f)$, induced by seismic vibrations $x(f)$ of the suspension point, is:

$$x_{seismic}(f) = H(f)x(f) = \frac{f_0^2}{f_0 - f^2 + if\frac{b}{2\pi m}} x(f) \tag{2.19}$$

where $H(f)$ is the transfer function of the oscillator and $f_0 = \frac{1}{2\pi}\sqrt{\frac{k}{m}}$ the cut-frequency.

At frequency f greater than the resonance:

$$H(f) \approx \frac{f_0^2}{f^2} \qquad \textbf{for } f > f_0 \tag{2.20}$$

that is, the oscillator acts as a filter for frequencies over the resonance frequency f_0. Therefore, for a fixed frequency $f > f_0$, we can increase the attenuation by lowering the resonance frequency of the pendulum and by using several pendula in cascade. By the way, at the resonance an input signal is amplified of a factor $Q = 2\pi m f_0/b$. So it is important for the system to be highly dissipative, i.e. with a very low Q.

2.2.4 *Thermal noise*

Thermal noise constitutes the most important noise source in the band from some dozen Hz to many hundred Hz. It represents the fluctuation of a macroscopic observable of the system at the thermodynamic equilibrium with the ambient, due to the thermal agitation of the microscopic elements constituting it.
For this reason this noise comes out to be an unavoidable limit for the precision of many measurements. In the interferometers this noise enters the sensitivity in the following ways:

- **suspension thermal noise**, which is responsible for displacement of the mirrors center of mass. It has three different sources:

  I. pendulum mode thermal oscillation,

  II. vertical mode thermal oscillation,

  III. violin modes thermal oscillation;

  [I.]

- **mirror thermal noise (in the bulk and in the coating)**, which can be divided into:

1. Brownian thermal noise,
2. thermoelastic noise,
3. thermorefractive noise.

Thermal noise is associated with internal dissipation phenomena. According to the fluctuation-dissipation theorem [22], dissipation phenomena are connected to a stochastic motion of the system itself.

For a linear mechanical system, we can write its equation of motion in the frequency domain in terms of an external force $F_{ext}(\omega)$ necessary to cause the system to move with a sinusoidal velocity of amplitude $v(\omega)$:

$$F_{ext}(\omega) = Z(\omega)v(\omega) \tag{2.21}$$

where the function $Z(\omega)$ is called the impedance. The fluctuation-dissipation theorem states that, at thermodynamic equilibrium, the power spectrum $F^2_{therm}(\omega)$ of the minimal fluctuating force on a system is given by:

$$F^2_{therm}(\omega) = 4k_B T\mathcal{R}\left(Z(\omega)\right) \tag{2.22}$$

where $\mathcal{R}\left(Z\right)$ indicates the real (i.e. dissipative) part of the impedance, k_B is the Boltzmann's constant, and T is the absolute temperature.

This stochastic force produces a Brownian motion of the system with power spectral density given by:

$$x^2_t(\omega) = \frac{4k_B T\mathcal{R}\left(Z\right)}{\omega^2\left|Z(\omega)\right|^2} \tag{2.23}$$

In the typical case of an oscillator damped by dissipative force proportional to the velocity, $\mathcal{R}\left(Z(\omega)\right)$ becomes a constant ($\mathcal{R}\left(Z(\omega)\right) = m/\tau$) depending by the mass m and the time constant τ. If the oscillator resonance frequency is $\omega_0 = \sqrt{k/m}$, the power spectral density of the displacement due to the thermal noise is:

$$x^2_t(\omega) = \frac{4k_B Tm/\tau}{m^2\left[\left(\omega^2 - \omega_0^2\right)^2 + \left(\omega/\tau\right)^2\right]} \tag{2.24}$$

For the pendulum mode of the suspension, the resonance frequency ω_0 is below the bandwidth ($\omega_0 << \omega$) for the detection of gravitational waves, so the Eq. 2.24 becomes:

$$x_t(\omega) = \frac{\sqrt{4k_B T m/\tau}}{m\omega^2} = \frac{1}{\omega^2}\sqrt{\frac{4k_B T \omega_0}{mQ}} \tag{2.25}$$

where $Q = \omega_0$ is the suspension quality factor. Then thermal noise effect decreases with increasing the frequency ω. Moreover, by Eq. 2.25 we see that the effect of thermal noise can be reduced by increasing the suspension quality factor Q and by increasing the mass of the mirror.

The noise due to the resonance modes of the mirror can be described as a set of oscillators corresponding to its normal modes. In this case the frequencies are of the order of several kHz, then above the bandwidth of detection; so the Eq. 2.25 becomes:

$$x_t(\omega) = \sqrt{\sum_i \frac{4k_B T m_i/\tau_i}{m_i^2 \omega_i^4}} = \sqrt{\sum_i \frac{4k_B T}{m_i Q_i \omega_i^3}} \tag{2.26}$$

where m_i is the effective mass of the mirror corresponding to the normal mode i with resonance frequency ω_i. We can see that the thermal noise effect decreases with increasing of the mirror Q factor and with increasing of the resonance frequency ω_i. Finally, we can notice that, as for the seismic noise, also for the thermal noise there is a decreases (with L^{-1}) of the interferometer sensitivity independently by the use of techniques of optical amplification of the signal (delay-line or Fabry-Perot).

2.3 Virgo+ Experiment

Virgo+ is the new version technology upgraded of Virgo detector, designed to detect gravitational waves of both astrophysical and cosmological origin in the frequency range from a few Hz to a few kHz.

With sensitivity in spectral density h of about $10^{-23}\ \frac{1}{\sqrt{Hz}} \div 10^{-22}\ \frac{1}{\sqrt{Hz}}$ in a frequency

range near 100 Hz.

This corresponds, in terms of relative displacements of the test masses, to measure length variations of less than $10^{-19}\ \frac{m}{Hz}$.

Clearly a so strong requirement need the extremely sophisticated experimental technique to be satisfied.

Since 2007 Virgo completed three scientific data taking periods (Virgo Science

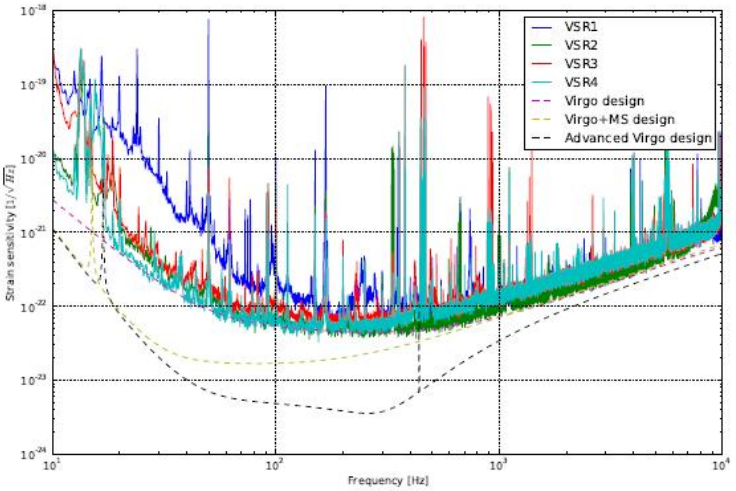

Figure 2.3: *Virgo detector measured sensitivities during the past and present science run. Design sensitivities are also included for Virgo with steel wire suspensions, with monolithic suspension and for Advanced Virgo.*

Run 1 to 3) and started recently (on June 3rd 2011) its fourth run. The first three periods were carried out in partial or complete coincidence with similar runs of the LIGO [1] detectors. The use of three detectors at the same time allows a reduction of background events by selecting only those events with triple coincidence. Between VSR2 and VSR3 the Virgo detector in a new version technology upgraded Virgo+ by replacing the lower part of each suspension chain (the payload); see the

Virgo+MS design curve in Fig. 2.3.

Such monolithic suspensions were installed with the goal of reducing the thermal noise contribution to the detector sensitivity and to test this new technology in view of the Advanced Virgo upgrade [2]. The fourth science run (VSR4) is planned to continue until 5 September 2011. After this date a long shutdown is planned to install all the upgrades needed to implement Advanced Virgo. The goal is to improve the design sensitivity of the detector of a factor 10 with respect to the first generations. Early runs are expected, in coincidence with Advanced LIGO [3], at the end of 2015.

2.3.1 *Virgo+ Overall Design*

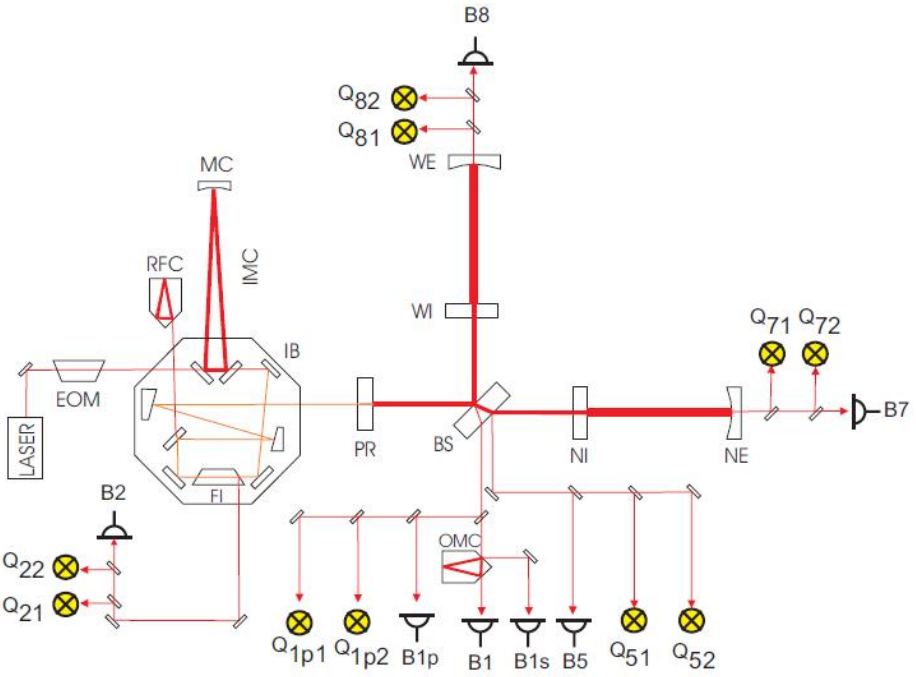

Figure 2.4: *Virgo optical layout. The main symbols are defined in the text.*

The optical design of Virgo+ is sketched in Fig. 2.4. A 20 W laser beam at

1064 nm is produced by a Nd:YVO4 high power laser, injection-locked to a solid state 1WNd:YAG master laser. The beam, after passing through the optical table for its alignment, enters the vacuum system, reaching the input optical bench (IB), suspended by a reduced-size seismic-isolation system (see below). The beam is then spatially filtered by a 144 m long triangular cavity (input mode cleaner - IMC) with the input and end mirrors assembled on the IB, and the intermediate mirror suspended at 144 m (Mode Cleaner - MC mirror). This additional cavity selects the optical fundamental mode (the Gaussian TEM_{00} mode), suppressing the high-order modes. The IMC is also used as a reference to pre-stabilize the laser beam frequency. The IMC length is stabilized in the low frequency range (below a few tens of Hz, where seismic noise and other spurious mechanisms induce fluctuations of the cavity length) by using as a reference a rigid 30 cm-long reference cavity (RFC), placed under the IB. After the IMC, the beam passes through the power recycling mirror (PR), is separated by the beam splitter (BS) and enters the two long Fabry-Perot cavities (North and West cavity). The nominal Finesse of the arm cavities is 50, with an input mirror power transmittance of 11.7% and the end mirror having almost full reflectivity (power transmittance around 3 x 10^{-4}). The Gaussian beam radius (i.e. the distance from the optical axis at which the field amplitude and intensity drops to $1/e$ and $1/e^2$) is 6 cm at the end curved mirror, while the minimum radius (beam waist) is on the flat input mirror (2 cm). The PR is a semi-transparent mirror located between the laser source and the beam splitter and has a reflectivity towards the interferometer around 95%. As discussed in section 2.2.2, this mirror forms an additional Fabry-Perot cavity between the whole interferometer and itself. In this way the power impinging onto the BS is amplified by a factor around 50.

The output interference signal is reconstructed by the photodiode B1, made by a set of high-quantum efficiency InGaAs photodiodes. This photodiode is assembled on

a bench, outside the vacuum system. The output beam, before reaching B1, passes through a monolithic 2.5 cm long cavity (output mode cleaner - OMC), located on a bench suspended in vacuum. The OMC is designed to filter high-order optical modes, originating from misalignments and optical defects. The other photo- diodes (labelled by "B" in Fig. 2.4) are used as feed-back error signals, to fix the longitudinal lengths of the interferometer (cavity resonance condition and destructive interference on B1) with a very high level of accuracy (around $10^{-12} \div 10^{-10}\ m$). The longitudinal control is done using the RF-modulation of the beam light by means of the Pound-Drever technique. In order to optimize the contrast in the interference pattern, the interferometer mirrors must be aligned with each another and with respect to the beam with a nanoradian accuracy. This is done using a feedback based on the error signals coming from the quadrant photodiodes (labeled by "Q" in Fig. 2.4).

All the six main Virgo mirrors (Power Recycling, Beam Splitter, North Input, North End, West Input, West End, with obvious notations in Fig. 2.4) are suspended from a Superattenuator (see Fig. 2.5). The other optical components, whose displacement does not induce an apparent arm variation (since they are located before the beam injection to the interferometer, or after the recombination of the beams) have less stringent isolation requirements. For this reason IB, MC and DB are suspended from shorter Superattenuators, having only two mechanical filters. The mirror and its Reference Mass are suspended in parallel from a Marionette, attached to the last filter of the chain by a steel wire. Longitudinal and angular forces for the interferometer locking and alignment can be applied both to the Marionette and to the mirror by coil-magnet actuators, with coils assembled on the last filter of the chain and on the Reference Mass.

In order to reduce the variations of the refraction index, due to the gas density fluctuations, the entire interferometer must be kept in vacuum (at a pressure less

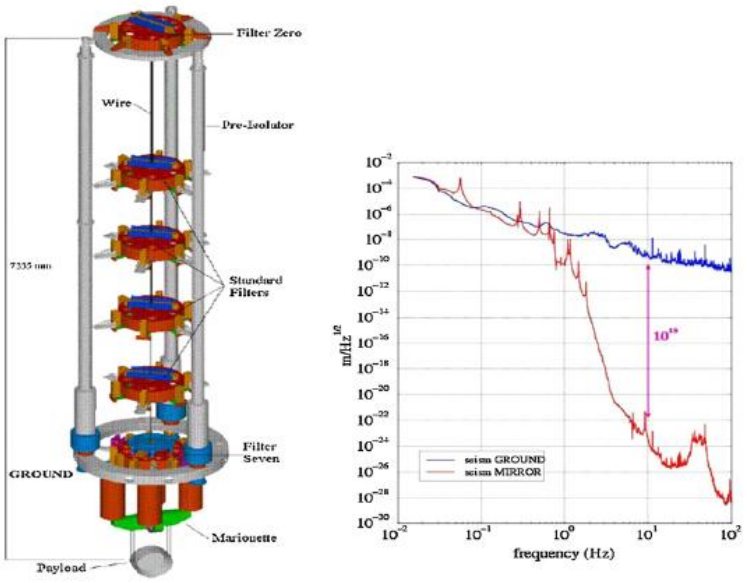

Figure 2.5: *The left panel is the image of the entire Virgo superattenuator. The right panel presents comparison of the spectral density of seismic noise at the ground and that at the mirror. The Virgo superattenuator provides suppression of the amplitude spectral density of noise by 15 orders of magnitude at 10 Hz frequency.*

than 10^{-8} mbar to meet Virgo and Virgo+ requirements, with a good safety margin). For this reason, each of the long Fabry-Perot cavities is contained in a 3 km-long vacuum pipe, with a diameter of 1.2 m.

2.3.2 *Injection System*

The laser system is accommodated in air, on an optical bench resting on the ground (Fig. 2.6). The master laser is a 1W Nd:YAG Non Planar Ring Oscillator (from Innolight Company). A 20 W-high power laser from Laser Zentrum Hannover (slave laser) is locked to the light coming from the master one. The feed-back allows transferring the large frequency stability performance of the master laser to the

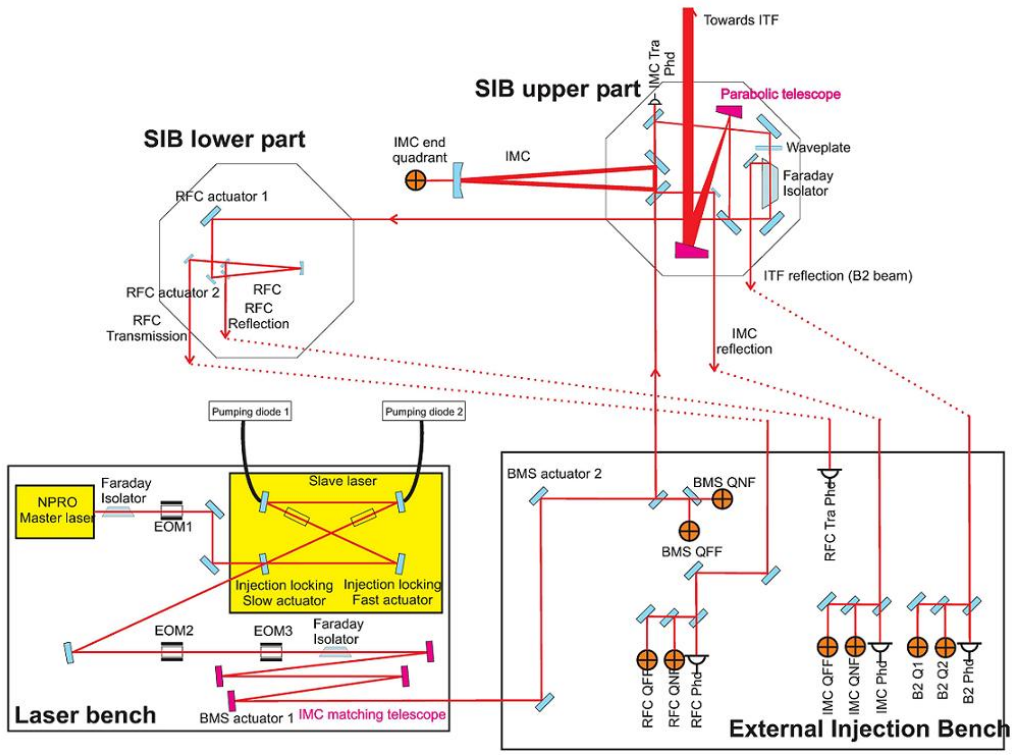

Figure 2.6: *The Virgo Injection System. The Master and Slave Laser bench is on the bottom left. The light goes to the External Injection Bench on the bottom right. The Suspended Injection Bench top and down views are shown on the top right and left respectively.*

high power slave laser. The optics located on the external injection bench (EIB), resting on the ground, and accommodated in an acoustically isolated environment, steers the beam to be injected to the IMC (Bondu et al., 2002). Thanks to its high Finesse (around 1000), the IMC cavity gives a strong suppression of the higher modes, different from the fundamental Gaussian one, strongly reducing the beam geometry fluctuations, in particular the beam pointing jitter (how we will discuss in the next chapter). The IMC filters also the laser frequency and the amplitude fluctuations, above its cut-off frequency at the cavity pole (around 500 Hz). In a

144 m-long cavity, the free-spectral range (that is the frequency-distance between two consecutive resonances in the transmission spectrum) is around 1 MHz. As a consequence, a so long cavity allows to transmit to the interferometer any multiple of 1 MHz, giving us a large flexibility in choosing the RF-modulation frequencies to be transmitted to the interferometer for the longitudinal and angular control.

The locking of the laser frequency on the IMC length is made by using the Pound-Drever technique and the piezoelectric actuators of the master laser. The 30 cm-long reference cavity, assembled on the IB, is made by an ultra-low thermal expansion coefficient ceramic, and supports three mirrors. As already mentioned, this high-Finesse cavity (1000) is used to stabilize the IMC length in the low frequency range. A pre-stabilization of the laser frequency, around $10^{-2}\frac{1}{Hz}$ in the Virgo detection band, is achieved in this way. This pre-stabilization is a mandatory step to achieve both the locking of the interferometer and the final frequency stabilization.

In Virgo only 50% of the available light of the laser (corresponding to about 8-9 W) in the IMC is transmitted to the interferometer. This is due to optical losses taking place on the various optical components.

A Faraday isolator, located on the IB, turned out to be necessary to prevent spurious light scattered off the interferometer to re-enter the IMC. At the output of the injection system, before entering the interferometer a small portion of the light is picked up. Its power fluctuations are monitored by a photodiode and a correction sent to the current of the slave laser. This feed-back allows one to have a beam at the input of the interferometer with the required power stability, i.e. a relative intensity noise ($\delta P/P$) about $10^{-8}\frac{1}{Hz}$. A local control system allows one to fix the position of the IB and of the MC with respect to the ground, with accuracy below 1 μm (or $1\mu rad$, in angle). This allows a good pre-alignment of the cavity necessary for the laser locking on the IMC. After the locking, the automatic alignment system,

based on quadrant photodiodes, allows low-noise angular control of the mirrors.

2.3.3 *Detection System*

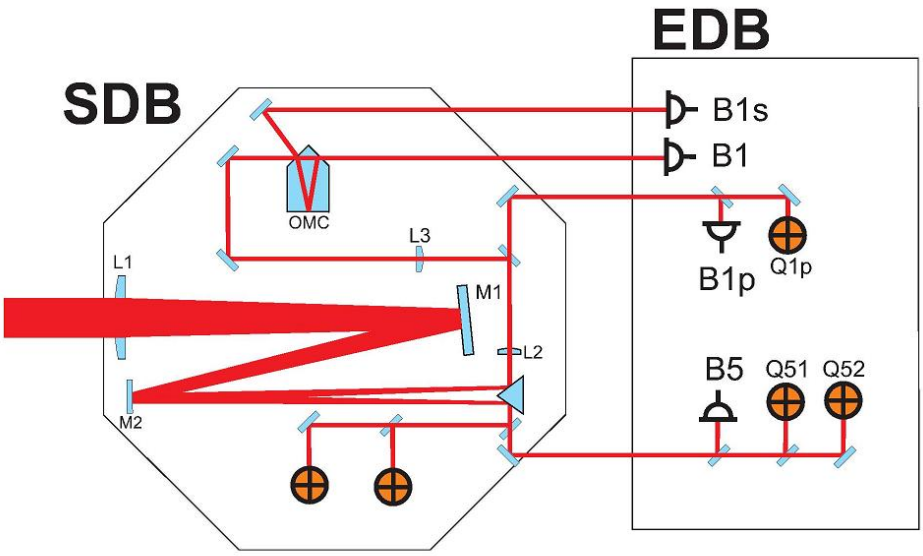

Figure 2.7: *Schematic view of the detection system. B1 is the dark fringe beam and B5 is the beam reflected by the second face of the Beam Splitter mirror. B1p is a small fraction of B1 extracted before the output mode cleaner (OMC) and B1s is the beam reflected by the OMC.*

This optical system is designed to detect the beams coming from the interferometer output ports. As already shown (Fig.2.4), the photodiode B1 (assembled on an external bench) is placed along the interference beam, and is used to measure the gravitational wave signal. The beam reflected from the second face of the BS impinges on the photodiode B5, assembled on the same bench of B1. The two beams transmitted through the 3 km-long cavities are detected by the two photodiodes B7 and B8 on the external optical benches of the terminal buildings. The beam re-

flected by the interferometer is monitored by the photodiode B2, assembled on the injection bench. Additional high quality optics are necessary to adapt the beam size to the photo-detectors, and to handle the several beams impinging on the detection bench. The main photodiode (B1) must detect variations of light power of 10^{-10} W at the modulation frequency, corresponding to a differential deformation of the arm length, smaller than 10^{-19} m. Additionally, the residual swing of the mirror at very low frequencies (of the order of 10^{-12} m, once the interferometer is locked) causes large fluctuations of the light intensity. This puts severe constraints on the dynamic range and residual noise of the photodiodes and their read-out system.

The OMC (see Fig.2.7) is a 2.5 cm-long triangular optical cavity, made by silica and with a Finesse of 50. The large cavity bandwidth (around 75 MHz) allows the transmission of both the carrier and the sidebands in the same Airy peak. As shown in Fig. 2.7, the interference pattern before the OMC is detected by the photodiode B1p. The cavity length is controlled by varying the OMC temperature, using a Peltier cell (that is a small solid-state heat pump made of a thin slab able to absorb or emit heat, depending on the current applied to its extremities). The OMC is kept on resonance by modulating the cavity length at 28 kHz with a piezoelectric device and detecting the error signal synchronously. In this way, the length of the cavity is controlled with an accuracy by about 10^{-10} m. Since a variation of the OMC length in the detection band would simulate the passage of a gravitational wave, the bench in vacuum is suspended from a short Superattenuator, in order to filter seismic vibrations. A Faraday isolator is also assembled on the suspended bench, in order to avoid the light being back scattered from the photodiodes and recombining with the main beam. The position of the suspended bench is controlled in feedback in all six degrees of freedom by using a digital camera as a sensor and coil- magnet actuators. The required accuracy in the detection band of a few 10^{-7} $rad/\sqrt{Hz}$

in angles and of few 10^{-8} $m/\sqrt{Hz}$ in the longitudinal degrees of freedom has been achieved.

2.3.4 *Sensitivity*

It is interesting to see how the various noise levels discussed above reflect on the sensitivity of an actual interferometer like the Virgo+ one (Fig. 2.8).

In Fig. 2.8 we can see the main limiting noises.

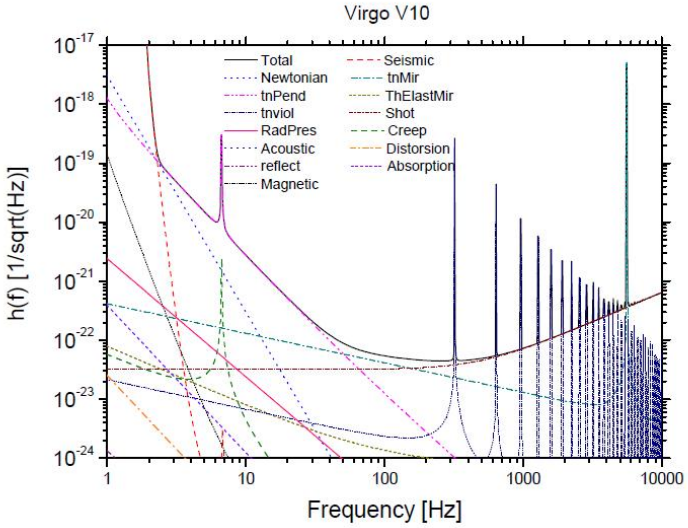

Figure 2.8: *Design sensitivity of Virgo, as a function of frequency. The coloured curves show the main limiting noises: seismic noise up to 4 Hz, thermal noise up to 100 Hz and shot noise at higher frequencies.*

Once the antenna is isolated from ground seismic noise, thermal displacements induced by pendulum dissipations in the mirror suspensions (pendulum thermal noise) limit the sensitivity up to a few tens of Hz.

At higher frequency, the thermal noise induced by dissipation inside the mirror (mir-

ror thermal noise) is dominant, up to a few hundreds of Hz.

Above this frequency, the antenna sensitivity is mainly suppressed by the shot-noise in the photo-detection. Many other spurious mechanisms, named technical noise, limit the interferometer performance.

During VSR2 the Virgo detector reached a sensitivity very close to the design one, see again Fig. 2.3.

Afterwards, the steel wire of the suspension has been replaced with fused silica

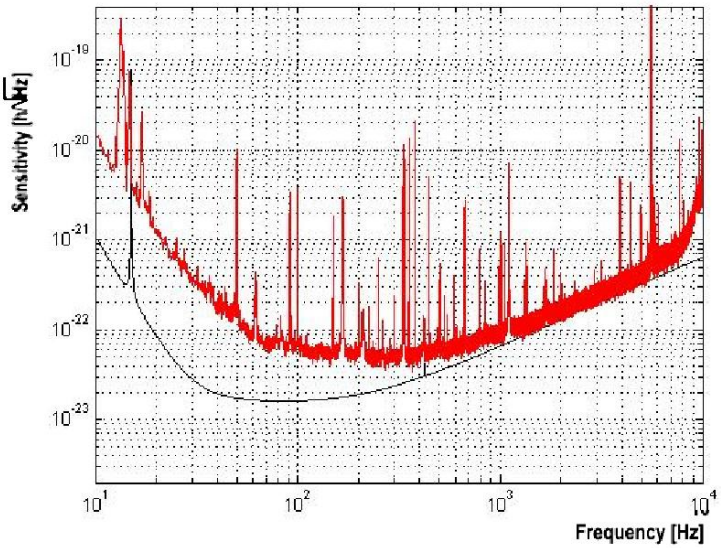

Figure 2.9: *Virgo+ design sensitivity with monolithic suspensions (black), compared to the VSR2 sensitivity (red).*

fibers monolithically. In this way dissipative processes are expected to be largely reduced resulting in lower thermal noise and better sensitivity at low frequency (see the Virgo+MS design curve in Fig. 2.3 and Fig. 2.9). However, with the VSR3, the detector sensitivity was not as good as expected and even slightly worse than the one obtained during VSR2. The main reason was that the four arm mirrors needed to be replaced and the new ones showed radius of curvature and losses asymmetries

much larger than before, resulting in a worse contrast of the interferometer. This in turn increased significantly the amount of spurious light reaching the output port, causing scattered light which was the main limiting noise source during VSR3. After the end of the run these problems have been tackled in two ways. A better dumping of the spurious light at dark port was implemented. Moreover a system to actively change the end mirror radius of curvature has been designed and installed. With these two systems it was possible to reduce by about a factor 3 the amount of power reaching the dark port and also to improve the interferometer contrast by a large amount. In this condition the fourth Virgo Science Run started, with improved sensitivity with respect to VSR2, see Fig. 2.3 and Fig. 2.10.

The most important result so far is the sensitivity improvement below 50 Hz. In

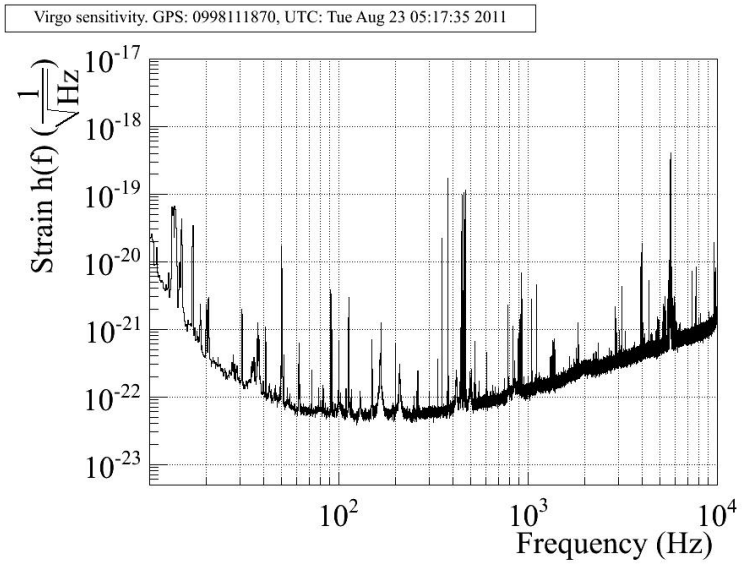

Figure 2.10: *The last measured Virgo sensitivity curve is shown here in the range 10 Hz-10 kHz.*

this region the noise level was significantly reduced with respect to before the monolithic suspension installation. More commissioning work will be needed to further

push the sensitivity significantly below the steel-wire thermal noise limit and fully demonstrate the improvemt coming from the installation of monolithic suspensions.

2.4 Advanced detector projects

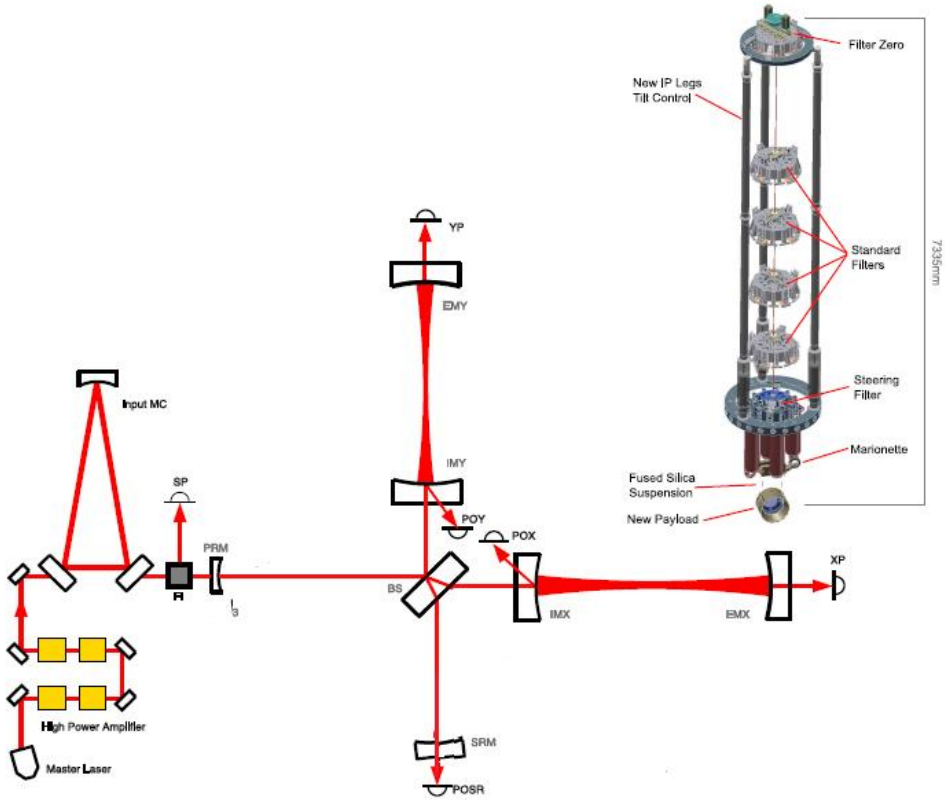

Figure 2.11: *Advanced Virgo Reference Design. Optical scheme, following the beam from the laser to the dark port: high power laser, triangular input mode cleaner, Faraday Isolator (FI), folded power recycling cavity, beam splitter, compensation plates, 3 km Fabry-Perot cavities, SR cavity, output mode cleaner, dark fringe photodiode. An image of the Virgo superattenuator is shown.*

The Advanced Virgo funding has been approved by INFN and CNRS at the end of 2009.

In order to increase the interferometer sensitivity at higher frequencies the laser input power will be around 200 W (with 125 W injected into the interferometer).

The AdV optical layout is illustrated in Fig. 2.11. In order to reduce the shot-noise, the light power circulating in the arms is maximized by increasing either the Finesse of the arm cavity up to around 900 (150 in Virgo+ and 50 in Virgo) and, according to the expected interferometer losses, the Finesse of the Power Recycling cavity (around 70). In this configuration, the laser power impinging on the beam splitter is 2.7 kW and 760 kW in the arm cavities.

A beam waist of 8.5 mm will be set close to the center of the cavity, in order to have a beam spot around 6 cm in radius on both cavity mirrors. These are the largest spots that can be accepted with a mirror small enough to be machined with a good optical surface.

The present baseline foresees the use of dual recycling Fabry-Perot Michelson Interferometer, so that there will be a combination of power recycling and signal recycling. The response of an interferometer with dual recycling is given by a combination of dual recycling parameters, and the arm cavity Finesse. The dual recycling mirror transmittance changes the Finesse of the dual recycling cavity, and so the bandwidth of the detector, whereas the fine tuning of the length affects the cavity central frequency and, as a consequence, the frequency of the antenna peak sensitivity.

The sensitivities achievable in Adv Virgo for different choices of the dual recycling parameters are discussed in Adv Virgo Baseline Design, 2009 [2]. It is important to stress that, once fixed the mirror transmittance is fixed, the tuning of the sensitivity peak can be performed remotely, by adjusting the dual recycling mirror position by just a few tens of nanometers.

2.4.1 *High Power Laser*

The Adv Virgo laser will have a power of about 200 W (four times that of Virgo+), with the goal to deliver at least 125 W in ITF input in the Gaussian fundamental mode, after mode filtering at the input of the injection system and the pre-mode cleaner, located on the external bench.

The laser is based on the so called DPSSL technology (Diode Pump Solid State Laser), that foresees the use of a master laser and two stages of amplification. The possibility to use a fiber amplifier to achieve these specifications is presently under study.

2.4.2 *Advanced Virgo Injection System*

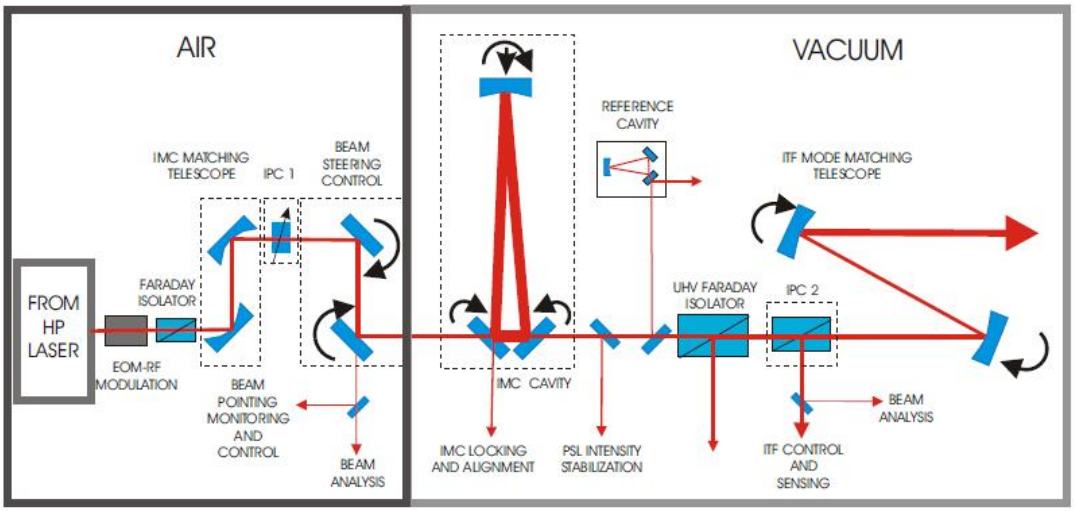

Figure 2.12: *Schematic of Advanced Virgo INJ subsystem baseline solution.*

The working principle of the Adv Virgo injection system is identical to the Virgo one, with the IMC used as a reference to lock the laser frequency, and the reference cavity to stabilize the IMC length in the low frequency range (see Fig. 2.12). The

same geometry, Finesse and reference cavity of Virgo, will be used. The main effort concerns the optical properties of the cavity mirrors, that must have a coating absorption below 1 ppm, and a RMS micro-roughness less than 1 nm. This will reduce thermal effects and diminish optical losses. Other stringent requirements for the Adv Virgo Injection system, such as a small intensity noise of the beam sent to the interferometer (that must be less than $3 \cdot 10^{-9}$ $\sqrt{Hz}$ at 10 Hz) are reported in [2]. After the IMC the intensity stabilization system, similar to the Virgo one, will provide the signal for stabilizing the laser relative intensity noise, and reach the requirements.

2.4.3 *Advanced Virgo Mirrors*

The baseline foresees the use of Fabry-Perot cavity mirrors with a diameter of 35 cm and a 20 cm thickness (the same diameter as the Virgo mirrors but twice as thick and heavy). This choice will enable reduction of the pendulum thermal noise (scaling with the inverse of the square root of the mirror mass) and the radiation pressure noise. A mirror substrate made by a new fused silica, with a bulk absorption three times smaller than the one used in Virgo (keeping the same quality factor, refraction index homogeneity, and residual strain) has been selected. The roughness of the mirror must be reduced from the present value of a few nm (corresponding to 300 ppm of optical losses) down to fractions of nm, to fulfill the requirement to have 75 ppm of optical losses. For what concerns the mechanical losses, the dominant dissipation mechanism in the mirror is still the coating. The lower dissipations have been measured on Ta2O5 (Tantalum Pentaoxide) coating, with a Ti doping (about 1.6 to 1.8 10^{-4}, in comparison with typical values around of $2 \cdot 10^{-4}$).

2.4.4 *Advanced Virgo Thermal Compensation System*

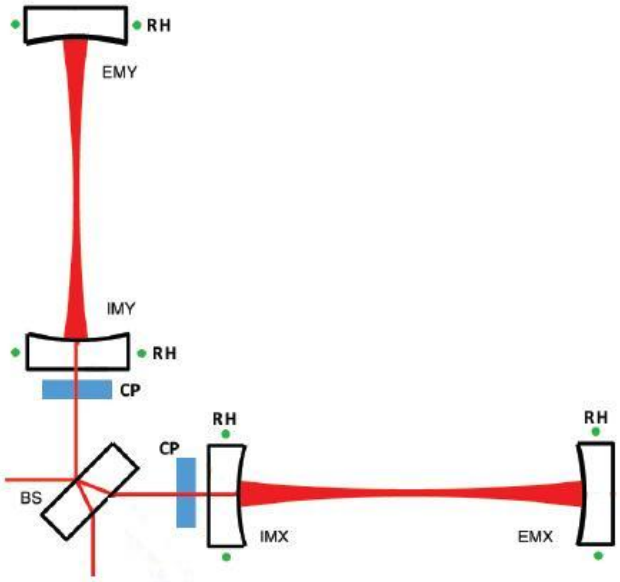

Figure 2.13: *Advanced Virgo TCS layout: the green dots represent the test masses shielded ring heaters, the blue rectangles represent compensation plates.*

The wave-front distortions and the deformation of the high reflectivity mirror surface are corrected by applying an external CO2 laser on both faces of each cavity input mirror (see Fig 2.13). As for Virgo+, the major problem concerns fluctuations of the laser intensity that can induce a spurious displacement of the mirror. In Adv Virgo the relative intensity noise of the CO2 laser must be reduced by about a factor ten with respect to Virgo+. This requirement is considered too challenging, and thus a new transmission optic (Compensation Plate) will be suspended to the Superattenuator in the recycling cavity, behind the input mirror. The CO2 laser will be used to adjust the lens compensation in order to correct for the optical wave front distortion occurring on the mirror. In this way, the CO2 laser radiation pressure has no effect on the high reflectivity surface of the mirror in the cavity, where the

measurement of the arm differential motion (i.e. of the gravitational wave effect) takes place.

2.4.5 *Other Improvements*

A total pressure of 10^{-9} mbar is necessary to ensure the noise induced by the residual gas is below the lowest point of the Adv Virgo sensititivity curve (around $3 \cdot 10^{-24} \frac{1}{Hz}$ at 300 Hz). Cryogenic traps will be used to separate the long pipes containing the arms of the interferometer and the central area vacuum chambers, where the Superattenuator and the optical payloads are located. This will allow a bake-out to be performed on the tube, without affecting the sophisticated components around the mirrors and its suspensions. Significant work will be necessary on the Virgo infrastructure to reduce the anthropogenic noise inside the experimental buildings. In particular, quieter machines and adequate acoustically insulated rooms around the external benches will be implemented. The strategy to achieve a stable locking and alignment, and the corresponding control noise, are to be determined. High accuracies (two orders of magnitude better than Virgo) in longitudinal length control will be required in order to avoid the re-injection of noise due to beam power fluctuations.

The locking of a high-Finesse cavity is a challenging operation, since the crossing time of the resonance gets smaller as the Finesse increases. One technique to overcome this problem is to use an additional laser, with a different wavelength in order decrease mirror reflectivity (5-15 %), and thus lower cavity Finesse. Once the cavity is locked on the additional laser, it is set in a deterministic way to its working point, where the main laser is at the resonance, and the main error signals can be used. An offset in the auxiliary laser error signals is introduced, and a smooth transition to lock the cavity on the interferometer laser can be performed.

2.4.6 *Advanced Virgo Design Sensitivity*

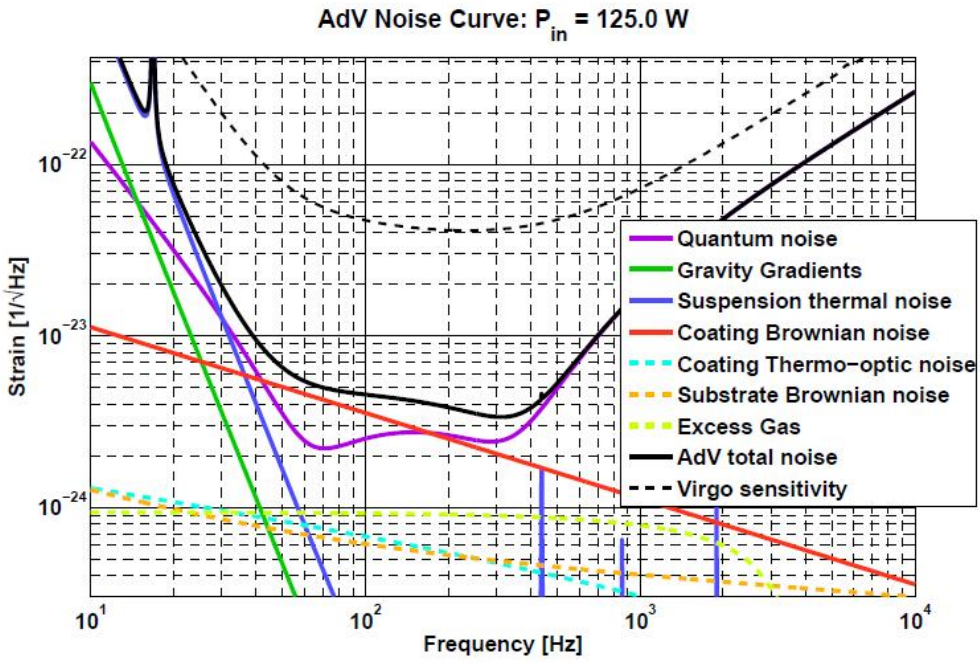

Figure 2.14: *Reference Advanced Virgo sensitivity and expected noise contributions. It has been calculated with SR mirror transmittance of 11 % and SR phase of 0.15 rad, 125 W of laser power entering the interferometer, cavity finesse of 888 and PR factor of 21.5. The chosen SR tuning optimizes the inspiral range for coalescing binary neutron stars. The Virgo design sensitivity is shown for the sake of comparison.*

The Adv Virgo detector has the goal to contribute bringing the gravitational waves into maturity, by achieving an improvement in sensitivity of about a factor of 10 or better with respect to the initial Virgo design sensitivity.
Adv Virgo will harvest its scientific potential thanks to the close collaboration with the Advanced LIGO detectors, constituting a long baseline network of observatories, capable to coherently exploit the time, amplitude and phase information coming

from the different sites, thus reconstructing the source position, the polarization of the impinging waves, ultimately giving access to the physics of the sources.
The Adv Virgo reference sensitivity as well as the main noise contributions are shown in Fig. 2.14. The curve is calculated using the parameters in tables 2.1 and 2.2.

The SR parameters have been chosen in order to maximize the sight distance for Binary Neutron Stars (BNS). The corresponding inspiral ranges are $\approx$ 150 Mpc for BNS and $\approx$ 1.1 Gpc for 10 $M_{\odot}$ Binary Black Holes (BBH).
As already mentioned, the presence of the SR cavity allows to think of Adv Virgo as a tuneable detector: the sensitivity curve can be shaped in order to optimize it for targeting different astrophysical sources. The SR mirror transmittance influences the detector bandwidth, while the microscopic lenght of the SR cavity changes the frequency of the maximal sensitivity.
Fig. 2.15 shows some examples of sensitivity curves obtained with different tunings. With respect to the reference sensitivity (optimized for BNS) one can:

- enhance the low frequency response in order to increase the detectability of large mass BBH (green curve in Fig. 2.15). This also requires lowering the input power;
- enhance the sensitivity in a certain frequency range, narrow banding the response (cyan curve in Fig. 2.15). This is indicated to target young pulsars;
- widen the detector response and increase the high frequency sensitivity for burst search (blue curve in Fig. 2.15).

AdV Overview, Part I		
Subsystem and Parameters	**AdV Preliminary Design**	**Initial Virgo Implementation**
mycolor **Sensitivity**		
Binary Neutron Star Inspiral Range	145Mpc	11Mpc
Anticipated Strain Sensitivity	$3.5 \cdot 10^{-24}/\sqrt{Hz}$	$4 \cdot 10^{-23}/\sqrt{Hz}$
Displacement Sensitivity	$1 \cdot 10^{-20}\ m/\sqrt{Hz}$	$1 \cdot 10^{-19}\ m/\sqrt{Hz}$
mycolor **Instrument Topology**		
Interferometer	Michelson	Michelson
Power Enhancement	Arm cavities and Power Recycling	Arm cavities and Power Recycling
Signal Enhancement	Signal Recycling	n.a.
mycolor **Laser and Optical Powers**		
Laser Wavelength	1064 nm	1064 nm
Optical Power at Laser Output at least	165W	20W
Optical Power at Interferometer Input	125W	8W
Optical Power at Test Masses	760 kW (TBC)	4 kW (TBC)
Optical Power on Beam Splitter	2.7 kW	0.3 kW
mycolor **Test Masses**		
Mirror Material	Fused Silica	Fused Silica
Main Test Mass Diameter	35 cm	35 cm
Main Test Mass Weight	42 kg	21 kg
mycolor **Test Mass Surfaces and Coatings**		
Coating Material	Ti doped Ta_2O_5	Ta_2O_5
Roughness	$<$ 1 Angstrom	$<$ 0.5 Angstrom
Flatness	0.5 nm RMS	$<$8 nm RMS
Losses per Surface	37.5 ppm	250 ppm (measured)
Test Mass ROC	Input Mirror = 1416m End Mirror = 1646m	Input Mirror = flat End Mirror = 3600m
Beam Radius at Input Mirror	56mm	21mm
mycolor **Thermal Compensation**		
Thermal Actuators	CO_2-Lasers and Ring Heater	CO_2-Lasers
Actuation Points	Compensation Plates and directly at Mirrors	Directly at Mirrors

Table 2.1: *Main parameters of the AdV Preliminary Design (PART I)*

AdV Overview, Part II		
Subsystem and Parameters	**AdV Preliminary Design**	**Initial Virgo Implementation**
mycolor **Suspension**		
Seismic Isolation System	Superattenuator	Superattenuator
Degrees of Freedom of Inverted Pendulum Inertial Control	6	4
Suspension Fibres	Fused Silica Fibres (tapered)	Steel Wires
mycolor **Vacuum System**		
Pressure	$2 \cdot 10^{-9}$ *mbar*	$2 \cdot 10^{-7}$ *mbar*
mycolor **Injection System**		
Input mode cleaner throughput	$> 90\%$	85% (meas.)
mycolor **Detection System**		
GW Signal Readout	DC-Readout	Heterodyne (RF)
Output Mode Cleaner Suppression	RF Sidebands and Higher Order Modes	Higher Order Modes
Main Photo Diode Environment	in Vacuum	in Air
mycolor **Lengths**		
Arm Cavity Length	3 km	3 km
Input Mode Cleaner	144m	144m
Power Recycling Cavity	24m	10m
Signal Recycling Cavity	TBD	n.a.
mycolor **Test Masses**		
Mirror Material	Fused Silica	Fused Silica
Main Test Mass Diameter	35 cm	35 cm
Main Test Mass Weight	42 kg	21 kg
mycolor **Interferometric Sensing and Control**		
Lock Acquisition Strategy	Auxiliary Lasers (different wavelength)	Main Laser
Number of RF Modulations	3	1
Schnupp Asymmetry	4 cm	85 cm
Recycling Cavity Design	Non-degenerate	Marginally stable
mycolor **Signal Recycling Parameter**		
Signal Recycling Mirror Transmittance	11%	n.a.
Signal Recycling Tuning	0.15 rad	n.a.

Table 2.2: *Main parameters of the AdV Preliminary Design (PART II)*

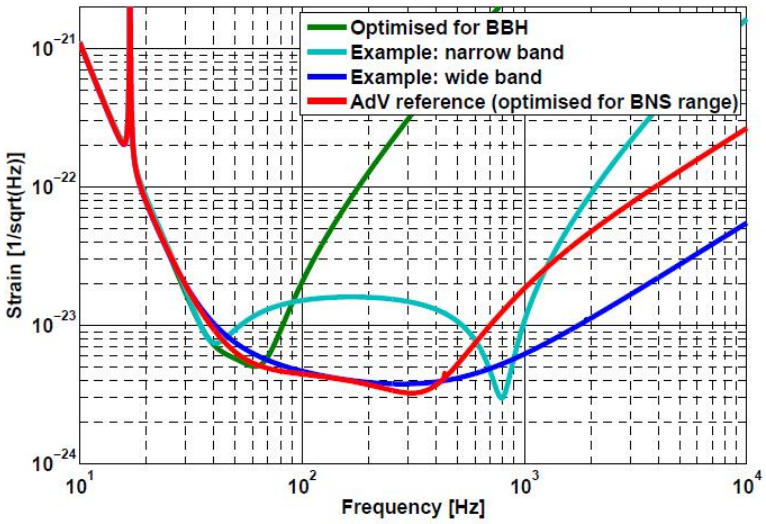

Figure 2.15: *Tuning the Adv Virgo sensitivity by changing the SR parameters. The red curve corresponds to the reference sensitivity of Fig. 2.14 and maximizes the inspiral range for BNS. The green curve is optimized for BBH detection (BH of 10 $M_\odot$ are considered) and is obtained with a low input power (9 W). The cyan curve shows a narrow band tuning, useful to target a monochromatic source, while the blue "wide-band" tuning allows to improve the high frequency sensitivity .*

Chapter 3

Beam Jitter Noise Contribution in Virgo and Advanced Virgo

The VIRGO Science Collaboration plans to upgrade the currently commissioned VIRGO interferometer with the second generation detectors. Advanced VIRGO detectors are designed to have sensitivities near the standard quantum-limit (SQL). This requires that all technical and not-fundamental noise sources are well suppressed. One of these technical noise sources is the beam jitter in conjunction with slightly misaligned mirrors.

As beam jitter is intended the time dependent changes in the location or propagation direction of the impinging laser field originates in the laser and at unsuspended optical components which steer the laser into the main interferometer.

Practically, these fluctuations in position and in direction of the input laser couple to misalignments of the mirrors forming the interferometer and potentially decrease the detector sensitivity.

So, the fundamental source for beam jitter noise is any motion of the optical elements at the Input of the Interferometer (like the mode matching telescope).

The laser jitter effects can be neglected when their contribution to the dark fringe is at least one order of magnitude smaller than the contributions from the fundamental noise sources (this "rule" applies to all technical noise).
In Fig. 3.1 we can observe the jitter noise projection on Virgo sensitivity: comparison with Virgo+ design curve.
We can see that the beam jitter limits the sensitivity at around 40Hz.

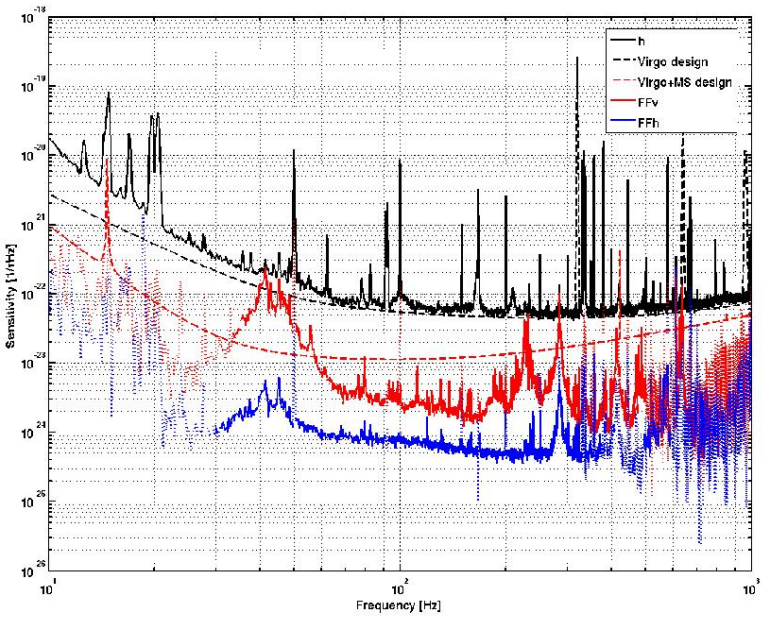

Figure 3.1: *Jitter noise projection on Virgo sensitivity: comparison with Virgo+ design curve.*

In the other regions it would be compliant with Virgo but it is not sufficiently low to be compliant with Virgo+ sensitivity.
In Ad-Virgo the sensitivity will be a factor 10 higher than Virgo and so the beam jitter noise for Adv Virgo won't be negligible if the injection system is not improved.

For frequencies under 100 Hz, as shown in Fig. 3.2 and in the follows sections, we show in the following that this issue comes from the vibrations of the two injection benches: Laser Bench (LB) and External Injection Bench (EIB) (see Fig. 2.6).

To improve the beam jitter at low frequency, we propose to place the optical

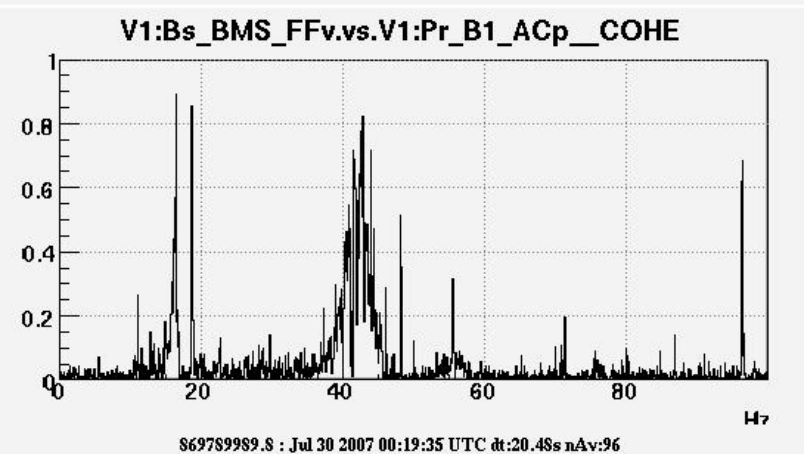

Figure 3.2: *Correlation between the vertical BMS photodiode and the dark fringe for frequencies below than 100 Hz.*

benches on pneumatic isolation systems enabling to lower the seismic noise by a factor of 100 at 10 Hz.

In following part of PhD work will be shown: it consists in modeling analytically the whole chain of beam jitter noise propagation from the laser to the dark port, to set requirements for the systems.

Starting from the Virgo optical layout, a preliminary step has been to evaluate how the seismic vibrations of the optical injection system are coupled to spurious misalignments of the interferometer mirrors. Only after, it has been possible to take into account the Adv Virgo optical configuration. In case of Adv Virgo, the optical layout is remarkable more complex and a detailed analysis has been necessary to set the critical parameters and requirements in order to obtain a beam jitter noise low

enough to be compliant with Adv-Virgo sensitivity.

3.1 Estimation of Input Beam Jitter at Input of Interferometer

In this section it is described the formalism which can be used to study the problem of dynamic misalignments in the injection system, in particular how the seismic vibrations of the optical injection system are coupled to the TEM00 input beam.
In Fig. 3.3 it is shown an arrangement of the interferometer input optical benches that we take in account in the analytical analysis of the beam jitter noise. The goal

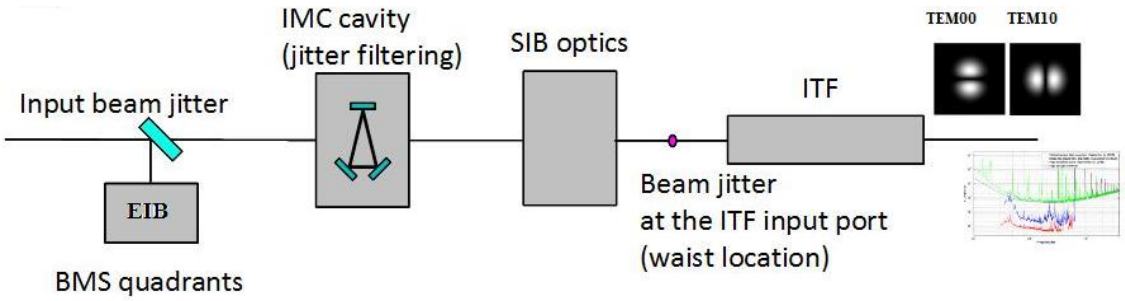

Figure 3.3: *Arrangement of the interferometer injection system composed of: laser bench "LB", external injection bench "EIB", where it is installed the monitoring system of the beam "BMS" which is used to keep the laser beam in a fixed position, the input mode cleaner "IMC" for the spatially filtering of beam (selecting the TEM00 mode) and the suspended injection bench where it is mounted the input beam mode-matching telescope.*

is to characterize the angular misalignment at the injection system output and so, at interferometer input.
The general concept of using the ABCD matrix formalism is explained in the next

sections.

We used a suitably extended formalism to analyses the off-axis path of the beams in the injection system.

3.1.1 *Input Beam Jitter with respect to Optical Bench Motion*

In this section we want to estimate how the motion of the optical bench (EIB) is creating beam jitter trough the optics on the bench, Fig. 3.4.

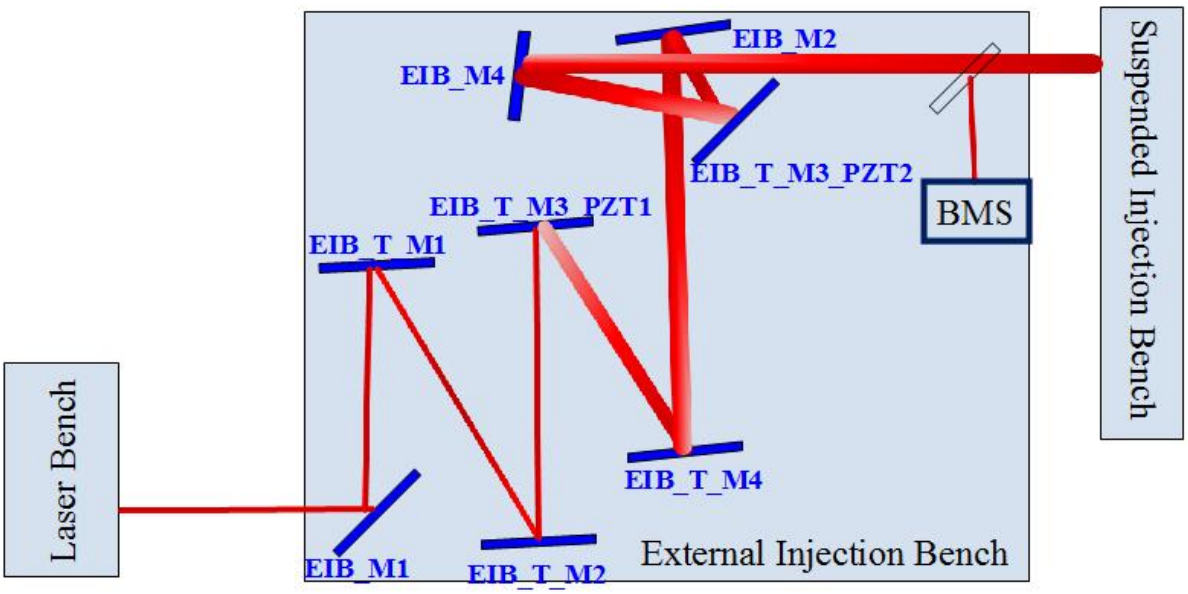

Figure 3.4: *System Layout.*

For this purpose, as a first approximation, we can assume that the beam coming from the LB, appears to be perfectly aligned with the optical axis and we want to evaluate what is the jitter of the beam at the output of the EIB when the optical elements mounted on the bench are tilted or displaced with respect the optical axis

due to seismic vibrations of the EIB itself.

Using the ray matrix algebra, in one degree of freedom:

- the input beam will be described by a column vector $(x_{in}, \alpha_{in}, 1)$ where x_{in} and α_{in} are the longitudinal and angular misalignments;
- the optics will be described by a convenient 3x3 matrix "ABCDEF";
- the beam transmitted by the optical system will be a column vector $(x_t, \alpha_t, 1)$, given by:

$$\begin{pmatrix} x_t \\ \alpha_t \\ 1 \end{pmatrix} = \begin{pmatrix} A & B & E \\ C & D & F \\ 0 & 0 & 1 \end{pmatrix} * \begin{pmatrix} x_{in} \\ \alpha_{in} \\ 1 \end{pmatrix}$$

In the ideal case where the input beam is not misaligned, we can write:

$$\begin{pmatrix} x_t \\ \alpha_t \\ 1 \end{pmatrix} = \begin{pmatrix} E \\ F \\ 1 \end{pmatrix}$$

In the real case, the input beam is not perfectly aligned with the optical axis, so the input jitter is coupled with the seismic motion of the EIB optics through the submatrix $\begin{pmatrix} A & B \\ C & D \end{pmatrix}$ and the transmitted jitter at the EIB output will be given by:

$$\begin{pmatrix} x_t \\ \alpha_t \\ 1 \end{pmatrix} = \begin{pmatrix} Ax_{in} + B\alpha_{in} + E \\ Cx_{in} + D\alpha_{in} + F \\ 1 \end{pmatrix}$$

We summarize a calculation of the beam jitter noise at the output of EIB.

The figure 3.4 shows the setup used in this calculation. It defines several lengths and mirrors (listed in the Table 3.1).

Parameter	l_0	l_1	l_2	l_3	l_4	l_5	l_6	l_7	l_8
Value	0.165	0.596	0.627	0.635	0.426	0.896	0.207	0.207	4.790
Mirror	EIB_M_1	$EIB\_T\_M_1$	$EIB\_T\_M_2$	$EIB\_T\_M_3\_PZT1$	$EIB\_T\_M_4$	EIB_M_2	EIB_M_4	$EIB\_T\_M_3\_PZT2$	
R(mm)	∞	500	750	-800	1600	∞	∞	∞	
θ	-45	3	-3	4.9	-5.1	7.51	-44.8	82.52	

Table 3.1: *Parameters of Optical Layout*

Every optical element on EIB will be describe using the ray tracing matrix in table 3.2 and the total matrix will be given by the products between these matrices.

	Meridian Plane	**Sagittal Plane**
Free Space Matrix	$\begin{pmatrix} 1 & L & 0 \\ 0 & 1 & 0 \\ 0 & 0 & 1 \end{pmatrix}$	$\begin{pmatrix} 1 & L & 0 \\ 0 & 1 & 0 \\ 0 & 0 & 1 \end{pmatrix}$
Reflection matrix from a spherical mirror	$\begin{pmatrix} -1 & 0 & N_i \frac{\sin 2\theta_i}{\cos\theta_i} \\ \frac{2}{R_i \cos\theta_i} & -1 & 2\alpha_i - \frac{2}{R_i \cos\theta_i} N_i \sin\theta_i + \frac{2}{R_i \cos\theta_i} T_i \cos\theta_i \\ 0 & 0 & 1 \end{pmatrix}$	$\begin{pmatrix} 1 & 0 & 0 \\ -\frac{2\cos\theta_i}{R_i} & 1 & 2\beta_i - \frac{2\cos\theta_i}{R_i} H_i \\ 0 & 0 & 1 \end{pmatrix}$
Reflection matrix from a flat mirror	$\begin{pmatrix} -1 & 0 & N_i \frac{\sin 2\theta_i}{\cos\theta_i} \\ 0 & -1 & 2\alpha_i \\ 0 & 0 & 1 \end{pmatrix}$	$\begin{pmatrix} 1 & 0 & 0 \\ 0 & 1 & 2\beta_i \\ 0 & 0 & 1 \end{pmatrix}$

Table 3.2: *Ray matrices for optical components: θ is the angular position of the mirror; α is the angular deviation from θ in the meridian plane; β is the angular deviation from 90° in the sagittal plane; T and N are the mismatches in meridian plane; H in the mismatch along the vertical direction*

To simplify, we take in account one degree of freedom (vertical misalignments). At 10Hz the input beam vertical jitter is estimated to be $10^{-8} \frac{rad}{\sqrt{Hz}}$ at PMC [25]. The vertical seismic motion of the EIB, measured through the accelerometer placed

on the bench (Em_SEBDCE09 signal), is shown in Fig. 3.5.

We will assume that the transfer function between the bench and the optics is

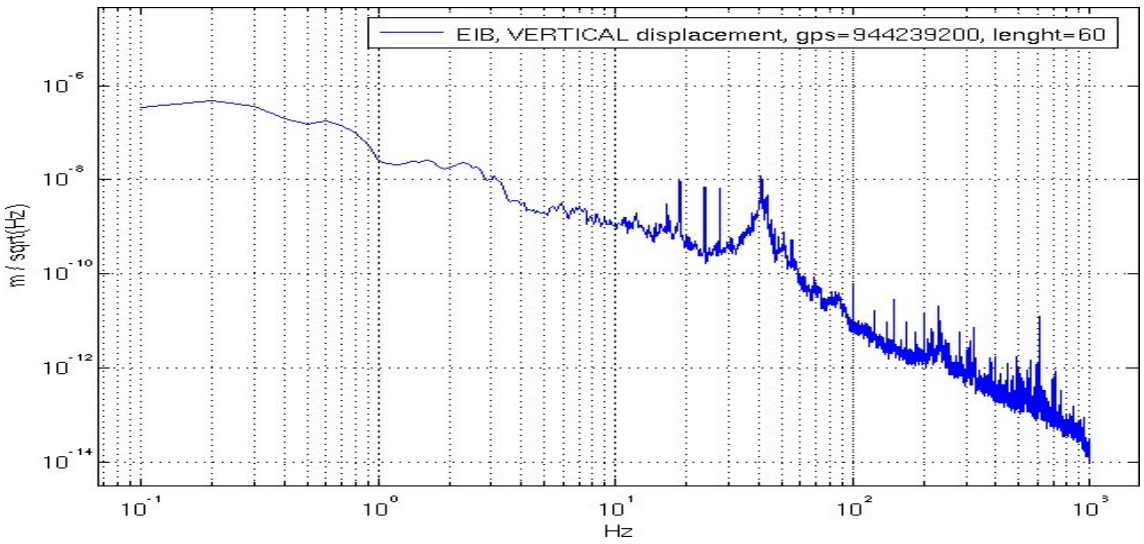

Figure 3.5: *EIB vertical displacement.*

equal to 1, we think of any optical element will move in the same way as the bench. So that H_i and β_i introduced in Table 3.2 are given by Em_SEBDCE09 signal. Given the frequency dependency of the input beam jitter $(\tilde{y}_{in}, \tilde{\beta}_{in})$ and of the optics tilts and shifts on the EIB (H_i, β_i), we can obtain the contribution of the injection system to the beam jitter at the IMC input (Fig. 3.6).

Using the ABCDEF matrix, we can write:

$$\tilde{y}_t = \sqrt{|A\tilde{y}_{in}|^2 + \left|B\tilde{\beta}_{in}\right|^2 + |E|^2} \tag{3.1}$$

$$\tilde{\beta}_t = \sqrt{|C\tilde{y}_{in}|^2 + \left|D\tilde{\beta}_{in}\right|^2 + |F|^2} \tag{3.2}$$

Where $\tilde{y}_t$ is the frequency dependent vertical displacement and $\tilde{\beta}_t$ is the frequency dependent vertical tilt at IMC input.

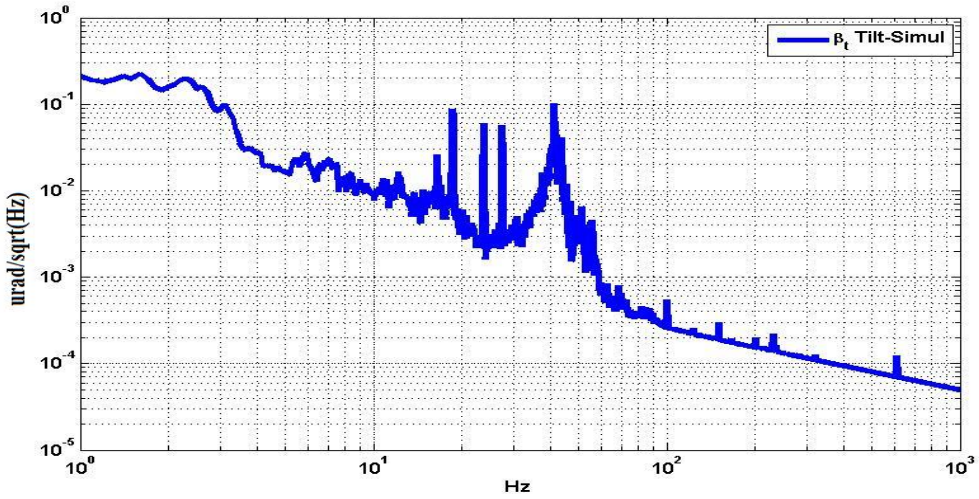

Figure 3.6: *Frequency dependent angular jitter obtained through analytic model.*

The model obtained is checked with the measurements realized through the BMS (figure 3.7) and we can observe that the data obtained are comparable in a frequency range $20Hz < f < 100Hz$.

To $f > 100Hz$ we are limited by the read noise introduced by the photodetector.

To $f < 20Hz$ we are limited by the BMS closed loop (controller noise).

The relationship obtained between the EIB motion and the beam at IMC input allows us to estimate the jitter contribution at IMC input monitoring the motion of the EIB optical elements.

Through this model, eventually, we could propose how to optimize the telescope (modifying the matrix) to minimize the most critical tilt/shift signals.

3.1.2 *Input Mode Cleaner Filtering*

We want to assess the input jitter filtering effect of the IMC assuming that the MC is perfectly static.

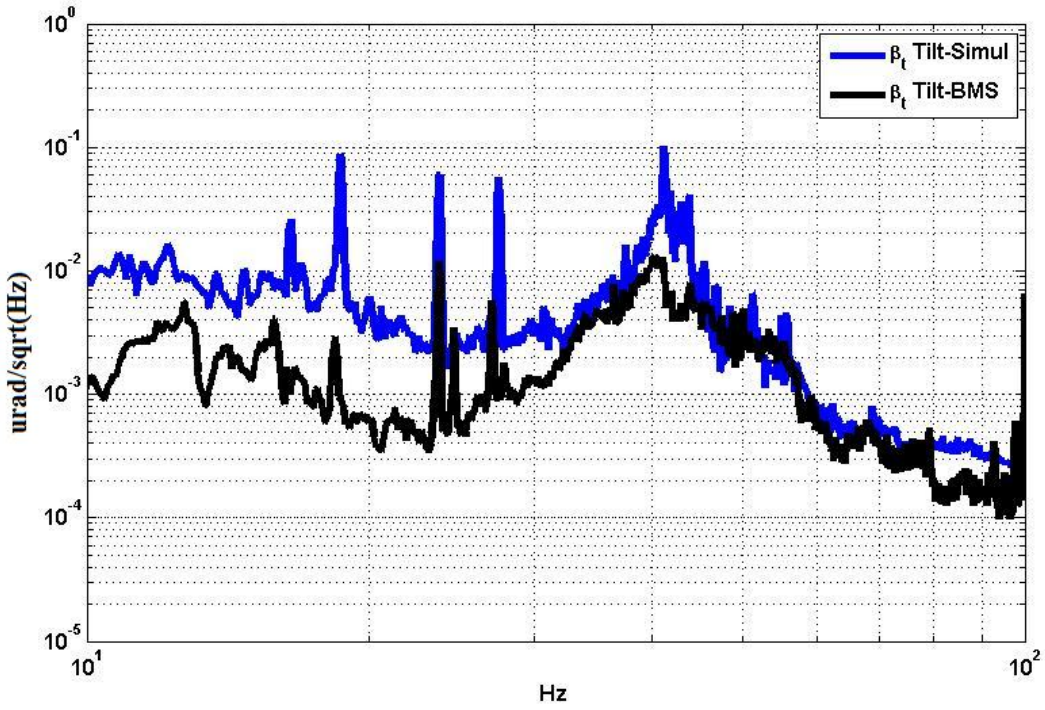

Figure 3.7: *Comparison between the computed and measured jitter at the output of the EIB.*

To this purpose we write the field at the IMC input in term of Hermite-Gauss modes.

As we know, an undistorted field can be spatially described by a mode TEM_{00}; any jitter, tilt or displacement, of the beam can be described at first order by two sidebands at frequencies ω_j with respect to the carrier with spatial mode TEM_{10} (in meridian plane), TEM_{01} (in sagittal plane) and amplitude dependents by the jitter (Fig. 3.8).

$$E = E_0 \left\{ \psi_{00} + \left(\frac{x_t}{w_o} - i\frac{\alpha_t}{\alpha_0} \right) \cos(\omega_j t)\psi_{10} + \left(\frac{y_t}{w_o} - i\frac{\beta_t}{\beta_0} \right) \cos(\omega_j t)\psi_{01} \right\} e^{i\omega_0 t} \quad (3.3)$$

To know how the jitter is transmitted by IMC, we must know how this cavity filters

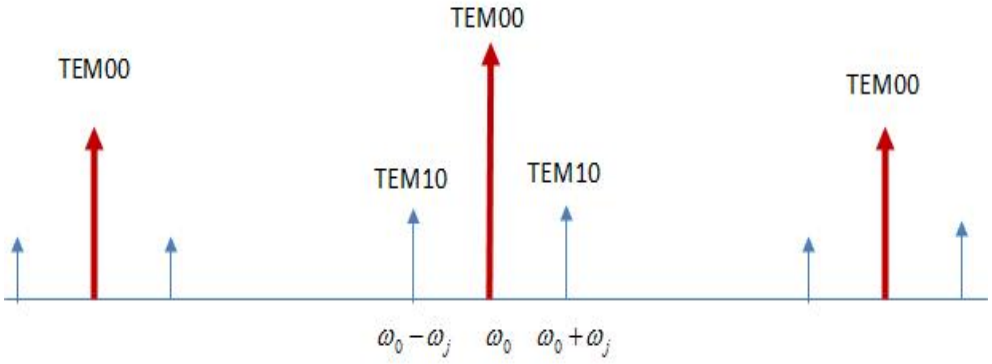

Figure 3.8: *Graphic description of a distorted field how a carrier and two sidebands produces by jitter.*

the TEM_{10} and TEM_{01}.

For a linear cavity the transverse vertical and horizontal modes have the same resonance frequency.

For a ring cavity this is is not true.

If the cavity has an odd number of mirrors (as the IMC), the modes TEM_{mn} with an odd mode number relative to the the ring plane (m =odd) are not degenerate with the modes TEM_{nm} having the same mode number relative to the plane perpendicular to the ring .

The cavity geometric form breaks the modes degeneracy.

After a round trip, the phase shift φ_{mn} is different for a beam horizontally symmetric and anti-symmetric.

As shown in figure 3.9, for a m+n=3 mode, the odd modes (1,2) are anti-symmetric to respect with the optical axis, the horizontally even modes (2,1) are symmetric.

A beam with a field distribution horizontally anti-symmetric to respect with the optical axis takes a geometrical π phase shift after a round trip. So,the total phase

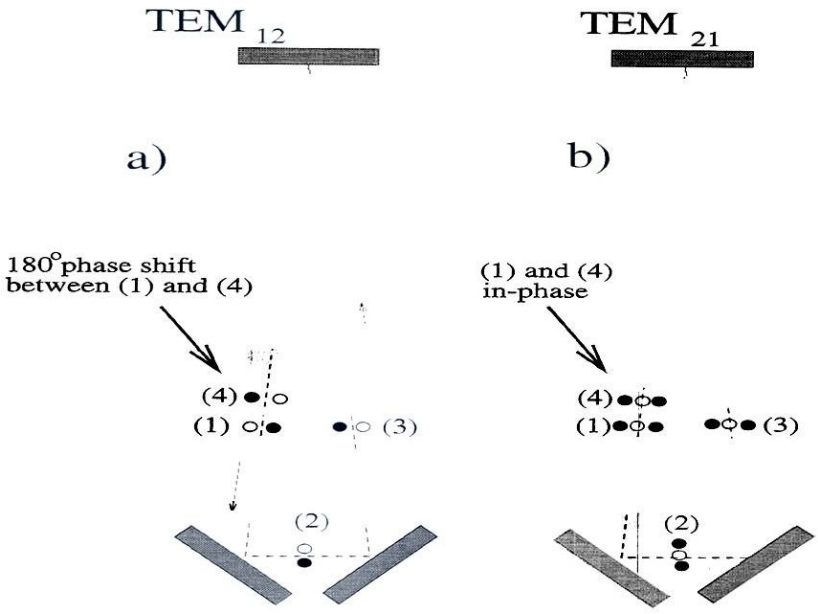

Figure 3.9: *Propagation in the ring plane for $m+n=3$. After a round trip, the beam horizontally symmetric (b) resonates in the cavity while the beam horizontally anti-symmetric (a) can't resonate because it takes a π phase shift due to the geometry*

$2\varphi_{mn}$ will be:

$$2\varphi_{mn}(z) - 2kz + \quad 2(1+m+n)\arccos\left[\left(1-\frac{L}{R_1}\right)\left(1-\frac{L}{R_2}\right)\left(1-\frac{L}{R_3}\right)\right]^{\frac{1}{2}} = \\ = \begin{cases} 0, & m \text{ even} \\ \pi, & m \text{ odd} \end{cases}$$

This degeneracy breaking causes a different vertical and horizontal jitter filtering because of the cavity transmission coefficient (t_{mn}) that depends on φ_{mn}:

$$t_{mn} = \frac{t_1 t_2}{1 + r_1 r_2 r_3 e^{2i\varphi_{mn}}} \tag{3.4}$$

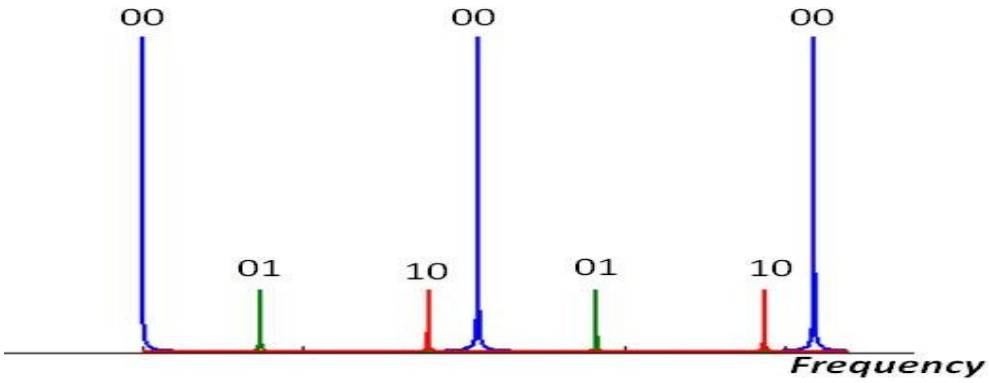

Figure 3.10: *Mode spectrum of a ring triangular cavity*

So that we will have $t_{10} \neq t_{01}$ and for a static tilt or displacement we can write:

$$E_T = E_0 \left\{ t_{00}\psi_{00} + t_{01}\left(\frac{x_t}{w_o} - i\frac{\alpha}{\alpha_0}\right)\psi_{01} + t_{10}\left(\frac{y_t}{w_o} - i\frac{\beta_t}{\beta_0}\right)\psi_{10} \right\} \tag{3.5}$$

Then, looking at the phase, we can say that the mode TEM_{10} is shifted by one half FSR with respect to TEM_{01} as in figure 3.10. As we know we can always write: $t_{mn} = |t_{mn}|e^{i\theta_{mn}}$.

Simple algebra can tell us that if TEM_{00} is at resonance $t_{mn} = \frac{t_1 t_2}{1 - r_1 r_2 r_3 e^{-2iX_{mn}}}$. It follows:

$$|t_{mn}| = \left(\frac{t_1 t_2}{1 + r_1^2 r_2^2 r_3^2 - 2r_1 r_2 r_3 \cos\left(2X_{mn}\right)}\right)^{1/2} = \frac{|t_{00}|}{\sqrt{1 + \frac{4F^2}{\pi^2}\sin^2 X_{mn}}} \tag{3.6}$$

with $|t_{00}| = \frac{t_1 t_2}{1 - r_1 r_2 r_3} \approx 1$

$$\theta_{mn} = \arctan\left(\frac{r_1 r_2 r_3 \sin 2X_{mn}}{1 - r_1 r_2 r_3 \cos 2X_{mn}}\right) \tag{3.7}$$

Where:

$$X_{mn} = \begin{cases} (m+n)\arccos\sqrt{1 - \frac{L}{R}}, & \text{if } m \text{ is even,} \\ -\frac{\pi}{2} + (m+n)\arccos\sqrt{1 - \frac{L}{R}}, & \text{if } m \text{ is odd.} \end{cases}$$

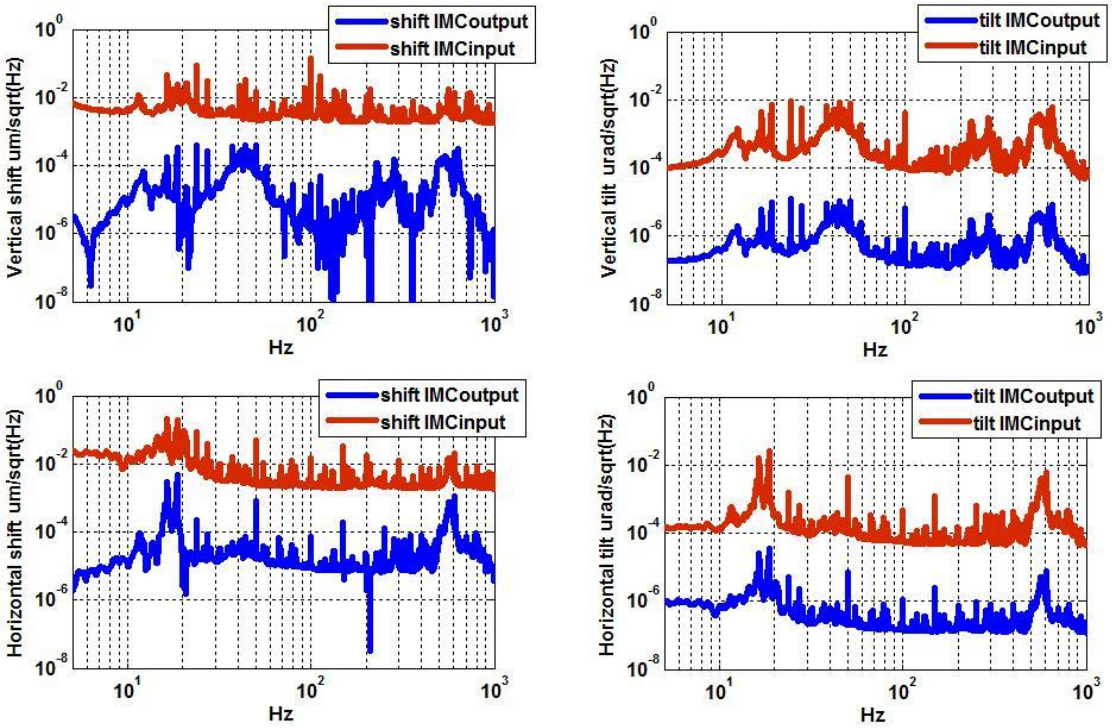

Figure 3.11: *Vertical and Horizontal Tilt/Shift at the IMC output.*

Using the Virgo parameters, the Mode cleaner provides a filtering of about 1/670 for the vertical jitter and 1/339 for the horizontal jitter.
If we have $\tilde{\beta}_t \approx 10^{-9} rad/\sqrt{Hz}$, we obtain $\tilde{\beta}_{MC} \approx 1.49 \cdot 10^{-12} rad/\sqrt{Hz}$ at the IMC output, (see Fig. 3.11).

3.1.3 *Calculation of Beam Jitter at the Input of the Interferometer*

In this section we take in account that between the IMC output and the input of ITF, there is the ITF mode matching telescope (Fig. 3.12).

So, we will compute how the jitter is transformed between these two places by

Figure 3.12: *Setup of ITF mode matching telescope.*

computing the matrix of the telescope.

In this case we will take into account an optical system perfectly aligned with the optical axis and an input beam misalignment given by Eq.3.5.

To describe the optical system we can use a simple 2x2 matrix given by:

$$\begin{aligned}\begin{pmatrix} A_s & B_s \\ C_s & D_s \end{pmatrix}_{SagittalPlane} = & \begin{pmatrix} 1 & l5 \\ 0 & 1 \end{pmatrix} \cdot \begin{pmatrix} 1 & 0 \\ -1/f4 & 1 \end{pmatrix} \cdot \begin{pmatrix} 1 & l4 \\ 0 & 1 \end{pmatrix} \cdot \\ & \cdot \begin{pmatrix} 1 & 0 \\ -1/f3 & 1 \end{pmatrix} \cdot \begin{pmatrix} 1 & l3 \\ 0 & 1 \end{pmatrix} \cdot \begin{pmatrix} 1 & 0 \\ -1/f2 & 1 \end{pmatrix} \cdot \\ & \cdot \begin{pmatrix} 1 & l2 \\ 0 & 1 \end{pmatrix} \cdot \begin{pmatrix} 1 & 0 \\ -1/f1 & 1 \end{pmatrix} \cdot \begin{pmatrix} 1 & l1 \\ 0 & 1 \end{pmatrix} \end{aligned} \tag{3.8}$$

$$\begin{aligned}\begin{pmatrix} A_m & B_m \\ C_m & D_m \end{pmatrix}_{MeridianPlane} = & \begin{pmatrix} 1 & l5 \\ 0 & 1 \end{pmatrix} \cdot \begin{pmatrix} -1 & 0 \\ 1/f4 & -1 \end{pmatrix} \cdot \begin{pmatrix} 1 & l4 \\ 0 & 1 \end{pmatrix} \cdot \\ & \cdot \begin{pmatrix} -1 & 0 \\ 1/f3 & -1 \end{pmatrix} \cdot \begin{pmatrix} 1 & l3 \\ 0 & 1 \end{pmatrix} \cdot \begin{pmatrix} -1 & 0 \\ 1/f2 & -1 \end{pmatrix} \cdot \\ & \cdot \begin{pmatrix} 1 & l2 \\ 0 & 1 \end{pmatrix} \cdot \begin{pmatrix} -1 & 0 \\ 1/f1 & -1 \end{pmatrix} \cdot \begin{pmatrix} 1 & l1 \\ 0 & 1 \end{pmatrix} \end{aligned} \tag{3.9}$$

So, the vertical displacement and tilt at ITF input will be:

$$\tilde{y}_0 = \sqrt{|A_s \cdot \tilde{y}_{MC}|^2 + \left|B_s \cdot \tilde{\beta}_{MC}\right|^2} \tag{3.10}$$

$$\tilde{\beta}_0 = \sqrt{|C_s \cdot \tilde{y}_{MC}|^2 + \left|D_s \cdot \tilde{\beta}_{MC}\right|^2} \tag{3.11}$$

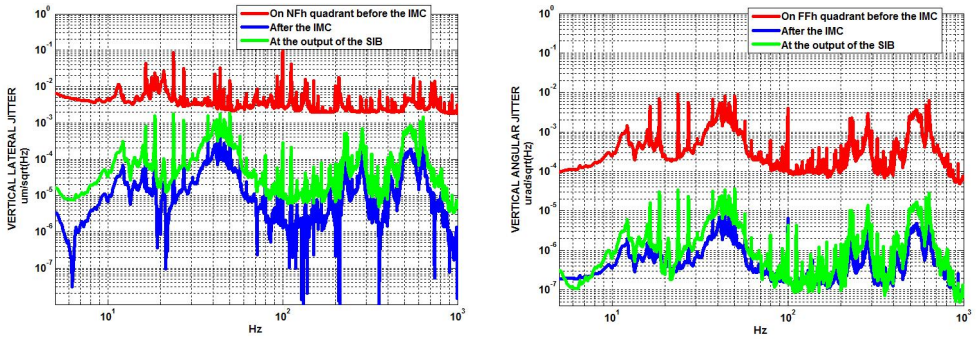

(a) (b)

Figure 3.13: *Vertical jitter at SIB output*

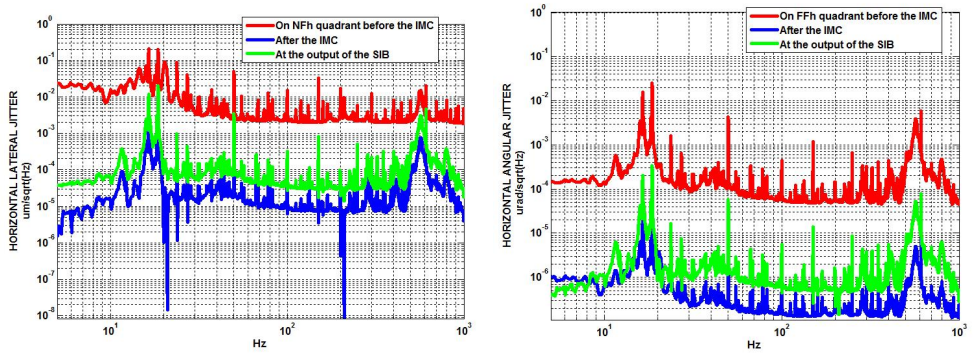

(a) (b)

Figure 3.14: *Horizontal jitter at SIB output*

Through the analysis made it is possible to estimate the jitter at the "SIB" bench output and therefore at the interferometer input, (see Fig. 3.13 and Fig. 3.14).

The curves obtained show as that around 40Hz, the angular and lateral motions of "EIB" bench limit the jitter at interferometer input to a value: $10^{-9}\ \frac{\mathrm{m}}{\sqrt{\mathrm{Hz}}}$ and $2 * 10^{-11}\ \frac{\mathrm{rad}}{\sqrt{\mathrm{Hz}}}$. How we will show, this value is a limit for Virgo interferometer just around 40Hz but for the second generation interferometer the jitter noise will be a limit also to the remaining frequencies.
So that the motions of "EIB" must be attenuated in order to meet the most stringent requirements of a second generation interferometer.

3.2 Calculation of the Dark Fringe Phase Noise induced by the Coupling between ITF Misalignments and Input Beam Jitter

In this section we present a calculation of the phase noise in a recycled interferometer with Fabry-Perot cavities in the arms, induced by the coupling of the fluctuations in position and in direction of the input laser with the misalignments of the interferometer mirrors.
The parameters of the interferometer used in the simulation are listed in table 3.3.

l_{cav}	l_1	l_2	l_{PR}	ROC_{ITM}	ROC_{ETM}	T_{ITM}	R_{ITM}	R_{ETM}	T_{PR}	R_{PR}
2999.9 m	5.634 m	6.513 m	6.000 m	∞	3450 m	0.007	0.883	0.99996	0.0513	0.9487

Table 3.3: *Parameters used in the simulation*

The optics misalignments of the interferometer are described by fixing the position of the recycling mirror and allowing the two Fabry-Perot cavities of the arms to move.

The little misalignments of the mirrors of FP cavities and the Finesse/losses asymmetries between the two arms transform the jitter in a certain amount of phase noise of the carrier at the level of the dark fringe.

Assuming that the vertical and horizontal degrees of freedom are uncoupled, we can restrict the analysis to one dimension.

The input field of the ITF will be:

$$E_{IN}(z_0) = E_0 \begin{pmatrix} \psi_0 \\ \frac{a_1}{2}\left(e^{i\omega_j t} + e^{-i\omega_j t}\right) \cdot \psi_1 \end{pmatrix} \exp(i\omega_0 t) \tag{3.12}$$

where a_1 is the amplitude of first order mode ψ_1, given by $a_1 = x_0 + i\alpha_0$, with:

$$x_0 = \frac{\tilde{x}_0}{w(z_0)}\left(1 + i\frac{z_0}{z_R}\right) \qquad\qquad \alpha_0 = \tilde{\alpha}_0 \frac{\pi w(z_0)}{\lambda} \tag{3.13}$$

An ITF mirror which is tilted by an angle Θ with respect to the ψ_0 mode is represented by the matrix:

$$M = \begin{pmatrix} \sqrt{1+\theta^2} & -2i\theta \\ -2i\theta & \sqrt{1+\theta^2} \end{pmatrix} \tag{3.14}$$

with $\theta = \frac{\pi w(z)}{\lambda}\Theta$.

A field reflected by a tilted mirror will be (adopting the notation 2 in appendix A):

$$E_r = rME_{IN} \tag{3.15}$$

Note that if the beam is reflected from the rear surface of the mirror, the reflection coefficient becomes rM^{-1} so that:

$$E_r = rM^{-1}E_{IN} \qquad\qquad \text{(rear surface)} \tag{3.16}$$

The above technique allows us to obtain a model for the characterization of the ITF sensitivity to the fluctuations in the input beam direction at frequency f and to the coupling of these with each static interferometer mirrors misalignments.

To provide a detailed analysis of the jitter effects on the dark fringe we will develop the formalism, discussed above, to various optical configurations:

- two mirrors resonator;
- Michelson interferometer with one cavity in each arm;
- previous configuration with an additional power recycling mirror between the laser and the beam splitter
- previous configuration with SR

3.2.1 *Two Mirrors Resonator*

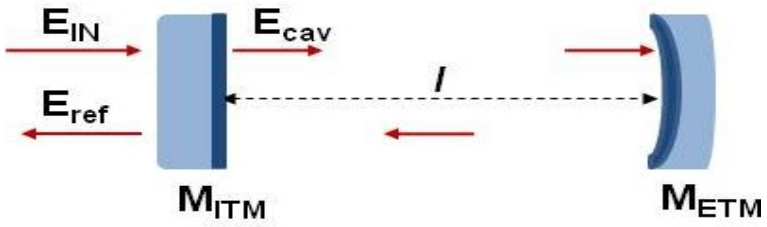

Figure 3.15: *Optical configuration of two mirrors resonator.*

Given the optical configuration in figure 3.15, we go to analyze as an input beam jitter behaves in reflection. To this purpose we take in account the transfer function of a mode ψ_1 into a mode ψ_0. The figure 3.15 defines the parameters (listed in the Table 3.3).
The round trip propagator inside the cavity is:

$$P_{cav} = r_{ITM} r_{ETM} M_{ITM} L M_{ETM} L \tag{3.17}$$

This propagator takes into account the mirrors misalignments through the M_i matrices given by Eq. 3.2. The L matrix is the free-space propagator:

$$L = \begin{pmatrix} \exp(i2\pi f \frac{l}{c}) & 0 \\ 0 & \exp(i2\pi f \frac{l}{c} + i\phi_C) \end{pmatrix} \tag{3.18}$$

L include the round trip phase shift and the Gouy phase ϕ_C:

$$\phi_C = 2\arctan\left(\frac{z_{TM}}{z_R}\right) = 2\arctan\left(\frac{l}{2z_R}\right) \tag{3.19}$$

The total field in the cavity is then the sum of all the contributions given by an infinite number of round trips of the field, and it is given by

$$E_{cav} = it_{ITM} E_{IN} \cdot \sum_{\infty}^{n=0} P_{cav}^n \tag{3.20}$$

Summing the series:

$$E_{cav} = it_{ITM} \left(U - P_{cav}\right)^{-1} \cdot E_{IN} \tag{3.21}$$

The reflected beam will be given by:

$$E_{ref} = r_{ITM} M_{ITM}^{-1} E_{IN} + it_{ITM} L M_{ETM} L E_{cav} =$$

$$= \left[r_{ITM} M_{ITM}^{-1} - t_{ITM}^2 L M_{ETM} L \left(U - P_{cav}\right)^{-1}\right] E_{IN} = R_C E_{IN} \tag{3.22}$$

R_C is a 2x2 matrix and its lower off-diagonal element represents the frequency dependent transfer function of a ψ_1 mode in the input field into the ψ_0 mode in the reflected field. The figure 3.16 shows the transfer functions of the jitter at $\pm f$ around the resonant fundamental mode for tilted end and tilted input mirrors in a cavity with parameters define in tab. 3.3.

In the case the end test mass is tilted small parts of the ψ_1 mode enter the cavity. The resonance of this field is stronger when the jitter frequency is still within the

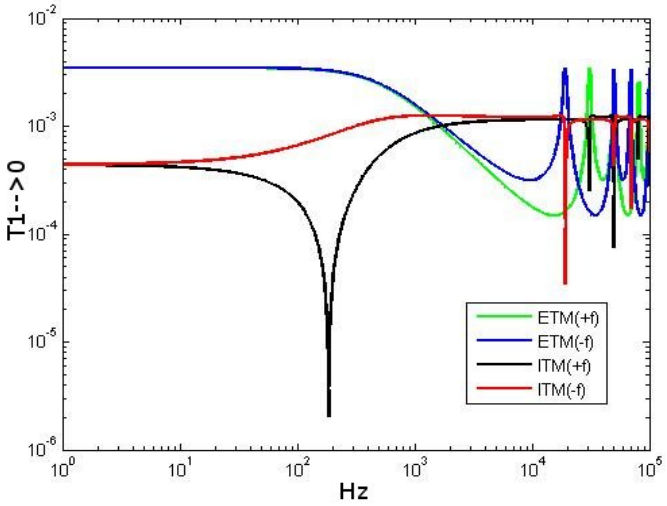

Figure 3.16: *Transfer function of mode ψ_1 in to a mode ψ_0 for two mirrors resonator.*

line width of the cavity $\left(f < FWHM/2 = \frac{FSR}{2F} \approx 5kHz\right)$. Above the line width the transfer function rolls off with the cavity pole. Jitter sidebands are also enhanced when the ψ_1 mode, the source mode, is resonant in the cavity. This is the case when the jitter frequency is equal to the transversal mode spacing of $f_t = \frac{FSR}{\pi} \arccos \sqrt{\left|1 - \frac{l_{cav}}{ROC_{ETM}}\right|} = 19.2kHz$.

In the case the input test mass is tilted, the ψ_1 mode generates a ψ_0 mode when it is directly reflected at the input mirror and also during its round trip through the cavity. The contribution inside the cavity picks up additional Gouy-phase in the cavity before it interferes with the directly reflected field. This creates the notch at 200Hz in the -f transfer function and the slight increase in the +f transfer function. Only the directly reflected field contributes at frequencies above the cavity pole.

3.2.2 *Michelson Interferometer with One Cavity in Each Arm*

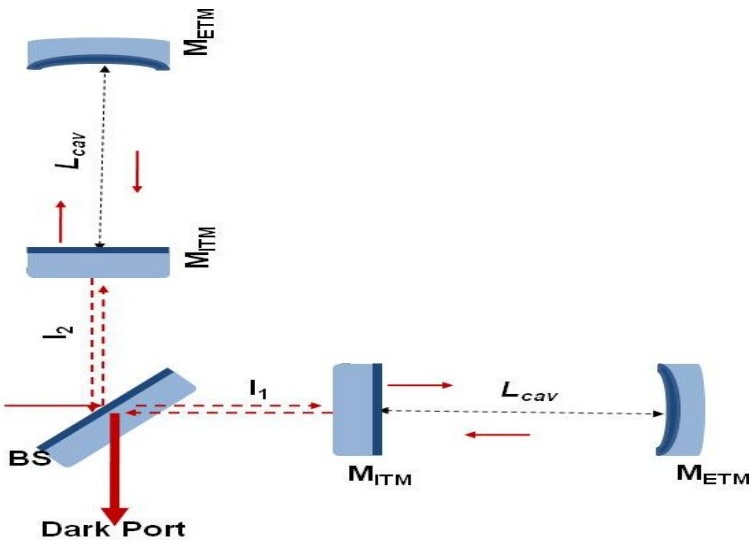

Figure 3.17: *Optical configuration of MI with one cavity in each arm.*

The field transmitted through a Michelson interferometer (MI) with one cavity in each arm to the dark port is a linear combination of the fields reflected at each cavity (Fig. 3.17):

$$E_{DP} = it_{bs}r_{bs}\left(L_1 R_{C1} L_1 + L_2 R_{C2} L_2\right) E_{IN} = T E_{IN} \tag{3.23}$$

R_{Ci} is the reflectivity of arm cavity i, respectively, as defined in Eq. 3.22.
L_i is the free space propagator which describes the propagation between the input test mass (ITMi)and the beam splitter:

$$L_i = \begin{pmatrix} \exp(i2\pi f \frac{l_i}{c}) & 0 \\ 0 & \exp(i2\pi f \frac{l_i}{c} + i\phi_i) \end{pmatrix} \tag{3.24}$$

Where l_i and ϕ_i are the distances and the Guoy phases between ITMi and the BS, respectively ($\phi_i = \arctan\frac{z_{BS}}{z_R} - \arctan\frac{z_{ITM}}{z_R}$).
The difference between the two distances (Schnupp asymmetry) is $l_2 - l_1 = 87.9cm = c/85.3MHz/4$. We analyze the situation for differential (subscript D) and common (subscript C) tilts of the ITMi and ETMi. A differential tilt is defined as $\Theta_D = \frac{\Theta_2 - \Theta_1}{2}$, while a common tilt is defined as $\Theta_C = \frac{\Theta_2 + \Theta_1}{2}$.
The transfer function of a mode ψ_1 into a mode ψ_0 measured at the dark port for common and differential ITM (left panel) and ETM (right panel) tilts for jitter sidebands around the carrier are shown in Fig. 3.18.
They are virtually identical to the cavity transfer functions except that:

1. In the -f transfer function for common tilts, the curve has a notch at 2.23 kHz. This is the case when $k(l_2 - l_1) = \frac{\phi_2 - \phi_1}{2}$.

2. the transfer function for common tilts are about three orders of magnitude smaller than for differential tilts. In fact, if the MI would be perfectly symmetric, the transfer function for common tilts would be identical to zero.

3. the ETM tilts are 1 order of magnitude greater than ITM tilts.

3.2.3 *Michelson Interferometer with One Cavity in Each Arm and a Power Recycling Mirror*

A Michelson interferometer with the power recycling (PR) mirror at the input, as shown in Fig. 3.19 forms a new cavity.
The reflectivity of the MI is:

$$R_{MI} = \left(r_{bs}^2 L_1 R_{C1} L_1 - t_{bs}^2 L_2 R_{C2} L_2\right) \tag{3.25}$$

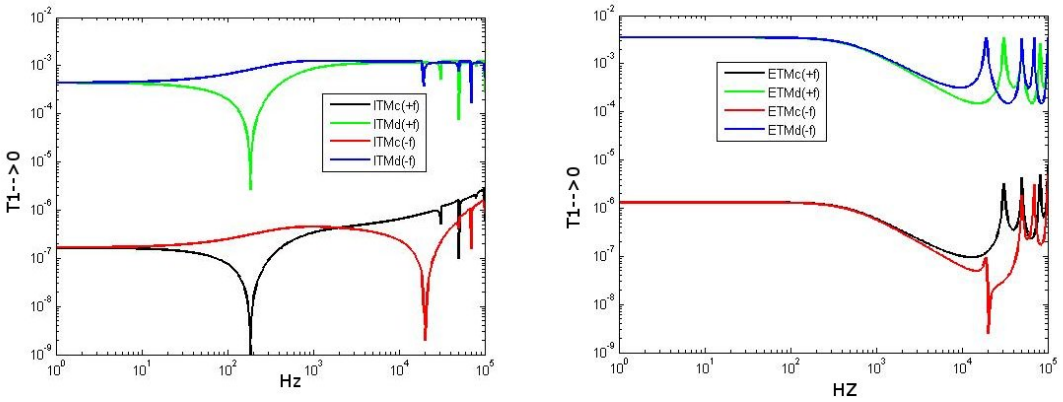

(a) (b)

Figure 3.18: *Transfer function of a mode ψ_1 in a mode ψ_0 for a Michelson interferometer with one cavity in each arm.*

The field reflected from the input mirror is then given by (as in Eq. 3.21)

$$E_{PR} = it_{PR}\left(U - P_{PR}\right)^{-1} E_{IN} = R_{PR}E_{IN} \tag{3.26}$$

Where P_{PR} can be calculated by replacing r_1M_1 and r_2M_2 in the equation 3.17 for the simple cavity with matrices $r_{PR}M_{PR}$ and R_{PR}:

$$P_{PR} = r_{PR}M_{PR}L_PR_{PR}L_P \tag{3.27}$$

r_{PR} is the amplitude reflectivity of the PR-mirror and M_{PR} is the tilt matrix for the PR mirror.

$L_P$is the free space propagator which depends on the distance l_P and the Gouy-phase ϕ_P between the PR-mirror and the beam splitter:

$$L_P = \begin{pmatrix} \exp(i2\pi f\frac{l_P}{c}) & 0 \\ 0 & \exp(i2\pi f\frac{l_P}{c} + i\phi_P) \end{pmatrix} \tag{3.28}$$

The field at the dark port is then:

$$E_{DP} = it_{PR}TL_P\left(U - P_{PR}\right)^{-1} E_{IN} \tag{3.29}$$

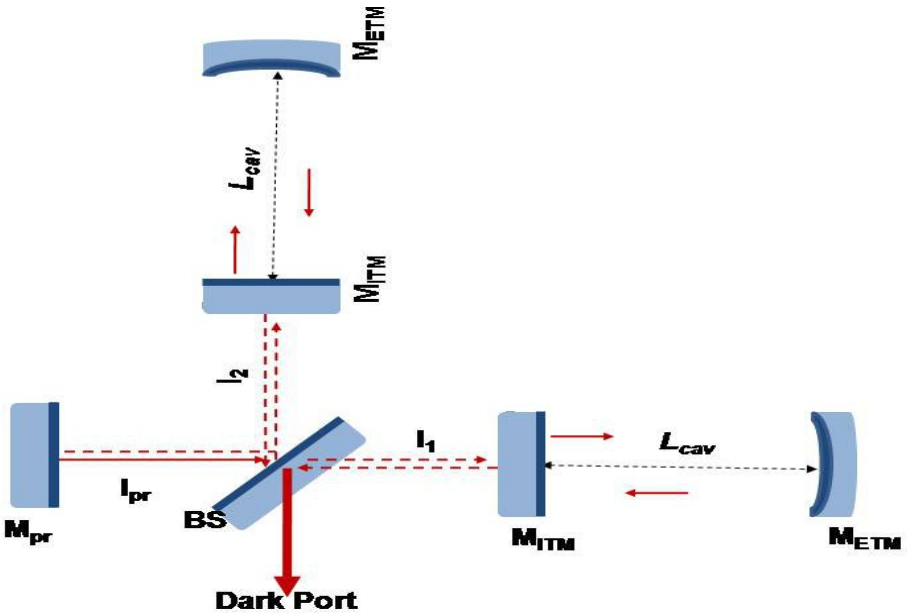

Figure 3.19: *Optical configuration of MI with one cavity in each arm and a power recycling mirror.*

where T is given by the Eq. 3.23.
The Transfer function of a mode ψ_1 into a mode ψ_0 at the dark port for this system for common and differential mirror tilts is shown in Fig. 3.20 while in Fig. 3.21 it is shown the Transfer function for the same system with Schnupp asymmetry, non-symmetric arm cavities. Asymmetries can be caused by:

- differences in the losses or transmissivities of the mirrors
- differential detuning ΔL caused by offsets in the L error signal. For example, DC sensing depends on asymmetries in the arm cavities to generate the correct local oscillator at the dark port

How we can observe, in the Virgo optical configuration the coupling between the input jitter and the spurious misaligned of the mirrors cavities is less than a simple

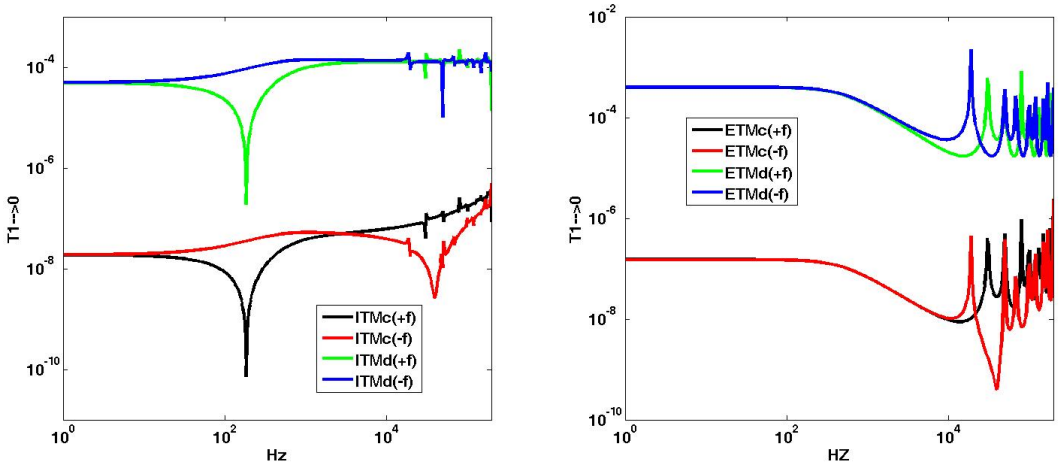

(a) (b)

Figure 3.20: *Transfer function of a mode ψ_1 in a mode ψ_0 for MI with one cavity in each arm and a power recycling mirror.*

Michelson configuration while the coupling is more relevant if we take into account the system asymmetry.

Moreover we can see the coupling Input jitter-ETM common tilt are negligible than the coupling Input jitter-ETM differential tilt but it can become important at low frequencies if we have cavities asymmetries or PR gain losses. In particular cases, the coupling Input jitter-ETM common tilt becomes the same amplitude than the coupling Input jitter-ETM differential(Fig. 3.22). In Fig.3.23 we note that the input jitter is coupling with the power recycling mirror tilt less than mirrors cavities tilts.

3.3 Cross Check of the Results

In this section we validate the analytical model obtained with the measurement done in Virgo. At the end we obtain the transfer function of the optical system (EIB +

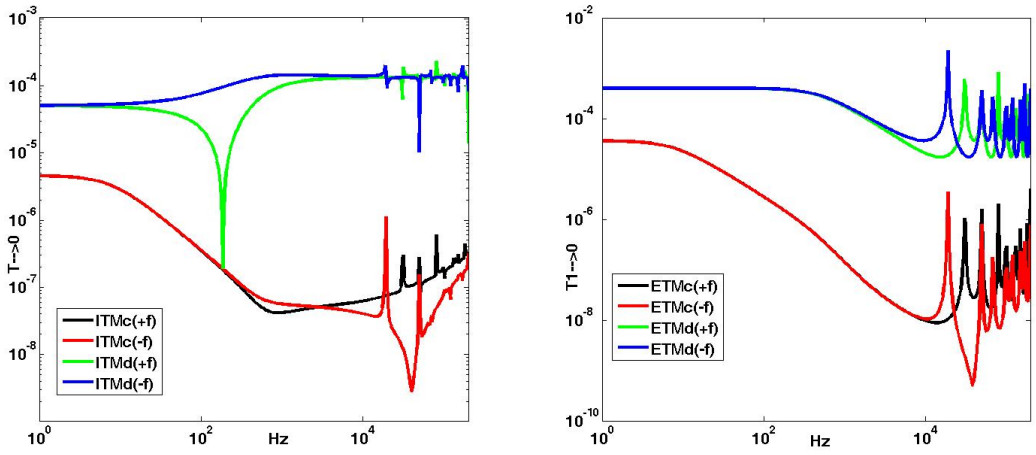

(a) (b)

Figure 3.21: *Transfer function of a mode ψ_1 in a mode ψ_0 for MI with one cavity in each arm and a power recycling mirror with Schnupp asymmetry and non-symmetric arm cavities.*

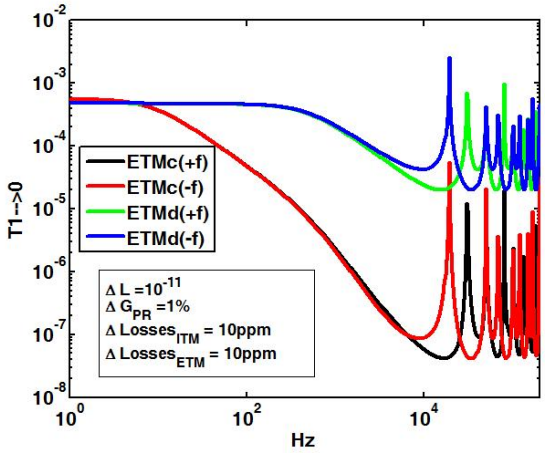

Figure 3.22: *Transfer function of a mode ψ_1 in a mode ψ_0 for MI with one cavity in each arm and a power recycling mirror with Schnupp asymmetry, non-symmetric arm cavities and Power Recycling Gain losses.*

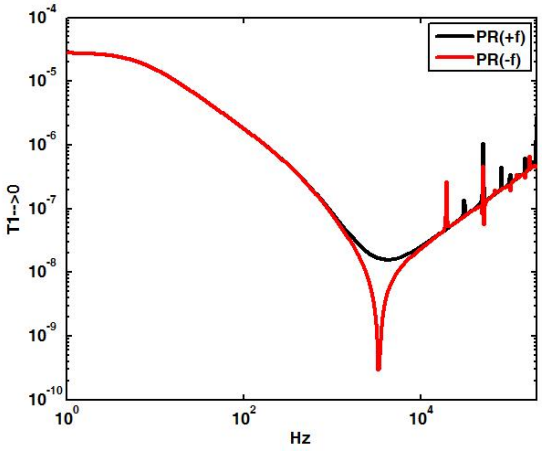

Figure 3.23: *Transfer function of a mode ψ_1 in a mode ψ_0 for MI with one cavity in each arm when the Power Recycling mirror is tilted.*

IMC + Telescope2 + Interferometer) so that we can reconstruct the dark fringe signal monitoring the motion of the optical injection elements of the interferometer. As stated in section 3.2, the input field of Interferometer (for one degree of freedom) is given by:

$$E_{IN}(z_{pr}) = E_0 \begin{pmatrix} \psi_0 \\ \frac{a_1}{2}\left(e^{i\omega_j t} + e^{-i\omega_j t}\right)\cdot\psi_1 \end{pmatrix} \exp(i\omega_0 t) \tag{3.30}$$

where a_1 is the amplitude of first order mode ψ_1, given by $a_1 = \frac{\tilde{x}_{pr}}{w(z_{pr})} + i\tilde{\alpha}_{pr}\frac{\pi w(z_{pr})}{\lambda}$, with $\tilde{x}_{pr}$ and $\tilde{\alpha}_{pr}$ beam misaligned given in section 3. The main Interferometer Transfer-Function will be given by 2x2 matrix T:

$$T_{DP} = \begin{pmatrix} A(\pm f) & B(\pm f) \\ C(\pm f) & D(\pm f) \end{pmatrix} \tag{3.31}$$

So that, the field at Dark Port will be:

$$E_{DP} = \begin{pmatrix} a_0^{DP}(\pm f)\cdot\psi_0 \\ a_1^{DP}(\pm f)\cdot\psi_1 \end{pmatrix} \exp(i\omega_0 t) = T\cdot E_{IN}(z_{pr}) \tag{3.32}$$

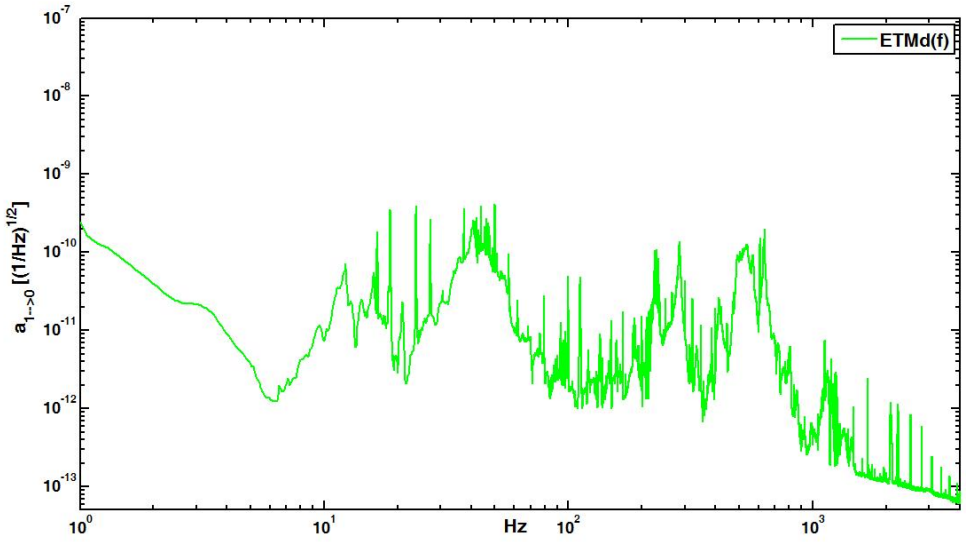

Figure 3.24: *Input Jitter Coupling with End Mirrors Cavities Tilt at DP.*

$$a_0^{DP}(\pm f) = E_0 \left(A(\pm f)\, a_0 + B(+f)\, \frac{a_1}{2} e^{i\omega t} + B(-f)\, \frac{a_1}{2} e^{-i\omega t} \right) \tag{3.33}$$

For DC sensing we can write:

$$|E_{DP}|^2_{DC} = P_0 \left(|A(\pm f)\, a_0|^2 + \left| B(+f)\, \frac{a_1}{2} \right|^2 + \left| B(-f)\, \frac{a_1}{2} \right|^2 \right) \tag{3.34}$$

In figure 3.24 we can observe how the input jitter measured at External Injection Bench by the BMS is coupling with the spurious misaligned caused by a differential tilt of end mirrors cavities, where $a_{1\to 0}^{DP} = \left| B(+f)\, \frac{a_1}{2} \right|$.

Therefore with a power input laser of 20W, the jitter sideband contribution to read out signal at Dark-Port photodiode will be (see Fig. 3.25): $\sqrt{P_0 \left(\left| B(+f)\, \frac{a_1}{2} \right|^2 + \left| B(-f)\, \frac{a_1}{2} \right|^2 \right)}$.

Now, we can evaluate if the effect of coupling between input jitter and mirrors interferometer misalignment decreases the detector signal to noise ratio.

In order to set the requirements for the misalignments the jitter noise can be compared with the expected noise of the interferometer.

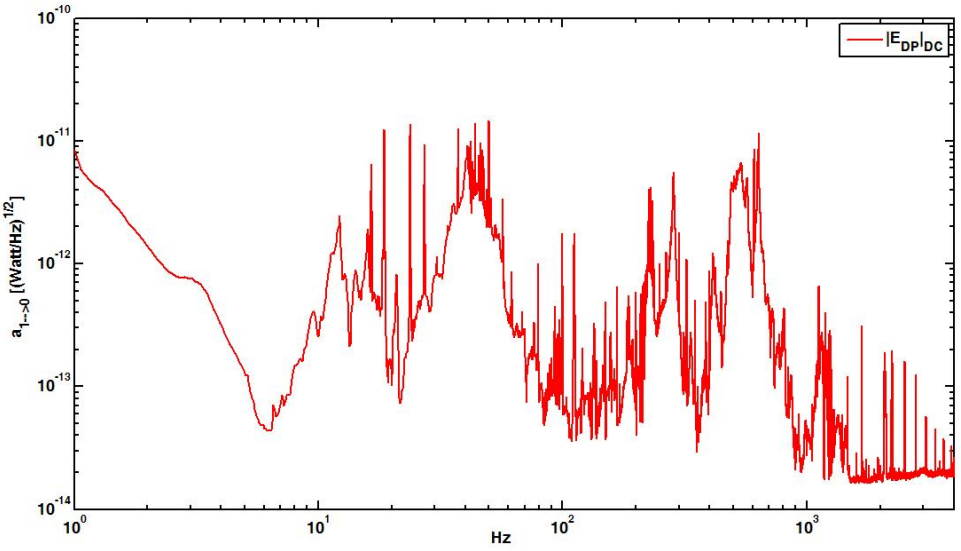

Figure 3.25: *Jitter sideband contribution to read out signal at Dark-Port photodiode with a Power laser of 20W.*

Based on this, use the approach suggested by Guido Mueller (in Ligo document T0900142_v2 [34]): it is taken the envelope of the sensitivity curves shown in [35] and it is assumed that the detector will be shot noise limited down to 40Hz in at least one of the configurations. Below 40Hz the sensitivity decreases then with f^{-2} due to radiation pressure noise. These assumptions lead to an envelope of the strain sensitivity of:

$$h_{envelope} = 3 \cdot 10^{-24} \sqrt{1 + \left(\frac{40Hz}{f}\right)^4} \frac{1}{\sqrt{Hz}} \tag{3.35}$$

although this number never enters the calculation.

Applying the same to Virgo, we go to use the envelope of the sensitivity curves shown in Fig. 3.26, obtaining an envelope of the strain sensitivity of:

$$h_{envelope} = 5 \cdot 10^{-23} \left[1 + \left(\frac{50Hz}{f}\right)^4\right]^{3/5} \frac{1}{\sqrt{Hz}} \tag{3.36}$$

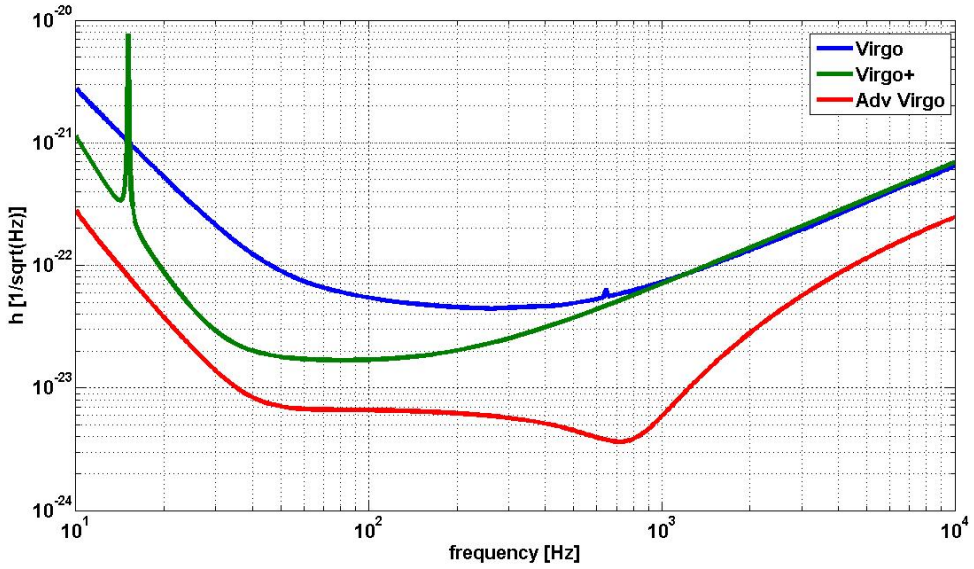

Figure 3.26: *Virgo, Virgo+ and Adv Virgo sensitivity curves.*

The requirements are then calculated the following way:

- Start with the number of photons in the input beam:

$$N_{in} = 0.5 \cdot 10^{20} \frac{1}{s} \text{ equivalent to } Pin = 10W \tag{3.37}$$

- Then, calculate the amplitude transfer-function for a 10-mode in the input field into the 00-mode at the dark port for a specific tilt of the core optics mirrors (for example differential ETM tilt).

$$a_{00}^{DP}(f) = T_{10\to00} a_{10}^{in}(f) \tag{3.38}$$

f is the Fourier frequency of the beam jitter and includes positive and negative components; $a_{10}^{in}(f)$ is the relative amplitude of the 10-mode in the input field. So $\sqrt{N_{in}} a_{10}^{in}(f)$ is the amplitude of the 10-mode in units of $\sqrt{\text{number of photons}/s}$. The amplitude of the created 00-mode in the dark port is then:

$$a^{DP}\sqrt{N_{in}} = T_{10\to00} a_{10}^{in}(f)\sqrt{N_{in}} \tag{3.39}$$

This relative amplitude of the 10-mode (relative to the 00-mode amplitude in the input field) can now be calculated by setting this to be smaller than unity for frequencies where we are shot noise limited and allow for a roll up at lower frequencies with f^{-2}. It is taken in account a safety factor of 20, factor 2 for the two directions and factor of 10 for technical noise,this gives:

$$a_{10}^{in}(f) \leq 0.05 \cdot \frac{\left[1 + \left(\frac{50Hz}{f}\right)^4\right]^{3/5}}{\sqrt{N_{in}} T_{10\to 00}} \tag{3.40}$$

So at 10 Hz $a_{10}^{in}(f) \leq 10^{-7} \frac{1}{\sqrt{Hz}}$ while at 100 Hz $a_{10}^{in}(f) \leq 3\ 10^{-9} \frac{1}{\sqrt{Hz}}$.
At interferometer input, the waist is ≈ 2 cm so that, around 40Hz we can estimate that a maximum shift must be less then $10^{-10}\ \frac{\mathrm{m}}{\sqrt{\mathrm{Hz}}}$ and the maximum tilt must be less then $10^{-13}\ \frac{\mathrm{rad}}{\sqrt{\mathrm{Hz}}}$ that compared with the results of the figure 3.13 we can conclude that in the case of Virgo typically the jitter effects are below the design curve but already at 40 Hz we have estimated a jitter of about $10^{-9}\ \frac{\mathrm{m}}{\sqrt{\mathrm{Hz}}}$ and $2\ 10^{-11}\ \frac{\mathrm{rad}}{\sqrt{\mathrm{Hz}}}$.
So that, we can say the contribution of EIB angular and lateral motion at dark port is not negligible around 40Hz.
Using the same logic to Virgo+ where the input power is 50W, we get the more stringent conditions, so that we can conclude that in this case we already have problems of non-negligible jitter in a frequency range greater then Virgo.

3.4 The Importance of Jitter in Advanced Virgo

At this point we have obtained a transfer function of the optical system that allows us to evaluate the effects on the dark fringe of the input beam jitter in Virgo and we have validated our model.
What has been obtained is now applied to Adv Virgo, making the appropriate changes.

In Ad-Virgo the sensitivity will be a factor 10 better than Virgo, it is very likely that the beam jitter noise for Adv Virgo won't be negligible if the injection system is not improved. So, using the analytic model obtained, we will be able to set an upper bound for the beam jitter noise at the input of the Adv Virgo, thus we will provide some requirements to various subsystems of Adv Virgo.

The expected displacement sensitivity of Advanced VIRGO is shown in Fig.3.27

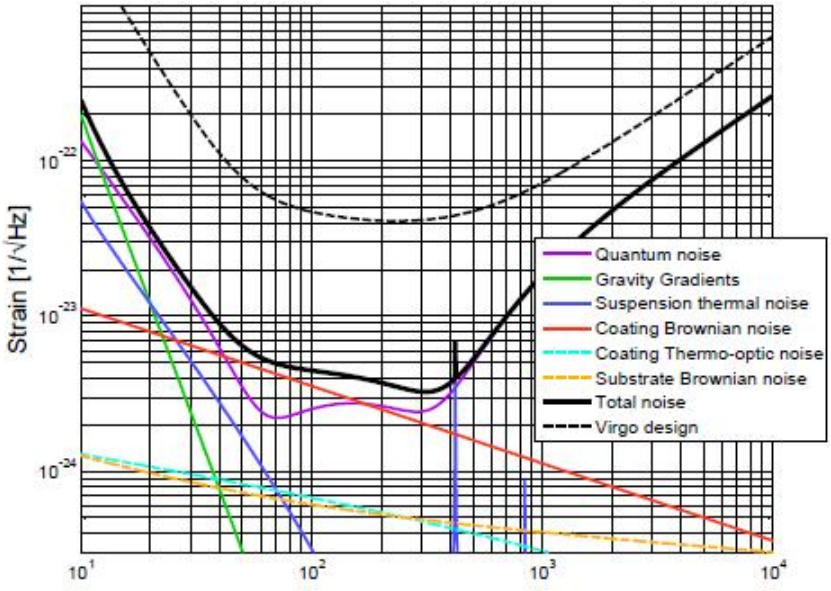

Figure 3.27: *Reference Adv Virgo sensitivity and expected noise contributions. The Virgo design sensitivity is shown for the sake of comparison.*

for input power Pin = 125W. At low frequencies the detector will be limited by radiation pressure noise, one component of the unified quantum noise. In the medium frequency range internal thermal noise of the mirror substrates will limit our sensitivity. Finally, shot noise, the second component of the unified quantum noise, will limit the sensitivity at high frequencies.

Contributions from technical noise sources like beam jitter have to be at least one

order of magnitude smaller than the contributions from these fundamental noise sources. So the jitter noise contribution at DP must be less then the black curve in Fig.3.27.

Applying the same processing used for Virgo configuration, for Adv Virgo parameter, we obtain at Dark Port a transmission function of first-order mode in zero-order mode given by the Fig. 3.28. Taking in account the envelope of the sensitivity

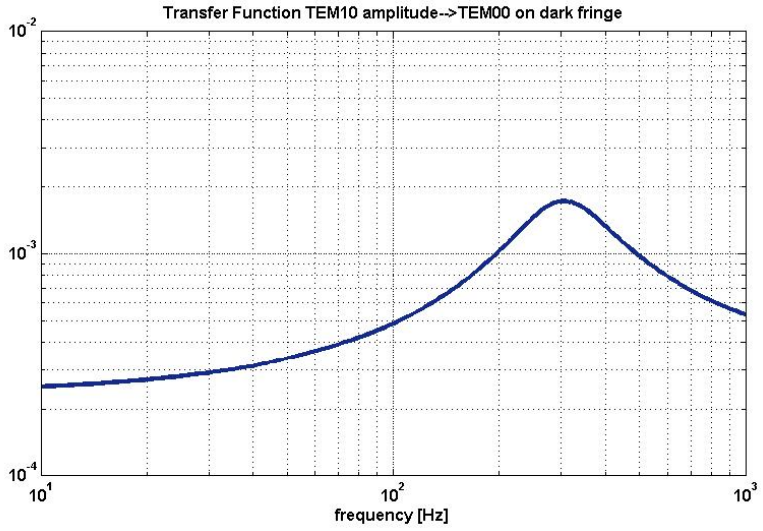

Figure 3.28: *Transfer function of mode ψ_1 in to a mode ψ_0 for Adv Virgo configuration.*

curves shown in Fig. 3.26, we obtain an envelope of the strain sensitivity of:

$$h_{envelope} = 6 \cdot 10^{-24} \left[1 + \left(\frac{40Hz}{f} \right)^4 \right]^{1/2} \frac{1}{\sqrt{Hz}} \tag{3.41}$$

Furthermore for a input power of $Pin = \ 125\ W$ we have:

$$N_{in} = 6.3 \cdot 10^{20}\ \frac{1}{s}$$

$$a_{10}^{in}(10\ Hz) \leq \ 10^{-7}\sqrt{1/Hz} \tag{3.42}$$

$$a_{10}^{in}(100\ Hz) \leq 4\ 10^{-9}\sqrt{1/Hz} \tag{3.43}$$

More generally, the complex amplitude of misalignment modes can be written as (in one freedom-degree):

$$\left|a_{10}^{in}(f)\right| = \sqrt{\left|\frac{\tilde{y}}{\omega_{pr}}\left(1 + i\frac{z_0}{z_R}\right)\right|^2 + \left|\tilde{\beta}\frac{\pi\omega_{pr}}{\lambda}\right|^2} \tag{3.44}$$

where $\tilde{y}$ and $\tilde{\beta}$ are the lateral and angular jitter at power recycling mirror (so at input of interferometer),ω_{pr}, the beam waist, λ, the laser wavelength, z_0, the distance from the waist and z_R, the Rayleigh range.

In Adv Virgo, $z_R = 190\ m$ and we considered $z_0 = 1500\ m$ and $w_{pr} = w(z_0) = 59mm$. So that, we can write:

$$\left|a_{10}^{in}(f)\right| = \sqrt{17.6\ 10^3\tilde{y}^2 + 3.4\ 10^{10}\tilde{\beta}^2} \leq \begin{cases} 10^{-7}\sqrt{1/Hz} & \text{at 10 Hz} \\ 4\ 10^{-9}\sqrt{1/Hz} & \text{at 100 Hz} \end{cases} \tag{3.45}$$

Jitter specs at the Michelson input obtained are:

- at 10 Hz $|a_{10}^{in}(f)| \leq\ 10^{-7}\ \frac{1}{\sqrt{Hz}} \Rightarrow \begin{array}{l} \tilde{y} \leq 7\ 10^{-10}\ \frac{m}{\sqrt{Hz}} \\ \tilde{\theta} \leq 5\ 10^{-13}\ \frac{rad}{\sqrt{Hz}} \end{array}$
- at 100 Hz $|a_{10}^{in}(f)| \leq 4\ 10^{-9}\ \frac{1}{\sqrt{Hz}} \Rightarrow \begin{array}{l} \tilde{y} \leq 3\ 10^{-11}\ \frac{m}{\sqrt{Hz}} \\ \tilde{\theta} \leq 2\ 10^{-14}\ \frac{rad}{\sqrt{Hz}} \end{array}$

The contribution of EIB angular and lateral motion should be seen by the ITF as beam jitter so that at least the same requirements than beam jitter should be asked for the bench residual motion. For Adv Virgo it has been necessary think of an improvement of EIB seismic isolation system. With an EIB suspended the amplitude of jitter at interferometer input will reduce by 1 or 2 factors around 10Hz and the peak around 40Hz will be flattened; this will make Adv Virgo sensitivity not limited by the jitter.

Actually the NIKHEF of Amsterdam works in progress to the suspension of EIB.

Chapter 4

High power laser and thermal effects in the injection system for Advanced Virgo

As mentioned in previous chapters, the injection system of VIRGO, in the currently configuration, is based on a 25W ultra-stable laser at 1064nm.
In order to improve the sensitivity of the interferometer, which is linked at high frequency to photon noise, it is planned to increase the laser power to 125W (project Advanced VIRGO).
The experience acquired during Virgo and Virgo+ commissioning showed that a such high input power will cause thermal distortions in optical components and change the mode quality of the optical beam.
Especially at this power, it will be necessary to take into account the thermal effects inside the IMC cavity, the suspended bench Faraday isolator and some various elements on the external injection bench.
In order to cancel out theses unwanted thermal effects it is necessary to control

them. This can be achieved by using different beam monitoring associated with active or passive compensation systems.
For example, we will see that the use of a compensation plate of DKDP can be a good way to compensate a thermal lens induced in a BK7 substrate. But a disadvantage is there is no possibility of fine tuning in this system and we couldn't have a local correction of the wavefront. So, it was been necessary to take in account a wavefront local control.
This was been the main experimental work during the my PhD.
A dynamically compensation technique has been proposed, in particular, to meet the requirements in Adv Virgo, a deformable mirror obtained using resistors as thermal actuators.
For this purpose we go to characterize the thermally deformable mirror in order validate the the possibility of using it in an adaptive optics system.

4.1 Thermal Lensing Effect

The largest thermo-optic effects, appearing in the VIRGO interferometer are tilt, focusing and astigmatism. Experience have already shown that the main parts of the injection system subject to thermal effects are the IMC cavity, the suspended bench Faraday isolator and some various elements on the external injection bench (Fig. 4.1). In Virgo it is necessity to compensate these effects, particularly in the Faraday isolator placed under vacuum. This element is placed between the IMC and the ITF and it used in VIRGO to isolate IMC from power reflected from the ITF. The Virgo group has studied how a Faraday isolator exhibits very high thermal lensing and so, they propose a passive method correction of this thermal effect.

The thermal lensing is a direct consequence of optical absorption inside its

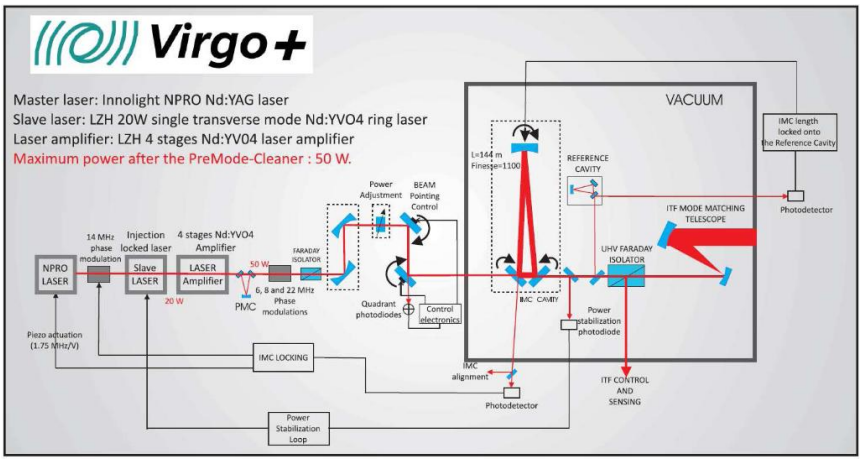

Figure 4.1: *Laser and injection system scheme.*

magneto-optical elements (TGG crystal). When the high power laser beam passes through the TGG, the center of the optics is heated and this heat is passed by conduction to the surfaces where it escapes by radiation.

The main consequence of this event is the appearance of a temperature gradient in the crystal.

The temperature gradient depends directly on the absorption level, the density of the incident power and is inversely proportional to the substrate thermal conductivity.

$$\Delta T(r) = \frac{\alpha_{sub} P}{4\pi k_{th}} \sum_{1}^{\infty} \frac{(-2)^n \cdot \left(\frac{r}{\omega}\right)^{2n}}{nn!} \tag{4.1}$$

Where $\Delta T(r)$ is the temperature difference between the center of the optic and a point at a distance r from the center, α_{sub} is the coefficient of absorption, P is the incident power and k_{th} is the substrate thermal conductivity.

In the presence of a temperature gradient in the substrate, the transmissive optics will behave like a lens.

This is a consequence of the thermo-optic effect: the refractive index is temperature dependent. Inside the optics, the temperature gradient induces a refractive index gradient.

The local refractive index changes with temperature T, so that the optical path change over the path S through a heated optic is:

$$\Delta S = \frac{dn}{dT}_S \Delta T \; ds \tag{4.2}$$

where $\frac{dn}{dT}$ is the thermo-optic coefficient.

Fig. 4.2 gives the results of precedent tests for a laser power going from 10 to 125 W for two different TGG crystal rods. The induced lens creates wavefront

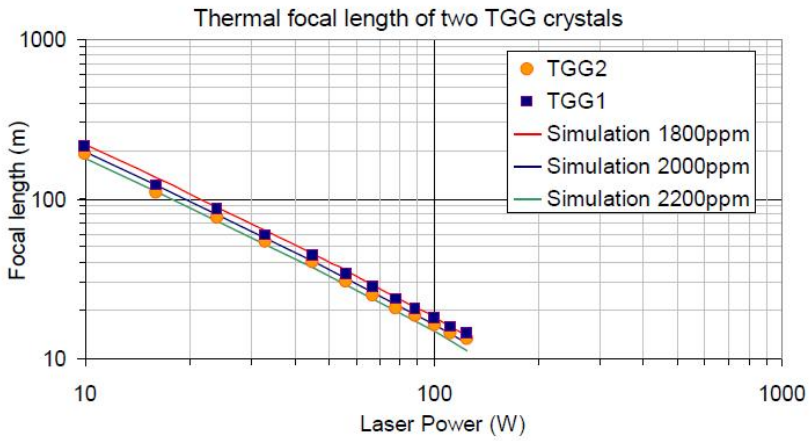

Figure 4.2: *Thermally induced lensing in TGG. Triangles and circles are experimental results. Lines correspond to results obtained with the finite element model code.*

distortion, accordingly a mismatching on the interferometer cavities and therefore a loss of coupled power (Fig. 4.3).

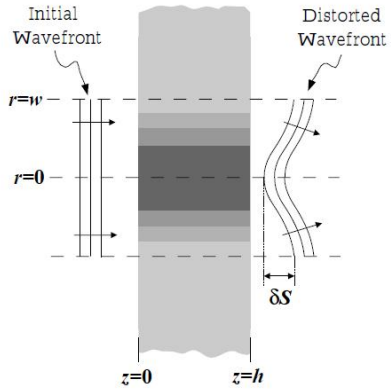

Figure 4.3: *Wavefront distortion caused by mirror heating.*

4.2 Thermal Lensing Effect Compensation

There are a few methods for compensating the effect of thermal lensing. They could be separated into two categories, passive methods and active methods. In this section we describe briefly the passive methods expected in Adv Virgo and we go to introduce the Phd work on an active method to wavefront control.

4.2.1 *Passive methods*

As we have seen in the measurements of Fig. 4.2, in Adv Virgo will be necessary to reduce this effect. One possibility proposed in Adv Virgo injection design is to include in the rotator an element realizing a passive compensation of these geometrical distortions.

For example it is possible to include a crystal of DKDP which exhibits a large negative thermo-optic coefficient ($\frac{dn}{dT}_{DKDP} = -4.4\ 10^{-5}\ K^{-1}$ to compare with $\frac{dn}{dT}_{TGG} = 1.9\ 10^{-5} K^{-1}$).

On Figure 4.4, we can see results obtained of negative thermal lensing created in a 4mm thick plate bought from Leysop Ldt (UK). With a simulation tool it is derived an absorption of this plate of about 800ppm.

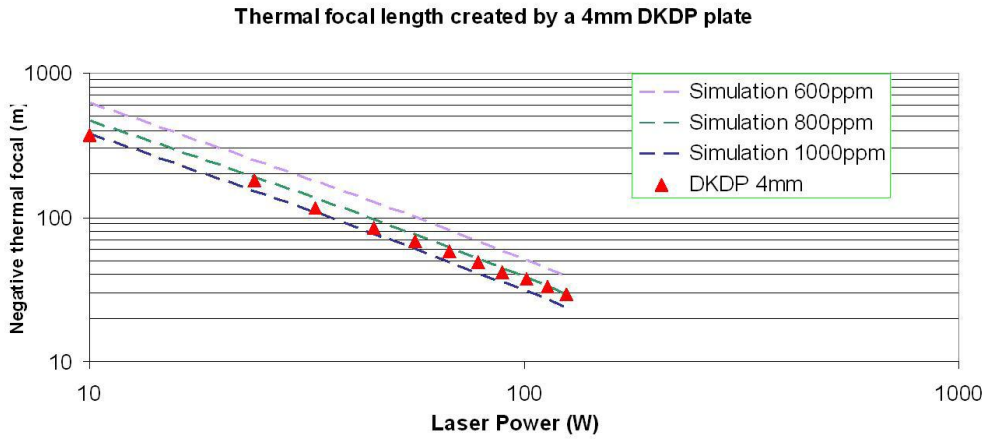

Figure 4.4: *Thermal focal length created by a 4mm DKDP. Simulations agree for an absorption of 800ppm.*

It was also possible to compute the length of DKDP necessary to correct for the TGG distortions and the result is given in Fig. 4.5, we got a good superposition for a 3.4 mm length DKDP rod in this case. Passive compensation has the advantage of being a very simple and efficient setup. However the exact combination of thickness and absorption must be chosen to have an ideal compensation. Afterwards there are no means to fine tune. In order to get some fine tuning we also studied different active methods so, in addition the system could not be used to correct for astigmatism. A passive compensation would therefore not be suitable for compensating effects for example in the IMC.

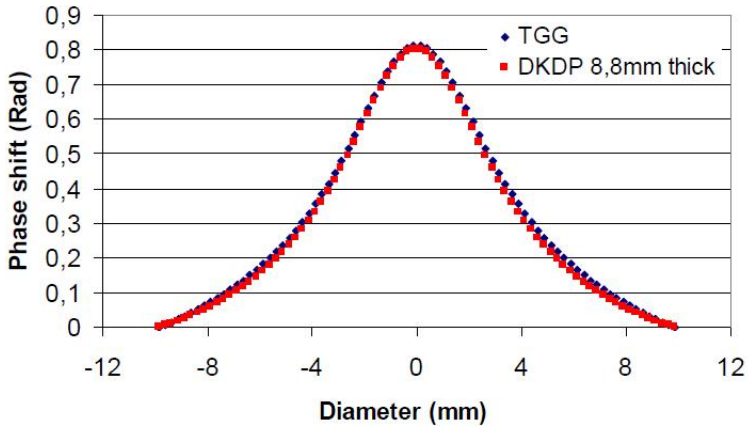

Figure 4.5: *Passive compensation for a Faraday isolator crossed by 40 watt power laser beam (an example).*

4.2.2 *Active methods*

For the passive compensation it is the transmitted beam that is absorbed by the compensation plate creating the compensating lens. For the active compensation the compensation plate is actively heated or cooled by an external device in such a way as to create the desired compensation.

So in addition to the passive control thermal effect, we proposed an active control; it will work as a controllable lens. The temperature gradient is achieved by using a heating element situated around the compensation plate (see Fig. 4.6).
The advantage of this type of compensation is the possibility to compensate for astigmatism or other higher order aberrations by changing the distribution of heating (and/or the orientation of the plate). The disadvantage of this technique is the low active of correction for considerable heating (up to 100 degrees).

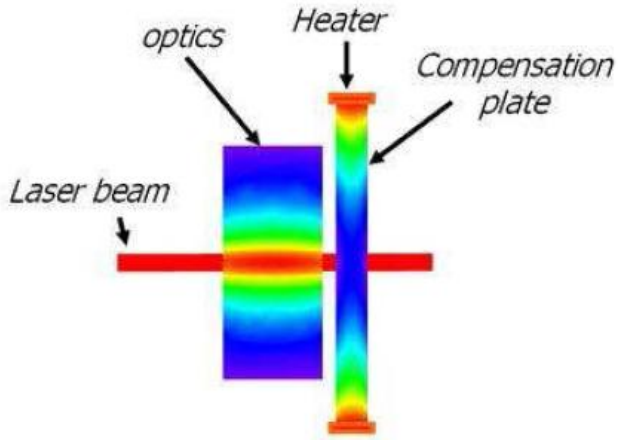

Figure 4.6: *Thermal lensing correction principle by the use of a compensation plate.*

Requirements

Using a deformable mirror could be the better and easier solution but we have to take into account some constraints: the system must be placed under vacuum and, as these systems should be placed after the IMC, it should be very stable (in order to not introduce beam jitter).

Furthermore, the device, to be compatible with the Adv-Virgo requirements, must be very high quality mirror and sustain high power laser.

In order to have high dynamic range, the thermal effects should be applied as close as possible to the beam. One possible technique could be to use a CO2 laser beam heating a transmissive substrate (Fused Silica for example) but the CO2 is very complex to use and potentially noisy.

To account for these problems, we propose to use an original method consisting of using an High Reflection Mirror that can distort the wavefront of a beam reflected from it by using thermal actuators.

thermally Deformable Mirror to perform a wavefront beam controller

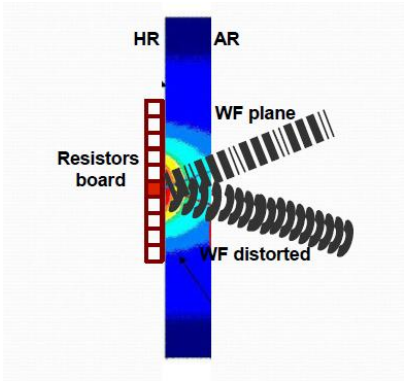

Figure 4.7: *Principle of the correction actuation of the TDM.*

This new deformable mirror proposed (see Fig. 4.7) is what we call TDM and in detail it is made with a a high reflective face and with an anti reflective coating on the front surface in order to use the mirror in a reverse way, thus allowing the beam to pass through the mirror substrate. The high reflective surface is heated by conduction with a micro-heater array.

Each heating element on the micro-heater array can be controlled separately. This heating therefore creates a non-homogeneous temperature distribution in the glass of the mirror so that the wavefront of light passing through the glass is modified according to the type of heating pattern applied.

In the next chapter we go to describe in detail the TDM design and TDM characterization.

Chapter 5

Wavefront Active Compensation: Characterization of a deformable mirror driven by micro-heater array

In this section we propose and characterize a new deformable mirror obtained with a micro resistors array as possible actuators.
Just as it is designed, it is called Thermally Deformable Mirror (TDM).
Moreover, let us notice that the TDM could have many scientific, industrial and medical applications as an alternative technology for low-cost active optics.
Especially, as mentioned in the previous chapter, in second generation of gravitational wave interferometer,the use of high power laser (200W for project Advanced VIRGO) and the non zero absorption coefficient of the optics (Faraday isolators, the electro-optic modulators and the mirrors in the cavities) causes a local heating and consequently a wavefront geometric deformation of the reflected and transmitted beams.
As already said in previous chapter, the variation of temperature causes a variation

of the refractive index of the material which produces thermal lensing effects.
It was necessary to perform an active system to controller and correct the wavefront distortions and that takes in account the AdV-Virgo requirements: compatible with the vacuum, very stable, very high quality mirror and sustain high power laser.

5.1 TDM to Perform a Wavefront Beam Controller

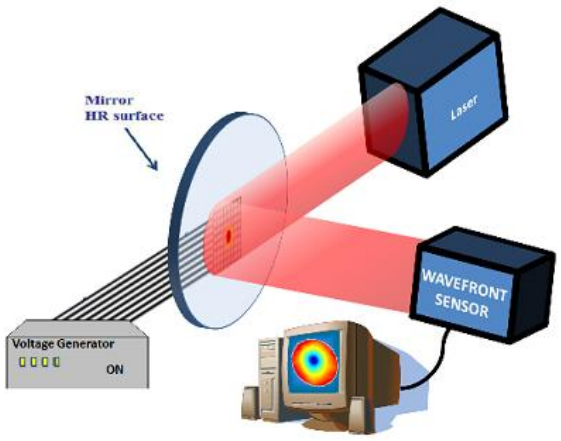

Figure 5.1: *Micro-heater-array scheme to perform a wavefront beam controller*

The TDM is a deformable mirror with an heater array how possible actuators to perform an active compensation system in order to cancel out the wavefront distortion generated by the thermal effects in the optical injection system.
Fig. 5.1 shows the schematic arrangement of the thermally deformable mirror. It consists of a mirror with Anti Reflection (AR) front surface coating and High Reflection (HR) coated (at 1064 nm) on the back face of the substrate. A micro-heater resistor array is in contact with HR surface of mirror with thermal grease. Using different powers (few milli-Watts) on each resistor, the mirror is heated point

by point in order to correct the locally wavefront deformation of the beam reflected by the mirror.
The system uses the heater array in contact with HR coating allowing efficient (in terms of power) correction of low and medium order terms (up to second order in Hermite-Gauss modes).
The measurements to the System-Characterization were performed in two different periods. In the first one, using an experimental set-up, we have investigated how the mirror transmission changes with the temperature and if these variations can be a limit to the use of thermally deformable mirror (TDM). In the second period, by using another set-up, the TDM system (mirror + heater array) is characterized.

5.2 Preliminary Test to verify no-transmission losses to mirror heating

Before proceeding with the measures for the characterization of the efficiency of TDM, we felt the need to check if mirrors with HR change their transmittivity factor when they were put in contact with a heating system. In the event that the transmittivity change means that a beam of light reflected from a mirror would TDM losses in power and what would be a limit to the use of an heater array how actuator for a deformable mirror.
So, we have investigated how the transmitted power changes with the temperature and if these variations can be a limit to the use of TDM. The mirrors tested are been:

- Mirror1: LAMBDA HHR-2506B-1064-45S
- Mirror2: CVI Melles Griot Y1-LW-3-1037-45-S

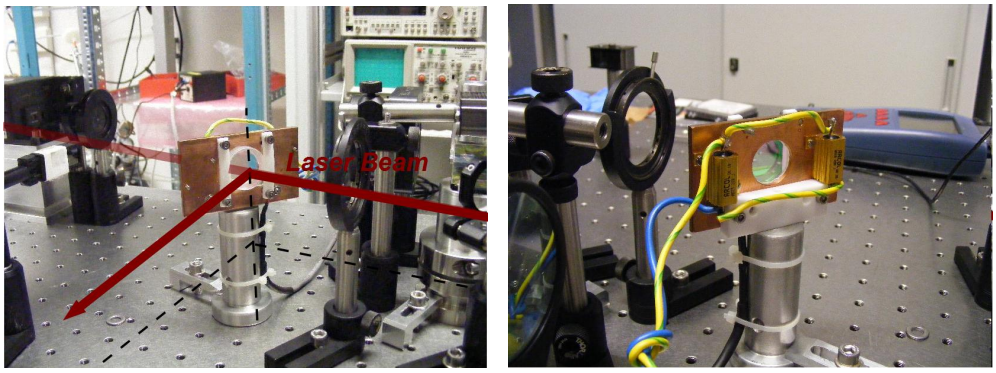

(a) (b)

Figure 5.2: *Test mirror mounted on a optical bench with the heating system installed, front (a) and rear view (b)*

These mirrors are 2 inches diameter BK7 substrate and are designed to reflect at high efficiency with no scattering or absorption. The setup can be seen in Fig. 5.2(a) where the tested mirrors are mounted to have a incidence angle of 45°.

A Heating System is used to heat the mirror, it is in contact with the anti-refection coating and fixed with thermal stick (Fig. 5.2(b)).

About the heating system, we used two hot resistances (R=11ohms) placed on a copper element for having the best conductive transfer of heating (Fig. 5.2(b)).

We have regulated the current arriving in the heating system with a Temperature Controller (Thorlabs "TC200"). The power transmitted was measured with a Power Meter (growing and decreasing the coating temperature) and the mirror temperature with an IR Camera.

We have been observed (Fig. 5.3) that the variations of the mirror Transmission vs temperature is a few ppm, so that we can conclude that these variations doesn't limit TDM and we can go on with the measurements to characterize the deformable mirror in question.

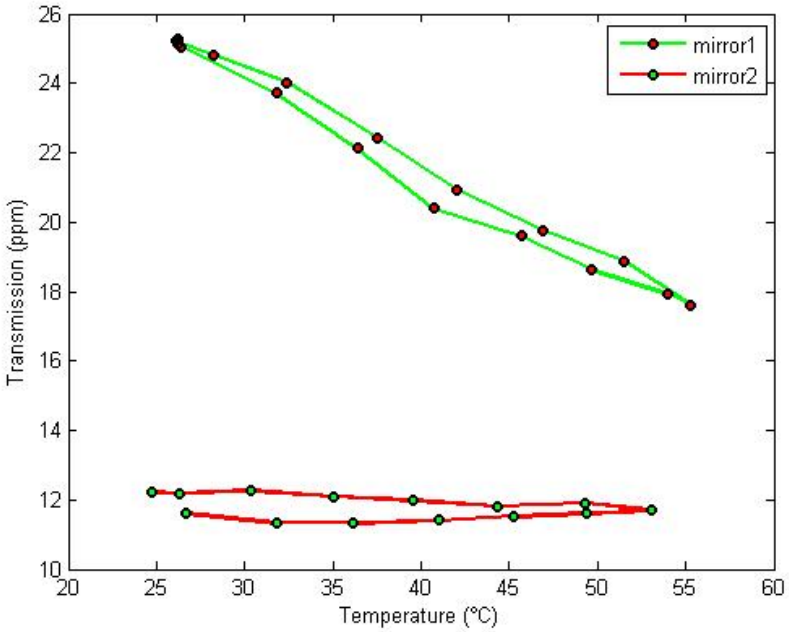

Figure 5.3: *Variations Transmission vs temperature of the tow mirrors: LAMBDA HHR-2506B-1064-45S and CVI Melles Griot Y1-LW-3-1037-45-S. The change is a few ppm so changes you may be considered it negligible.*

5.3 TDM Design

In this section, we go to investigate in more detail the TDM design.
A micro-heater is used to make a deformable mirror with "thermal actuators". The figure 5.4 below shows the principal of this technique.

The back of a mirror is heated with a micro-heater array for which each heating element can be controlled separately. This heating creates a non-homogeneous temperature distribution in the glass of the mirror. As both the refractive index and glass thickness depend on temperature, the wavefront of light passing through the glass is modified according to the type of heating pattern applied. In the case of

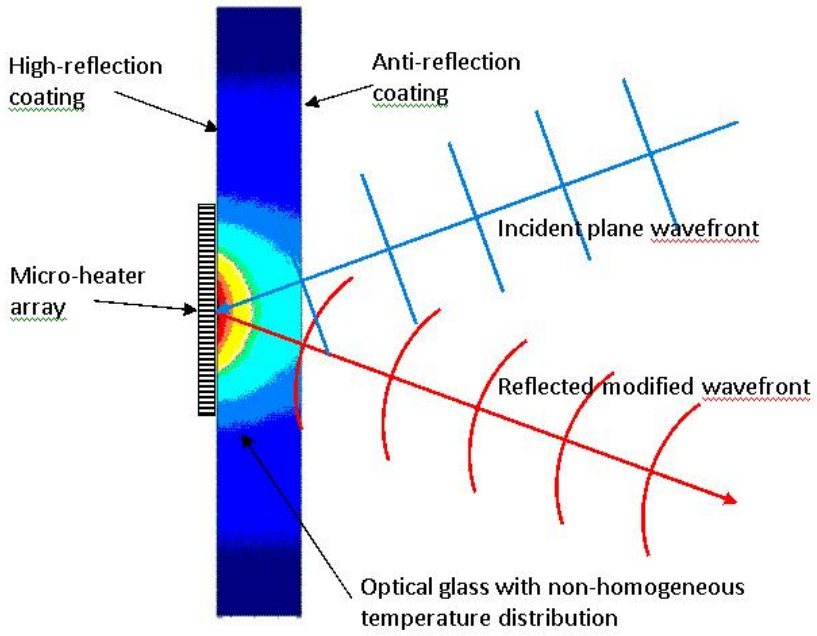

Figure 5.4: *Schematic setup of deformable mirror*

figure 5.4 the heating pattern applied has a gaussian distribution and made a flat wavefront become curved.

The Figure 5.5(a) below shows the configuration of the heating array.
There are 61 heating elements. The center to center spacing of each element is 1mm. The heating array is best mounted on a flexible substrate which allowed an optimal contact when surface mounted resistive elements was glued in contact with the optical surface of the mirror (HR face of the mirror)(see Fig. 5.6).
Therefore, there must be nothing protruding on this side of the board which could prevent a good contact.
The resistive elements are heated with a voltage source (one for each element). The maximum voltage is been 10 V. The ideal resistance for the available power source

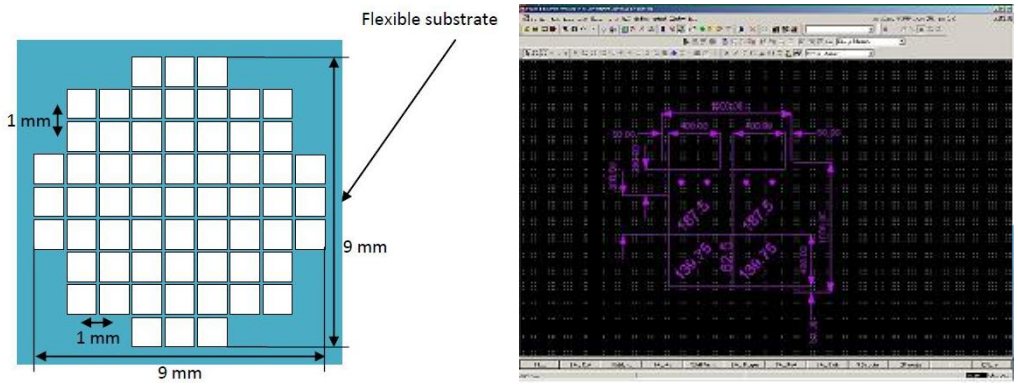

(a) (b)

Figure 5.5: *Schematic diagram of heating array configuration (a) and an example of a resistance design (b)*

is been 1000 Ohms. This results in a maximum power dissipation of 100mW.

How we seen in previous section, all the materials close to the heating array should be capable of working continuously at high temperature.

Figure 5.5(b) gives an example of a resistance design giving almost 700 Ohms (Note: Grid shown is $25\mu m$). The values shown in each quadrant are the calculated resistive values using Ohmega-Ply 250 ohm/square material. $(250 * 0.559 = 139.75\ ohms)$ $(250 * 0.75 = 187.50\ ohms)$ $(250 * 0.25 = 62.50\ ohms)$ $(187.5 * 2) + (139.75 * 2) + 62.5 = 717\ ohms$.

All connecting copper tracks are as small as possible in order to minimize heat conducting away from the heating elements.

The heating array is connected to a flexible cable of about 300 mm (see figure 5.6). The contacts at the end of this flexible cable is such that we can connect it to a home-built interface board and use a digital DAQ system to send the driving voltages to the heater array in Remote Control.

The Fig. 5.7 shows the resistor array photo glued on HR surface mirror.

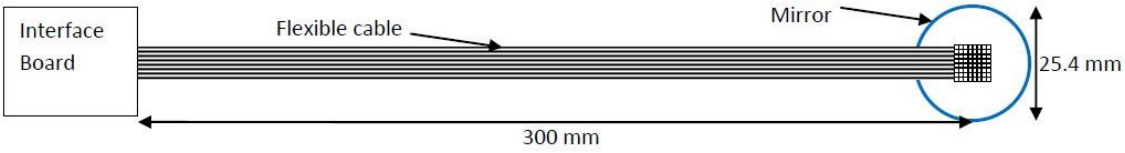

Figure 5.6: *Schematic diagram of setup*

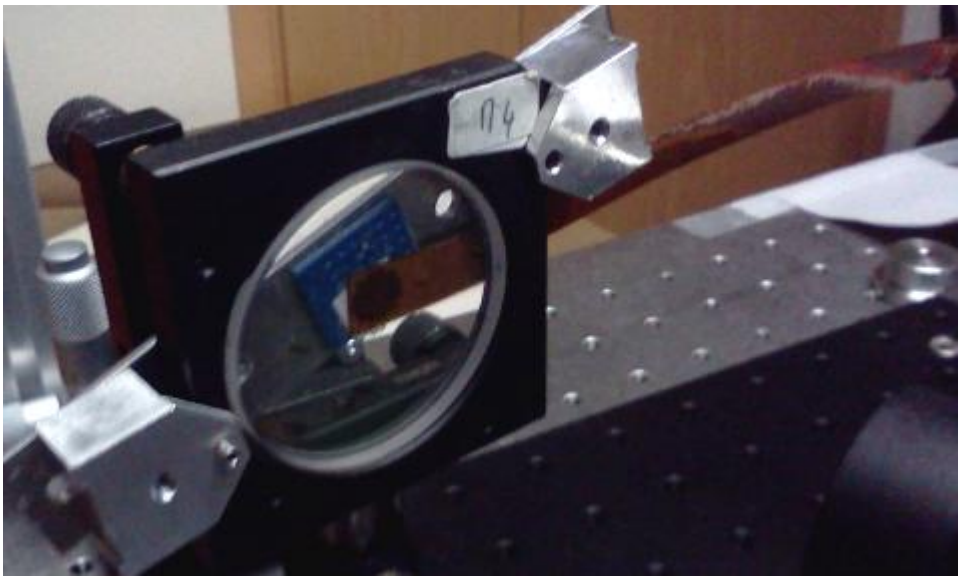

Figure 5.7: *TDM photo*

5.4 Characterization of TDM:

How previous said, the TDM could be an alternative technology to active optics to correct laser wavefront geometric distortions. However, it is necessary to be applicable that this system is required to be simple, efficient and low-cost.

The system simplicity is obvious, it consists exclusively of a mirror and resistors. Also regarding its cost, this is easy to evaluate:

(The Cost of a standard mirror) + (The Cost of cable with heating array)

The cost of "TDM board" is about 250 euro when bought in small quantity but it would cost around 10 euro in large quantity.
This is a very important feature if you think the cost of a generic deformable mirror.
To check the efficiency requirement, it is tested:

- System Linearity vs Power;
- System Stability;
- Measure Repeatability;
- System Response Superposition.

Efficiency evaluation of the heater resistor system gave good results.
So we go on to obtain an active system in remote control to compensate the geometric fluctuations of the beam.
The system is developed in the framework of Virgo experiment and has allowed to perform the first tests of the control beam wavefront.

5.4.1 *Experimental set-up*

The experimental set-up was formed by a Nd-Yag laser, emitting at 1064 nm, an beam expander to have a beam waist on the TDM greater than resistor array radius (4-5 mm), the TDM to characterize, a telescope and a Wavefront sensors for laser beam analysis (Phasics) mounted where it is formed the image of TDM. In Fig. 5.8(a) and 5.8(b) are shown respectively a scheme and a snapshot of the experimental

set-up. The laser power used to perform all the measurement, with this set-up, was

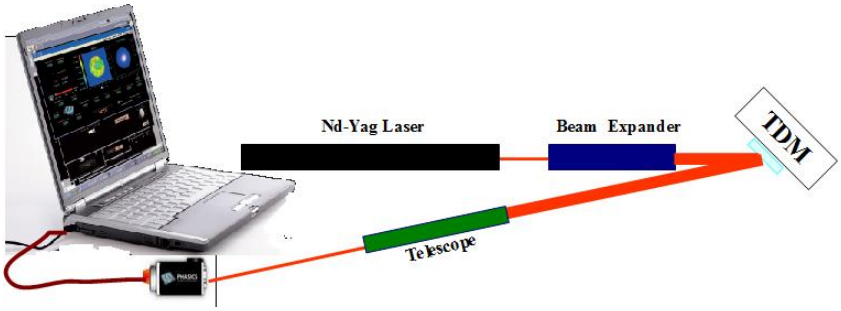

(a)

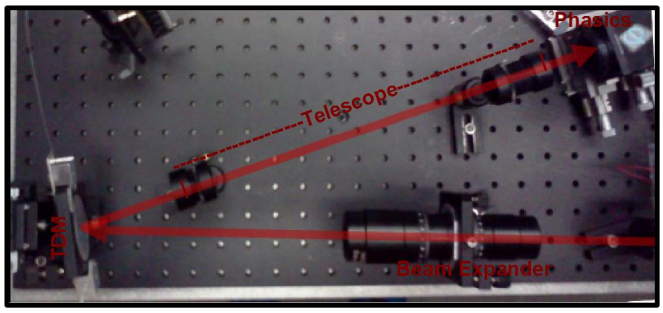

(b)

Figure 5.8: *Scheme and Photo of Experimental set-up used to TDM characterization.*

5 $\mu Watt$. The telescope was made by two lens with focus to 150 mm and 50 mm to have a magnification factor 1/3 to provide the camera eye read all beam. In Fig. 5.9, it can see a snapshot of the micro-array image on Phasics camera. At beginning, we have driven the TDM manually using a home-built interface board and a Voltage Generator while the test on more resistors turn on together and the test on wavefront correction were made in remote control.

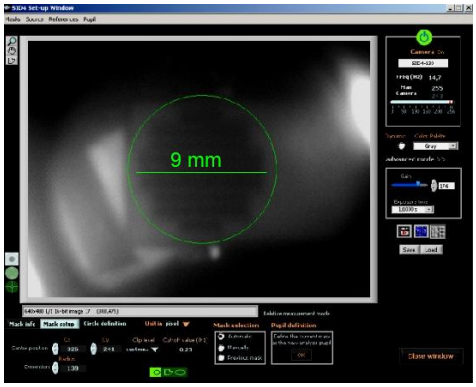

Figure 5.9: *Snapshot of the micro resistors array image on Phasics camera*

5.4.2 *A modified Hartmann test to measure wavefront distortions: Phasics^{TM} SID4*

To check the TDM efficiency to wavefront correction we need to know accurately the the global wavefront shape, so we need a common wavefront sensor.
The main commercially available wavefront sensor is the Shack-Hartmann sensor; it is composed of a micro-lens array that decomposes the incident wavefront, associated with a CCD sensor.
The main disadvantages of this sensor is the poor spatial resolution because the number of measurement points is limited by the number of micro-lenses.
Usually, in wavefront sensors with interferometric methods the spatial resolution is often better than in Shack-Hartmann because they are only limited by the CCD sensor resolution but, on the other hand, direct interferometry methods need a reference beam. An alternative is the multi-shearing interferometry, that doesn't need a reference beam and that offers the highest flexibility. So the proposed device for our application is a multi-lateral shearing interferometer from Phasics with a two dimensions diffraction grating (Phasics SID4).

Phasics^{TM} SID4 uses a 2D diffraction grating replicates the incident beam into 4 identical waves which are propagated along slightly different directions. The direction differences create interference patterns (see Fig. 5.10). After a few millimeter

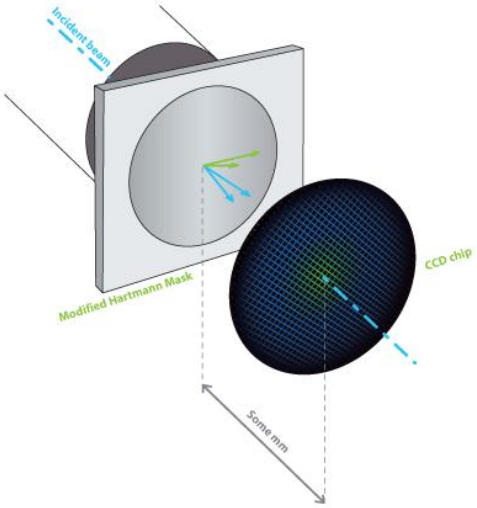

Figure 5.10: *SID4 wavefront sensor.*

propagation, the 4 beams are slightly separated. When aberrations are present on the beam, the interference grid is distorted. The grid deformations are directly connected to the phase gradients. A spectral analysis using Fourier transforms allows the phase gradient extraction in 2 orthogonal directions. The phase map is finally obtained by integration of these gradients. Finally, you get one measurement point per interferogram fringe.

5.4.3 *Introductory tests*

The first tests made were aimed at verifying the stability of the experimental set up used and at checking no loss of intensity in the TDM device.

Knowing that SID4 is very sensitive to environment vibrations as a preliminary test we have evaluated the stability of the wave front background profile, without heating the mirror, like saying the TDM device is taken off.

In the Fig. 5.11 it is shown the result obtained, we can conclude that there is a "background noise", the uncertainty in measurement is ± 20 *nm*. The test immedi-

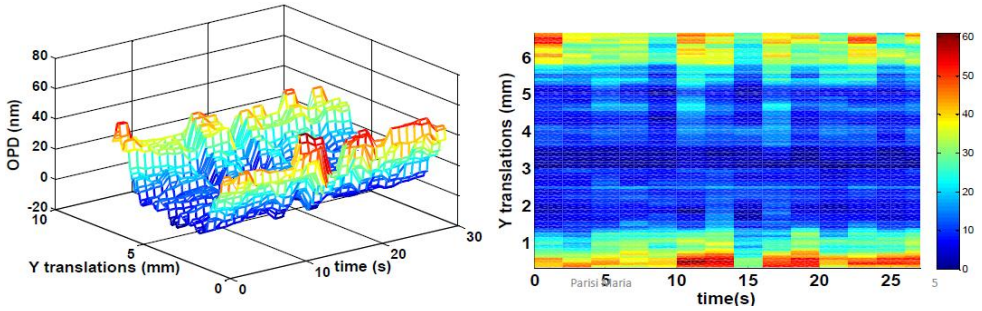

Figure 5.11: *Check of the OPD background stability:wavefront profile without heating the mirror.*

ately following was to verify the not intensity losses heating the mirror. Looking the Fig. 5.12, we can conclude that turn on a resistor there is no change in the intensity profile, so that we can say with the TDM device we we do not take the risk of power losses.

5.4.4 *Stability Measurement*

Subsequent to these initial tests, we went forward with measurements to check the stability of TDM device (see Fig. 5.13).

Therefore, a resistor of micro array is turned on by 10 V voltage. Looking the Fig. 5.13 we can conclude that there is a primary time of about caused by the temperature gradient and immediately after the wavefront becomes stable fixing the value of 230 ± 20 *nm*

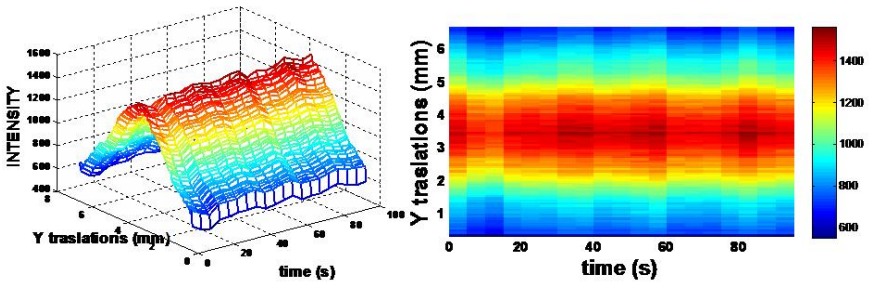

Figure 5.12: *Check of the no change in the beam intensity profile when the TDM plays.*

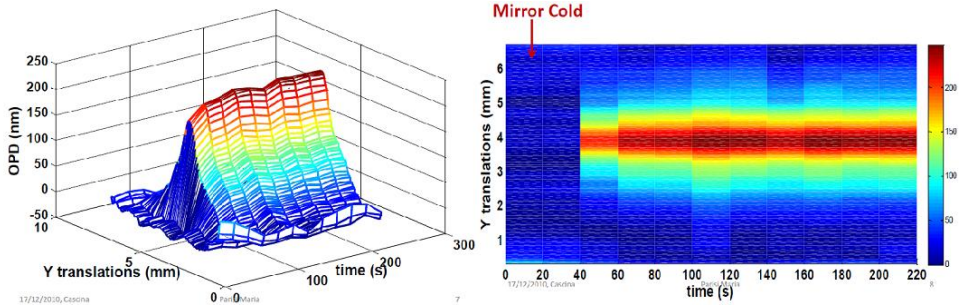

Figure 5.13: *TDM stability measurement.*

5.4.5 *Linearity Measurement*

The linearity of the TDM was estimated by applying a linear ramp signal to the driving electronic using the Voltage Generator.

In Fig. 5.14(a) it is shown how change punctually the wavefront when increase the Voltage across the resistor's terminals.

The Voltage was changed in the range $[1V, 10V]$ with 1 V steps, the curve obtained is shown in Fig. 5.14(b).

As we expected the Optical Path Difference (OPD) changes quadratically with the

Voltage while depends linearly by Power.

Of course, for no light (Power = 0 Watts) we can extrapolate the OPD value, remembering that the error on the measurements is given by laser own fluctuations, we can write $OPD(P = 0) \approx \ 10 \ \pm 20 \ nm$.

It was not possible to estimate the TDM non linearity because of intrinsic instability of laser beam.

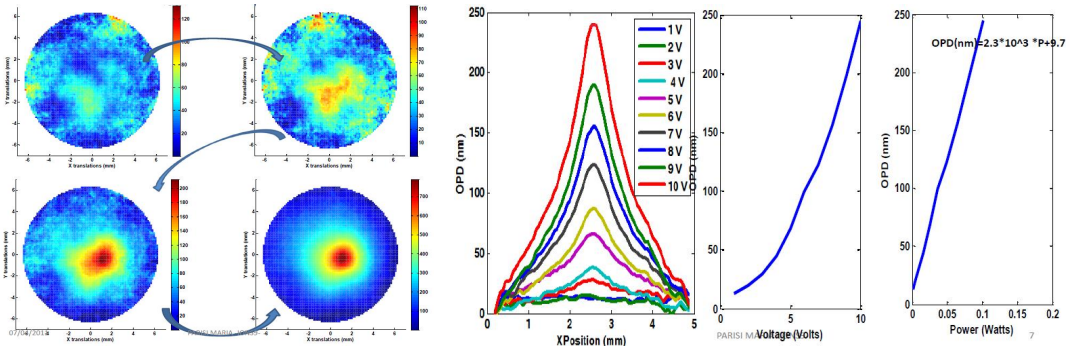

(a) (b)

Figure 5.14: *Wavefront change increasing the Voltage on the resistor(a) and Wavefront change along Y-translation, the change is quadratic vs voltage while it is linear vs power*

5.4.6 *Repeatability Measurement*

The repeatability of wavefront distortions caused by TDM is a crucial characteristic of this device, since it is involved with high precision wavefront shape that requires high performances in order to satisfy the requirements of the TDM applications.

This measurement gives a clear idea of the quality and repeatability of the issued positions.

In Fig. 5.15 an example of the measurement results is reported. It refers to the residual motion around the value of wavefront distortion, for a central resistor of

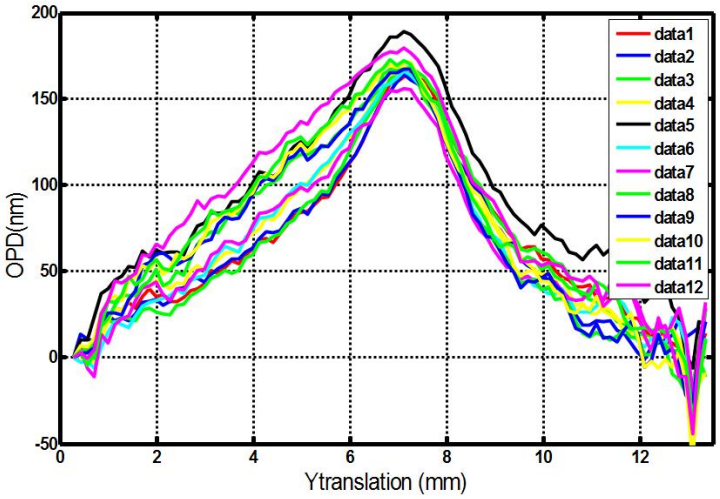

Figure 5.15: *Residual motion of the OPD around the value of wavefront distortion along the y axis obtained applying the same Voltage across a resistor.*

micro-array of $R = 962$ *ohms* and a Voltage of $V = 9V$.

Very similar results come from the same measurements performed with different actuators.

In this case too, the laser fluctuations are limiting the measurements so it is not possible to give any precise value about the repeatability measurements; we can only conclude that each measure can be repeated with an accuracy of $\leq \pm 20\ nm$.

5.4.7 *Linearity of Actuation Process*

Another measurement done to test the system efficiency it was to check the superposition principle for more actuators.

For this purpose, we have turn on separately two resistors R1 and R2 (Fig. 5.16(a)), these phase responses are summed. This wavefront image obtained is compared with the phase response obtained turning on R1 and R2 at the same time. The same

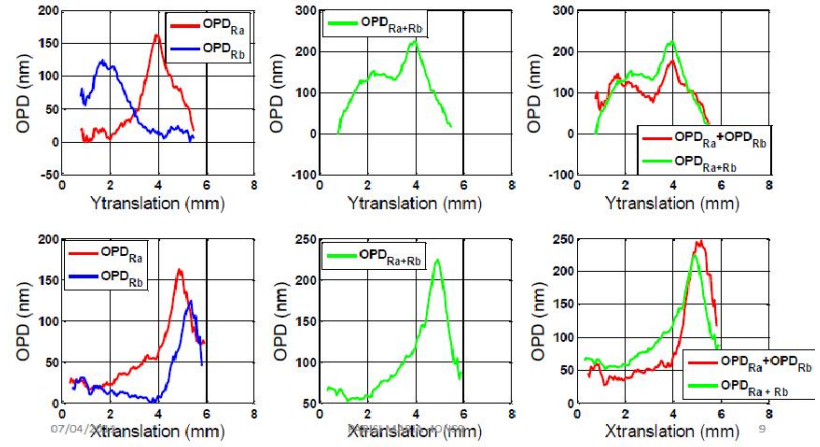

(a)

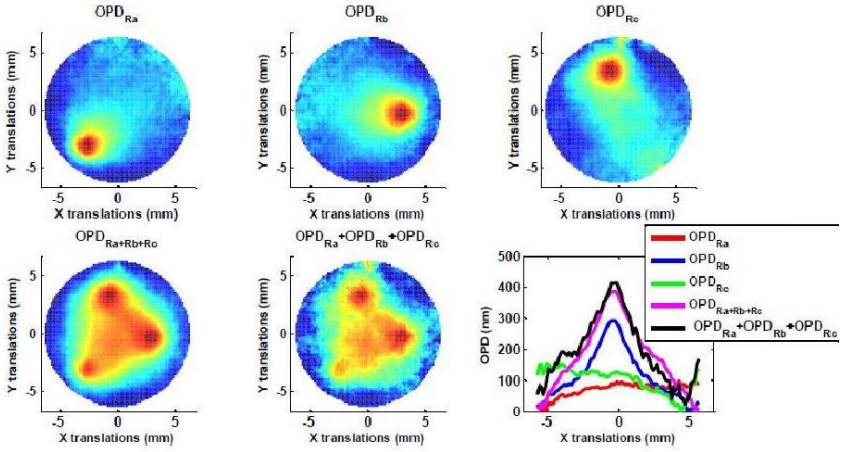

(b)

Figure 5.16: *Wavefront change with 2 or 3 resistors heated together*

it is done for three resistors (Fig. 5.16(b)). We can see that the system response caused by two or more resistors turned on is the sum of the responses which would have been caused by each resistor individually, concluding that the system response is linear.

5.5 Remote Control System and System Matrix Response

To control efficiently each resistor it was necessary to have a digitized signal to resistors. So, the commands are given by a DAC output and sent by a remote control system to the resistors. The correspondence between DAC channel and corresponding resistor and the correspondence between DAC channel and phase image deformed were established.

First, each resistor has been independently turned on at the same current of 5mA, with a voltage supply of 12V. Averaged phase images of each resistor have been collected (average of 15 images) (Fig. 5.17).

Second, a snapshot of the array image on the Phasics camera it was taken, so that it

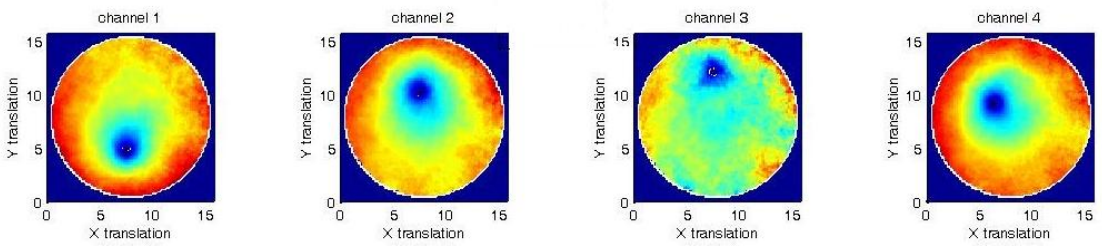

Figure 5.17: *Phase images obtained turning on independently each resistor by a remote control system.*

was possible determined the array position relative to the pupil (Fig. 5.18(a)) and final we identified the relation between the array position and phase image (Fig. 5.18(b)). From the results observed, it was deduced that some actuators are not

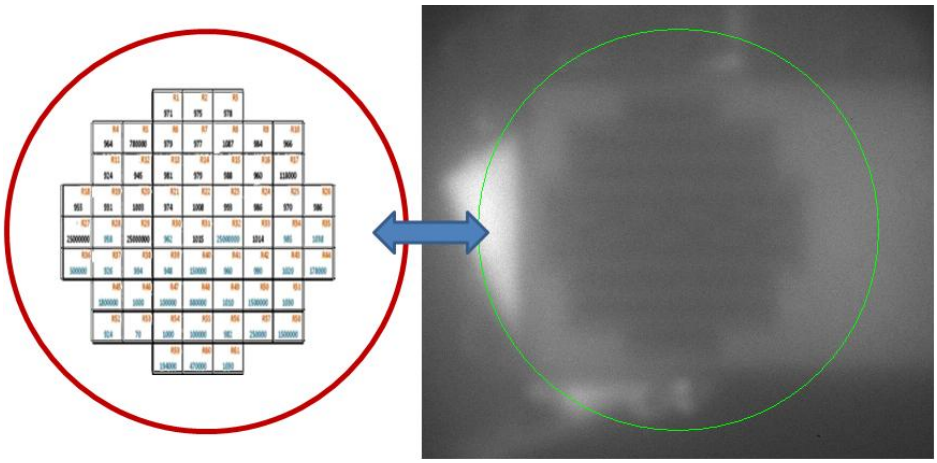

(a)

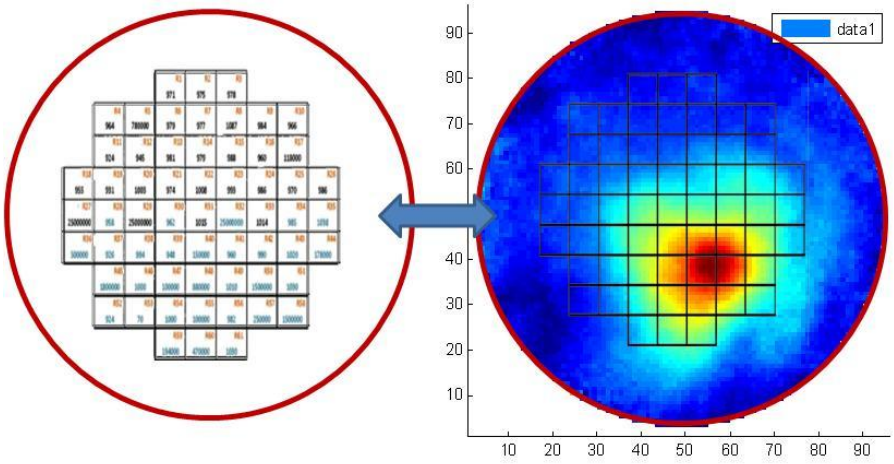

(b)

Figure 5.18: *Snapshot of the array image on the Phasics camera to determine the array position relative to the pupil and phase image to determine the array position relative to phase image modified by the actuators.*

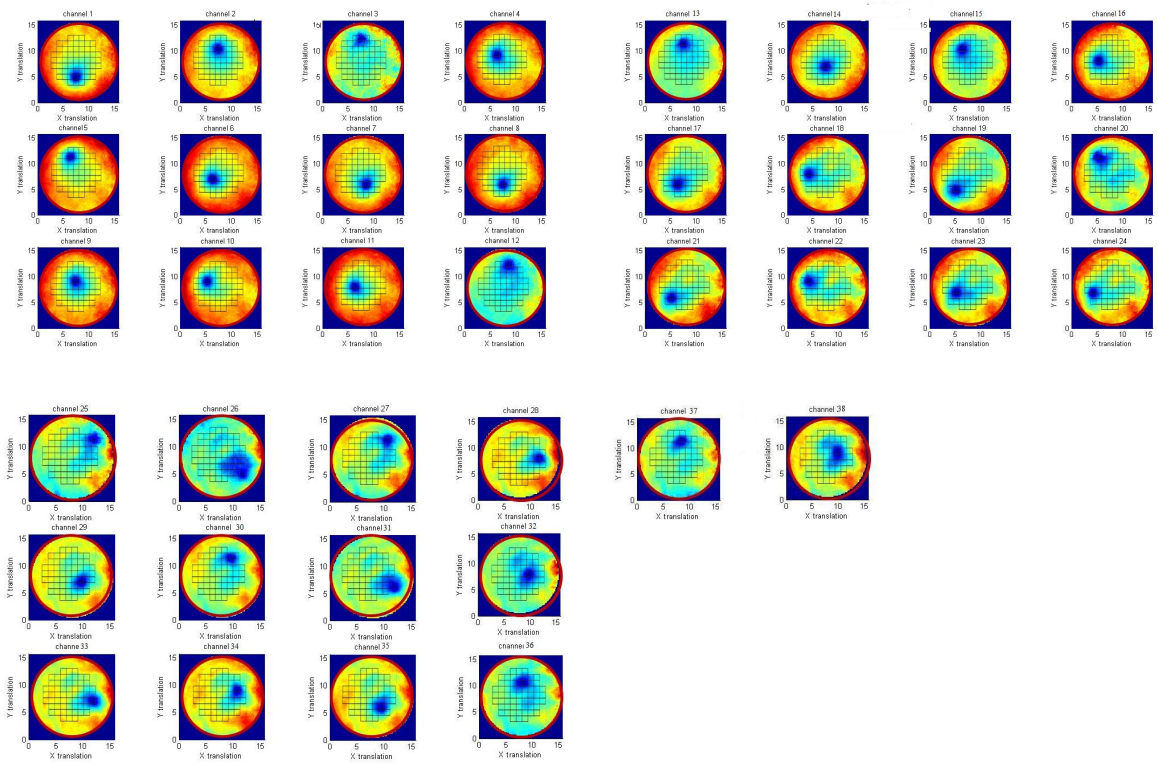

Figure 5.19: *Picture obtained for each DAC channel turned on*

working anymore due to manufacturing defects or previous destructive tests, furthermore some wavefront image was not sharp, it was probably due to a bad gluing resistors board to the mirror.

With this work, it was possible to identify a pictures set which characterizes the total system response. For each DAC channel exist a picture, remembering that exist a linear relation of wavefront vs power and that exist the wavefront superposition. We can obtain a wavefront as we like looking it as a superposition of feature cation, we can construct a picture library of system response for actuation of each resistor at the same level. The 38 influence functions of resistors which are working are presented in Fig. 5.19. It will be used to calculate the complete response of the system.

We can see that several influence functions have phase distortions on the whole pupil whereas the others are well defined. As all the resistors have been successively activated without doing the reference again at each time, it may come from a hysteresis effect of precedent actuations. This does not affect the identification protocol but it has to be investigated for the library construction.

5.6 TDM: results obtained

The device performance gives favorable implications for the use of such actuators in active compensation optical applications for the correction of static or slow wavefront deformations.

The TDM proves to give a linear response, after a mechanical response time of about 10 seconds the response seems to be very stable, the measurements were been repeatable and the superposed phase images of two different actuators switched on separately can be comparable with simultaneous application of two actuators.

Especially, the TDM seems to meet the requirements to be a good adaptive optics system for the input wavefront deformation compensation in Advanced Gravitational Waves Interferometers as Adv Virgo.

The TDM proves to be a deformable mirror with high quality mirror compatible, with high power laser compatible and a low cost system.

Conclusions

The present work has been carried out in the framework of the interferometric detection of gravitational waves (GW), specifically in the Virgo detector and in the Advanced Virgo (Adv-Virgo) project.
In particular, attention has been given to the mitigation of effect of laser beam perturbations in GWs detectors.
Virgo is near the design curve of sensitivity; to reach this condition the interferometer must work in condition of extremely precision, especially in terms of alignments. For example, the fluctuations in position and direction of the laser beam (beam jitter) are a critical technical noise source that can limit the dark fringe sensitivity.
The first part of the PhD work has been addressed to model analytically the all chain of beam jitter noise propagation from the laser to the set requirements for various sub systems and propose/test new improvements and up-grade of the detector. Starting from the Virgo optical layout, a preliminary step has been to evaluate how the seismic vibrations of the optical injection system are coupled to the TEM00 input beam. A second step has been to evaluate how these effects propagate in the main interferometer (ITF) and affect the dark-fringe carrying the GW signal. Moreover this study has contributed to set parameters and requirements to constrain a beam jitter noise to be compliant with Adv-Virgo sensitivity.
Studying the contribution of the external injection bench (EIB) angular and lateral

motions to the beam jitter, it is demonstrated that the noise is not negligible in Virgo and will yet be compliant with the requirements of Adv-Virgo. Indeed, the analysis carried out allows us to know that the "EIB" bench limits the jitter at the interferometer input to a value: $10^{-9}\ \frac{\mathrm{m}}{\sqrt{\mathrm{Hz}}}$ and $2*10^{-11}\ \frac{\mathrm{rad}}{\sqrt{\mathrm{Hz}}}$ around 40Hz; while the requirements obtained for Adv Virgo, evaluating the jitter transfer function of the interferometer, have been: $\tilde{y} \leq\ 10^{-11}\ \frac{m}{\sqrt{Hz}}$ and $\tilde{\theta} \leq 10^{-14}\ \frac{rad}{\sqrt{Hz}}$,(around 100Hz). So that, to be in accordance with Adv Virgo, it has been proposed to place the optical bench EIB on pneumatic isolation system to better isolate the bench from seismic noise, especially in the tens of Hz frequency region.

With an EIB suspended the amplitude of jitter at interferometer input will reduce by 1 or 2 factors around 10Hz and the peak around 40Hz will be attenuated.

Actually the NIKHEF group of Amsterdam works in progress to the suspension of EIB.

The second part of the PhD work, has been dedicated to the effects of thermal deformations of the Adv-Virgo injection optics.

In fact, in second generation of GW ITF, the use of high power laser (200W for project Advanced VIRGO) will cause a local heating and consequently a wavefront geometric deformation of the beam impinging on the interferometer.

In particular a new active system to control and correct the wavefront distortions has been performed that simultaneously meets the Adv-Virgo requirements: compatible with the vacuum, very stable, very high quality mirror and sustain high power laser. The system proposed has been a deformable mirror with an heater array used as actuator.

The system has shown encouraging performances in terms of efficiency, checking the system stability, linearity and measurements repeatability.

Appendix A

Phase relation at a mirror or beam splitter

This appendix is developed in order to define the notation used throughout the thesis.

The magnitude and phase of reflection at single optical surface can be derived from Maxwell's equations and imposing the boundary conditions required by the electromagnetic theory, namely the condition that the field amplitudes tangential to the optical surface must be continuous. The result is a set of equations that are solved to obtain relations between the incident, reflected and transmitted wave that are called Fresnel's equations [24].

$$r = \frac{n_1 - n_2}{n_1 + n_2} \tag{A.1}$$

with n_1 and n_2 the indices of refraction of the first and second medium, respectively. The transmission coefficient for a lossless surface can be computed as $t^2 = 1 - r^2$. We note that the reflection coefficient is always real and the phase change upon reflection depends on whether the second medium is optically thinner or thicker than the first ($n_1 < n_2$ phase shift π or $n_1 > n_2$ phase shift 0).

It can also shown that the phase change for the transmitted wave at a lossless surface is zero. This often contrasts with the common notation adopted for the analysis of modern optical systems.

Modern mirrors and beam splitters that make use of dielectric coatings are complex optical systems, whose reflectivity and transmission depend on the multiple interference inside the coating layers and thus on microscopic parameters. The phase change upon transmission or reflection depends on the details of the applied coating and is typically not known. In any case, the knowledge of an absolute value of a phase change is typically not of interest in laser interferometers because the absolute positions of the optical components are not known to sub-wavelength precision. Instead the relative phase between the incoming and outgoing beams is of importance.
The phase relation between the beams, can be derived from the fundamental principle of power conservation.

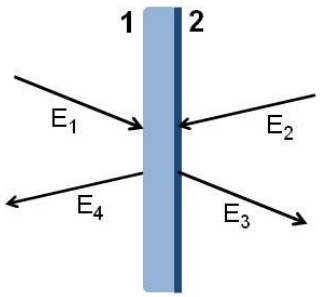

Figure A.1: *Partially reflected mirror.*

To do this we consider a mirror, as shown in Fig. A.1.
We assume that the magnitude of the reflection r and transmission t are known. The

phase changes upon transmission and reflection are unknown and might be different for either direction, thus, we write ϕ_{r_1} (ϕ_{t_1}) for the reflection (transmission)at the front and ϕ_{r_2} (ϕ_{t_2}) for the reflection (transmission)at the back of the mirror.
Then the electric fields can be computed as

$$E_3 = te^{i\phi_{t_1}} E_1 + re^{i\phi_{r_2}} E_2 \tag{A.2}$$

$$E_4 = te^{i\phi_{t_2}} E_2 + re^{i\phi_{r_1}} E_1 \tag{A.3}$$

Conservation of the total power requires that:

$$r^2 + t^2 = 1 - p$$

where p is the possible dissipation in the mirror.
If we consider the power balance.

$$|E_3|^2 + |E_4|^2 = (1-p)\left(|E_1|^2 + |E_2|^2\right) \tag{A.4}$$

This gives the following constraint on the phase factors:

$$(\phi_{r_1} + \phi_{r_2}) - (\phi_{t_1} + \phi_{t_2}) = (2n \pm 1)\pi \tag{A.5}$$

Due to symmetry we can say that the phase change upon transmission $\phi_{t_1} = \phi_{t_2} = \phi_t$ should be the same in both directions.

$$\frac{1}{2}(\phi_{r_1} + \phi_{r_2}) - \phi_t = (2n \pm 1)\frac{\pi}{2} \tag{A.6}$$

So that, the adopted notations are usually:

1. $\phi_t = 0$; $\phi_{r_1} = \pi$; $\phi_{r_2} = 0$
2. $\phi_t = \frac{\pi}{2}$; $\phi_{r_1} = \phi_{r_2} = 0$

Appendix B

Gaussian optics: Hermite-Gaussian Modes.

In this appendix section , the light is described by a scalar function $u(r,t)$, called the wavefunction, that obeys a second order differential equation known as the wave equation:

$$\nabla^2 u - \frac{1}{c^2}\frac{\partial^2 u}{\partial t^2} = 0 \tag{B.1}$$

the form of waves. In free space, light waves travel with speed $c = c_0$ while in a medium of refractive index n, light waves travel with a reduced speed $c = \frac{c_0}{n}$.
Any function satisfying Eq. (B.1) represents a possible optical wave.
Because the wave equation is linear, the principle of superposition applies; i.e., if $u_l(r,t)$ and $u_2(r,t)$ represent optical waves, then $u(r,t) = u_1(r,t) + u_2(r,t)$ also represents a possible optical wave.
We know that equation (B.1) would admit monochromatic wave solutions of the type:

$$u(r,t) = a(r)\cos\left[2\pi\nu t + \varphi(r)\right] \tag{B.2}$$

where:

$a(r)$ =amplitude

$\varphi(r)$ =phase

ν =frequency (cycles/s or Hz)

$\omega = 2\pi\nu$ = angular frequency (radians/s).

Both the amplitude and the phase are generally position dependent, but the wavefunction is a harmonic function of time with frequency ν at all positions.

It is convenient to represent the real wavefunction $u(r,t)$ in (B.1) in terms of a complex function

$$U(r,t) = a(r)\exp\left[j\varphi(r)\right]\exp\left(j2\pi\nu t\right) = U(r)\exp\left(j2\pi\nu t\right) \tag{B.3}$$

so that

$$u(r,t) = ReU(r,t) = \frac{1}{2}[U(r,t) + U*(r,t)] \tag{B.4}$$

The function $U(r,t)$, known as the complex wavefunction, describes the wave completely; the wavefunction u(r, t) is simply its real part. Like the wavefunction $u(r,t)$, the complex wavefunction $U(r,t)$ must also satisfy the wave equation,

$$\nabla^2 U - \frac{1}{c^2}\frac{\partial^2 U}{\partial t^2} = 0 \tag{B.5}$$

Substituting $U(r,t) = U(r)\exp(j2\pi\nu t)$ into the wave equation (B.5), we obtain the Helmholtz equation:

$$\left(\nabla^2 + k^2\right)U(r) = 0 \tag{B.6}$$

where $k = \frac{2\pi\nu}{c} = \frac{\omega}{c}$ it is the wavenumber.

The simplest solutions of the Helmholtz equation in a homogeneous medium are the plane wave and the spherical wave.

The plane wave has complex amplitude

$$U(r) = A\exp\left(-jk\cdot r\right) = A\exp\left[-j\left(k_x x + k_y y + k_z z\right)\right] \tag{B.7}$$

where A is a complex constant called the complex envelope and $k = (k_x, k_y, k_z)$ is called the wavevector. For Eq.(B.7) to satisfy the Helmholtz equation $k_x^2 + k_y^2 + k_z^2 = k^2$, so that the magnitude of the wavevector $\mathbf{k}$ is the wavenumber k.

The spherical wave is:

$$U(r) = \frac{A}{r} \exp(-jkr) \tag{B.8}$$

where r is the distance from the origin and $k = 2\pi\nu/c = \omega/c$ is the wavenumber. Taking $argA = 0$ for simplicity, the wavefronts are the surfaces $kr = 2\pi q$ or $r = q\lambda$, where q is an integer. These are concentric spheres separated by a radial distance $\lambda = 2\pi/k$.

A wave is said to be paraxial if its wavefront normals are paraxial rays.

One way of constructing a paraxial wave is to start with a plane wave $A\exp(-jkz)$, regard it as a "carrier" wave, and modify or "modulate" its complex envelope A, making it a slowly varying function of position $A(r)$ so that the complex amplitude of the modulated wave becomes:

$$U(r) = A(r)exp(-jkz) \tag{B.9}$$

For a paraxial wave (Eq. B.9), to satisfy the Helmholtz equation, the complex envelope $A(r)$ must satisfy another partial differential equation obtained by substituting (B.9) into (B.6). The assumption that $A(r)$ varies slowly with respect to z signifies that within a distance $\Delta z = \lambda$, the change ΔA is much smaller than A itself, i.e., $\Delta A << A$. This inequality of complex variables applies to the magnitudes of the real and imaginary parts separately. Since $\Delta A = (\partial A/\partial z)\,\Delta z = (\partial A/\partial z)\,\lambda$, it follows that $\partial A/\partial z << A/\lambda = Ak/2\pi$, so that:

$$\frac{\partial A}{\partial z} << kA \tag{B.10}$$

The derivative $\partial A/\partial z$ itself must also vary slowly within the distance λ, so that $\partial^2 A/\partial z^2 << k\partial A/\partial z$, which proviedes:

$$\frac{\partial^2 A}{\partial z^2} << k^2 A \tag{B.11}$$

Substituting (B.9) into (B.6) and neglecting $\frac{\partial^2 A}{\partial z^2}$ in comparation with $k\frac{\partial A}{\partial z}$ or $k^2 A$, leads to a partial differential equation for the complex envelope A(r):

$$\nabla_T^2 A - j2k\frac{\partial A}{\partial z} = 0 \tag{B.12}$$

We shall simply call it the **paraxial Helmholtx equation**.

The most simplest solution of paraxial Helmholtx equation is the **paraboloid wave**, $A(r) = \frac{A_1}{z}\exp\left(-jk\frac{\rho^2}{2z}\right)$ ($\rho = x^2+y^2$) while the most useful solution is the **Gaussian beam**.

$$A(r) = \frac{A_1}{q(z)}\exp\left(-jk\frac{\rho^2}{2q(z)}\right) \tag{B.13}$$

This represents a paraboloid wave centered about the point $z = \xi = -jz_0$ and where, $q(z) = z - \xi$ is called the **q-parameter** and z_0 is known as the **Rayleigh range** (Fig. B.1).

To separate the amplitude and phase of this complex envelope, we write the complex function $1/q(z) = 1/(z + jz_0)$ in terms of its real and imaginary parts by defining two new real functions, $R(z)$ and $W(z)$, such that:

$$\frac{1}{q(z)} = \frac{1}{R(z)} - j\frac{\lambda}{\pi W^2(z)} \tag{B.14}$$

$W(z)$ and $R(z)$ are measures of the beam width and wavefront radius of curvature. So, the complex amplitude $U(r)$ of the Gaussian beam is:

$$\begin{aligned} U(r) &= A_0\frac{W_0}{W(z)}\exp\left[-j\frac{\rho^2}{2q}\right]\exp\left[-jkz\right]\exp\left[j\varsigma(z)\right] \\ &= A_0\frac{W_0}{W(z)}\exp\left[-\frac{\rho^2}{W^2(z)}\right]\exp\left[-jkz - jk\frac{\rho^2}{2R(z)} + j\varsigma(z)\right] \end{aligned} \tag{B.15}$$

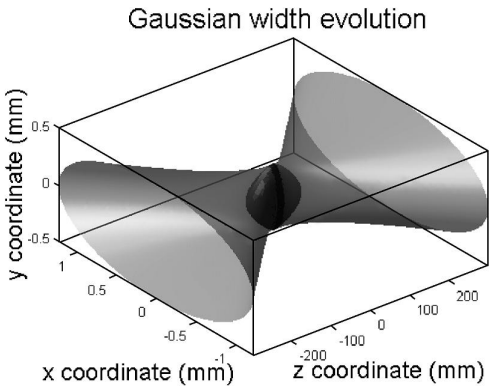

Figure B.1: *A 3-D representation of the evolution of the Gaussian width.*

where:

$$A_0 = \frac{A_1}{jz_R} \qquad W(z) = W_0\sqrt{1+\left(\frac{z}{z_R}\right)^2}$$

$$R(z) = z\left[1+\left(\frac{z_R}{z}\right)^2\right] \qquad \varsigma(z) = \tan^{-1}\left(\frac{z}{z_R}\right) \qquad W_0 = \sqrt{\frac{\lambda z_R}{\pi}}$$

Up to this point, we considered a single solution of the paraxial wave equation, namely the fundamental Gaussian mode. Other solutions, mathematically forming an orthonormal and complete base, exist. Each oscillation in the resonator is a linear combination of those modes. Their transverse structures have a rectangular, cylindrical, or a mix of them symmetry : it is mainly defined by the mirrors shape (rectangular or circular). This structure is in general strongly affected by other perturbations and cannot be observed so easily.

Let's start with the modes having a rectangular geometry in a Cartesian coordinates

system. We can then write a solution of the wave equation as follows :

$$\psi(x,y,z) = g\left(\frac{x}{w}\right) h\left(\frac{y}{w}\right) \exp -i\left[\Delta\phi\left(z\right) + \frac{k}{2q\left(z\right)}\left(x^2+y^2\right)\right] \tag{B.16}$$

where g (respectively h) is a function of z and x (respectively z and y).

The insertion of this solution inside the paraxial wave equation leads to a differential equation for g and h; the solutions of this equation are Hermite's polynomials.

One can show (not demonstrated here) than a complete set of solutions is :

$$\psi_{n,m}(x,y,z) = \sqrt{\frac{2}{\pi}\frac{1}{2^{n+m}n!m!}}\frac{1}{\omega(z)}H_n\left(\frac{x\sqrt{2}}{\omega(z)}\right)H_m\left(\frac{y\sqrt{2}}{\omega(z)}\right)e^{-i(kz-\phi_{n,m})}e^{-ik\frac{x^2+y^2}{2q}} \tag{B.17}$$

where :

m, n are integers

q, R et w were already defined for Gaussian beams

$\phi(z) = (m+n+1)\arctan\left(\frac{\lambda z}{\pi w_0^2}\right)$ is the Gouy phase shift

$H_n(X)$ are the Hermite ploynomials

As an example : $H_0(X) = 1$, $H_1(X) = 2X$, $H_2(X) = 4X^2 - 2$ etc.

For m = n = 0, we have the fundamental Gaussian beam.

So that:

$$\psi_{00}(x,y,z) = \left(\frac{2}{\pi\omega_0^2}\right)^{1/2} e^{-\frac{x^2+y^2}{\omega^2(z)}}$$

$$\psi_{10}(x,y,z) = \left(\frac{2x}{\omega_0}\right)\psi_{00}(x,y,z)$$

$$\psi_{01}(x,y,z) = \left(\frac{2y}{\omega_0}\right)\psi_{00}(x,y,z)$$

These relations are useful in deriving the spatial distributions of beams misaligned with respect to optical axis.

For any m and n, the propagation law for R, q and w remains the same. Only the

phase shift and the transverse beam structure differ. The figures B.2(a) and B.2(b) depict the intensity pattern for those modes. One can notice some "'zeros"' for the intensity (dark lines) : their number correspond to the order m.

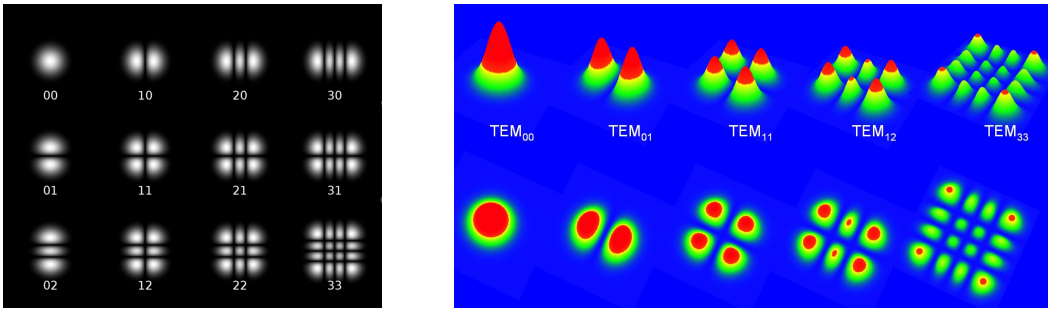

(a) (b)

Figure B.2: *Spatial energy distribution for Hermite-Gaussian modes in 2D (a) and 3D (b) presentation.*

The phase-shift after one round trip in a two mirrors resonator has to be equal to q times (q is an integer). Starting from the phase expression and using the same method as in previous paragraph we obtain the following expression for the frequency of the TEM_{mnq} mode:

$$\nu_{nmq} = \frac{c}{2d}\left[q + \frac{1}{\pi}(m+n+1)\arccos\left(\pm\sqrt{(g_1 g_2)}\right)\right] \tag{B.18}$$

If the resonator symmetry is mostly circular, the modes exhibit a cylindrical symmetry described by the Laguerre polynomials. The mathematical method is the same as the one described for Hermite-Gaussian modes. The figure B.3 describe the intensity distribution for such modes.

The frequency of the TEM_{plq} mode:

$$\nu_{plq} = \frac{c}{2d}\left[q + \frac{1}{\pi}(2p+l+1)\arccos\left(\pm\sqrt{(g_1 g_2)}\right)\right] \tag{B.19}$$

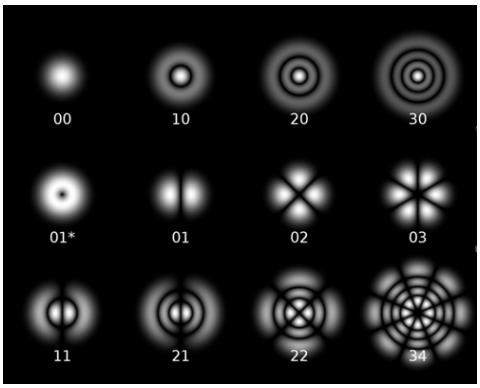

Figure B.3: *Spatial energy distribution for Laguerre-Gaussian modes.*

A steady-state field distribution oscillating inside the resonator is called an eigenmode of the resonator. The eigenmodes are characterized by the transverse mode structure (transverse mode index p, l or m,n) and the axial mode order q. The notations for the eigenmodes are

$$T_{plq} \qquad \text{and} \qquad T_{mnq} \tag{B.20}$$

where the abbreviation TEM represents the fact that the electric and the magnetic field vectors are perpendicular to each other and to the wave vector R (Transverse Electro Magnetic).

In both symmetries the TEM_{00} mode has the same shape; the intensity distribution is Gaussian.

As mentioned above, the resonance frequencies thus depend on both the axial and the transverse mode order. In contrast to the plane-parallel ($g_1 = g_2 = 1$) whose resonance frequencies are only determined by the axial mode index, each axial mode

of stable resonators is subdivided into a sequence of frequencies corresponding to different transverse modes. This separation is controlled by the g-parameters of the resonator mirrors. As the origin of the g-diagram is approached, the frequency gap between different transverse modes having the same axial mode order becomes wider. In the limit of the stable confocal resonator ($g_1 = g_2 = 0$), the frequency gap equals $c_0/(4d)$ which is half the axial mode distance. The confocal resonator exhibits frequency degeneracy which means that all modes meeting the conditions $2q + 2p + l + 1 = k$ and $2q + m + n + 1 = k$, with k : integer, oscillate at the same resonance frequency $kc_0/(4d)$.

Appendix C

A tilted and displaced Gaussian beam

The x- and y- axes of the coordinate system are chosen to be transverse to the beam propagation (and optical axis) of the perfectly aligned and undistorted system (z-axis). We start with a field spatially described by a zero-order Hermite-Gaussian mode, if the beam axis is the same of the optical axis, the amplitude at distance x from the z-axis is given by:

$$\psi = \sqrt{\frac{2P_{in}}{\pi w_0^2}} e^{-\frac{x^2+y^2}{w_o^2}} \tag{C.1}$$

When ψ is laterally displaced in the positive x-direction by a small amount a and in the positive y-direction by a small amount b, as in figure C.1), we get:

$$\psi = \sqrt{\frac{2P_{in}}{\pi w_0^2}} e^{-\frac{(x-a)^2+(y-b)^2}{w_o^2}} \tag{C.2}$$

A tilted beam that makes the angles φ and ϑ with respect to the cavity axes (Fig. C.2), for small φ and ϑ can be described by:

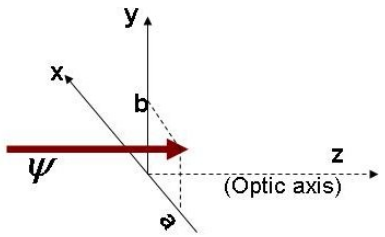

Figure C.1: *Beam displacement respect to cavity axis.*

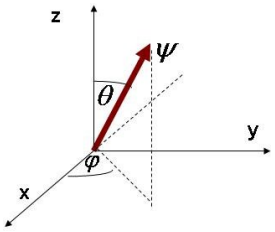

Figure C.2: *Beam tilt respect to cavity axis.*

$$\psi = \sqrt{\frac{2P_{in}}{\pi w_0^2}} e^{-\frac{x^2+y^2}{w_o^2}} e^{-ik(\alpha x+\beta y)} \tag{C.3}$$

where: $\alpha = \sin\vartheta\cos\varphi$ and $\beta = \sin\vartheta\sin\varphi$.

In order to calculate the effects of laser jitter, the function ψ can be expanded to first-order in $a, b, \alpha, \beta \approx 0$.

$$\psi_{in} = \sqrt{\frac{2P_{in}}{\pi w_0^2}} e^{-\frac{x^2+y^2}{w_o^2}} \left\{1 + 2\frac{x}{w_o^2}a + 2\frac{y}{w_o^2}b - ik\alpha x - ik\beta y\right\} \tag{C.4}$$

If we call $\alpha_0 = \beta_0 = \frac{k\omega_0}{2} = \frac{\pi\omega_0}{\lambda}$, with λ laser wavelength and if we refer to Hermite-Gauss modes which are listed in Appendix B, we can note that:

$$\psi_{in} = \sqrt{P_{in}} \left\{\psi_{00} + \left(\frac{a}{w_0} - i\frac{\alpha}{\alpha_0}\right)\psi_{10} + \left(\frac{b}{w_0} - i\frac{\beta}{\beta_0}\right)\psi_{01}\right\} \tag{C.5}$$

So that a misaligned beam can then be described, in one degree of freedom and

in $z = z_0$, as a column vector:

$$\psi_{in} = \sqrt{P_{in}} \begin{pmatrix} \psi_0 \\ a_1 \cdot \psi_1 \end{pmatrix} \tag{C.6}$$

where a_1 is the amplitude of first order mode ψ_1, given by $a_1 = \hat{a} + i\hat{\alpha}$, with:

$$\hat{a} = \frac{a}{w(z_0)} \left(1 + i\frac{z_0}{z_R}\right) \qquad \hat{\alpha} = \alpha \frac{\pi w(z_0)}{\lambda} \tag{C.7}$$

Appendix D

Mode decomposition

In this section, we present a formalism which can be used to study the problem of misalignment in the GW interferometer, with the goal of characterization the sensitivity of the detector to angular misalignment.
In particular a field circulating in the misaligned or distorted optical system is decomposed in to a superposition of the eigenmodes of the unperturbed system; the scale of the imperfections determines the number of eigenmodes needed for an accurate description.

$$\psi(x, y, z) = \sum q_{nm}\psi_{nm} \tag{D.1}$$

Misaligned or distorting optical components are represented as operators in the basis of these eigenmodes: $M(x, y, z_2, z_1)$; the transformation of a field of a misaligned or distorted optical system at position z_1 in to a field at position z_2 is given:

$$\psi(x, y, z_2) = M(x, y, z_2, z_1)\psi(x, y, z_1) \tag{D.2}$$

the representation $M_{nm,kl}(z_2, z_1)$ of $M(x, y, z_2, z_1)$ in the modal space can be written as:

$$M_{mn,kl}(z_2, z_1) = \int\int_{\infty}^{-\infty} \psi^{+}_{mn}(x, y, z_2)M(x, y, z_2, z_1)\psi_{kl}(x, y, z_1)dxdy \tag{D.3}$$

where the functions $\psi_{mn}(x, y, z)$ are the eigenmodes of the unperturbed system. To simplify the calculation we go to separate the longitudinal propagation from misalignment and distortion effects caused by lenses and mirrors, which affect the wavefront at a fixed longitudinal position.

In the Hermite-Gaussian basis the propagator simplifies to

$$L_{mn,kl}(\phi_{mn}) = \delta_{mk}\delta_{nl}e^{-ik(z_2-z_1)}e^{i(\phi_{mn}(z_2)-\phi_{mn}(z_1))} \tag{D.4}$$

where $\phi_{mn}(z_2)-\phi_{mn}(z_1)$ is the Guoy phase shift. The propagator is the only operator which retains a significant z-dependence. Hence, for lenses and mirrors Eq. D.3 reduces to

$$M_{mn,kl} =< mn|M(x, y)|kl > \tag{D.5}$$

where the bra-ket-product is defined as the integration over the transverse degrees of freedom and where $< mn|$ and $|kl >$ are the Gaussian eigenmodes.

Let us consider a slightly misaligned mirror, spatial variations over the mirror surface cause each part of the wavefront acquires an additional phase shift due to a local displacement in the z-direction (see Fig. D.1). If all deviations from the ideal surface are contained in the function $Z(x, y)$, the mirror distortion operator can then be written as

$$M(x, y) = e^{-2ikZ(x,y)} \tag{D.6}$$

To obtain the true reflected field of the mirror one has to multiply the right hand side of Eq. (D.6) by the reflection coefficient.

The distortion operator which describes reflection from the rear surface of the mirror is given by:

$$M(x, y)_{rear} = e^{2ikZ(x,y)} = M(x, y)^{-1} \tag{D.7}$$

If is a real function, these operators are unitary and, thus, conserves energy. The

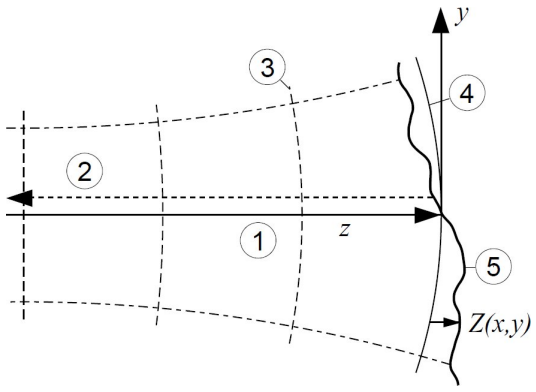

Figure D.1: *Reflection on an imperfect and misaligned mirror surface. 1) direction of incoming laser beam, 2) reflected beam, 3) undistorted wavefront, 4) ideal mirror surface, 5) physical mirror surface and Z(x,y) deviation from ideal mirror surface.*

modal space representation then becomes:

$$M_{mn,kl} =< mn|e^{-2ikZ(x,y)}|kl >=< mn| \exp\left(-2ik \sum |op > Z_{op,qr} < qr|\right)|kl > \tag{D.8}$$

Expanding Z(x,y) in a series of orthonormal polynomials H_i

$$-2kZ(x,y) = \sum_{i,j} c_{ij} H_i\left(\sqrt{2}\frac{x}{w(z)}\right) H_j\left(\sqrt{2}\frac{y}{w(z)}\right) \tag{D.9}$$

one obtains:

$$-2kZ_{op,qr} = 2\sum_{1,j} c_{ij} T^{ij}_{op,qr} = \sum_{1,j} c_{ij} < op|H_i(x)H_j(y)|qr > |_{z=0} \tag{D.10}$$

For a small rotation about the y-axis Z(x,y) can be written as $Z(x,y) = \theta_x x$. By substituting $\Theta = \theta\pi w(z)/\lambda$ which is the normalized rotation angle, the operator becomes:

$$-2kZ(x,y) = -\sqrt{8}\Theta_x \frac{\sqrt{2}x}{w(z)} = -\sqrt{2}\Theta_x H_1\left(\frac{\sqrt{2}x}{w(z)}\right) \tag{D.11}$$

In the Hermite-Gaussian basis, the recursion relationship for the Hermite polynomials simplifies the generator T_{10} to

$$T^{10}_{op,qr} = \frac{1}{\sqrt{2}}\delta_{pr}\left(\sqrt{q}\delta_{o,q-1} + \sqrt{o}\delta_{o,q+1}\right) \tag{D.12}$$

For small misalignments the only important modes are the fundamental TEM_{00} mode and the lowest order transverse (Hermite-Gaussian) modes, TEM_{10} and TEM_{01}. Using the notation where all three modes are the components of a single vector, an electromagnetic field in modal space can be written as:

$$\psi = \begin{pmatrix} \psi_{00} \\ \psi_{10} \\ \psi_{01} \end{pmatrix} \tag{D.13}$$

Making use of eqs. (D.4) and (D.12) and including terms to first order in and only [17], the propagator and the mirror misalignment matrices become

$$L(z_2 - z_1) = e^{-ik(z_2-z_1)} \begin{pmatrix} e^{i\eta} & 0 & 0 \\ 0 & e^{i2\eta} & 0 \\ 0 & 0 & e^{i2\eta} \end{pmatrix} \quad M(\Theta_x, \Theta_y) = \begin{pmatrix} 1 & -i2\Theta_x & -i2\Theta_y \\ -i2\Theta_x & 1 & 0 \\ -i2\Theta_y & 0 & 1 \end{pmatrix} \tag{D.14}$$

with $\eta = \eta(z_2) - \eta(z_1) = \arctan\sqrt{\frac{z_2}{z_R}} - \arctan\sqrt{\frac{z_1}{z_R}}$.
The above technique can be applied to study the problem of misalignment in each optical system.

Bibliography

[1] P. J. Sutton, *Searching for gravitational waves with LIGO* J. Phys.: Conf. Ser., 2008 (110) 062024

[2] The Virgo Collaboration, *Advanced Virgo Baseline Design* Virgo document, 2009 , https://tds.ego-gw.it/ql/?c=6589

[3] G. M. Harry (for the LIGO Scientific Collaboration), *Advanced LIGO the next generation of gravitational wave detectors* Class. Quant. Grav., 2010 (27) 084006

[4] S.Capozziello, M. Funaro, *Introduzione alla Relativita' Generale* Napoli (1995)

[5] S. Weinberg, *Gravitation and cosmology*: principles and applications of the general theory of Relativity, john wiley-Sons, New York (1972).

[6] C.W. Misner, K.S. Thorne, J. Wheeler, *Gravitation*, W. H. Freeman, San Francisco (1973).

[7] C. Moller, *The theory of relativity*, Oxford University Press, New Delhi (1972).

[8] R.M. Wald, *General relativity*, The University of Chicago Press, Chicago, (1984).

[9] R.A. Hulse and J.H. Taylor, Astrophys. J. **191** , L59-L61 (1974).

[10] R.A. Hulse and J.H. Taylor, Astrophys. J. *Discovery of a pulsar in a binary system* **195** , L51-L53 (1975).

[11] R.A. Hulse and J.H. Taylor, Astrophys. J. **201** , L55-L59 (1975).

[12] J.H Taylor, *Noble lecture : Binary Pulsars and Relativistic Gravity* Rev. Mod. Phys. , 711-719 (1994).

[13] Einstein, A.: *Naherungsweise Integration der Feldgleichungen der Gravitation.* In: Sitzungsberichte der Koniglich Preussischen Akademie der Wissenschaften Berlin (1916), 688-696.

[14] K. S. Thorne, C. W. Misner and J. A. Wheeler, *Gravitation*, W. H. Freeman publisher (1973)

[15] R. M. Wald, *General Relativity*, University Of Chicago Press (1974)

[16] B.F. Shutz, Nature 323, 310 (1986).

[17] A. Abramovici,W.E. Althouse, R.W.P. Drever, Y. Gürsel, S. Kawamura, F.J. Raab, D. Shoemaker, L. Sievers, R.E. Spero, K.S. Thorne, R.E. Vogt, R. Weiss, S.E. Whitcomb and M.E. Zucker, Science 256, 325-333 (1992).

[18] D.G. Blair, *The detection of gravitational waves*, Cambridge U. Press, Cambridge (1991).

[19] P.R. Saulson, *Fundamentals of Interferometric Gravitational Wave Detectors*, World Scientific (1994)

[20] A. Abramovic et al., *LIGO : The Laser Interferometer Gravitational − Wave Observatory Science* 256, 325 (1992).

[21] A. Brillet, A. Giazotto et al., *The VIRGO Project Final Conceptual Design of the French–Italian Interferometric Antenna for Gravitational Wave Detection*, unpublished (1992).

[22] H.B.Callen, T.A.Welton, *Irreversibility and Generalized Noise*, Phys. Rev., 83 (1), 34-40 (1951)

[23] M. Lorenzini and the Virgo Collaboration,*The monolithic suspension for the Virgo interferometer*, Class. Quantum Grav., 2010 (27) 084021

[24] Kenyon, I.R., *The Light Fantastic: A Modern Introduction to Classical and Quantum Optics*, (Oxford University Press, Oxford; New York, 2008).

[25] Cleva; *Pre Mode Cleaner completion (virchrq0022006)*, VIRGO+ 2nd Review Document.

[26] A. E. Siegman; *Lasers* (1986), ed. University Science Books, Mill Valley, California.

[27] E. Calloni, N. Man, H. Nguyen, *Spatial Filtering Properties of Mode Cleaner*, Virgo Note: VIR-NOT-NAP-1380-44.

[28] Guido Mueller, *Beam jitter coupling in advanced LIGO*, Optical Society of America,2005.

[29] V. Mandic, *Estimate of the Beam Jitter at the Output Mode Cleaner*, Ligo Note: LIGO-T060178-00-D.

[30] Peter Fritschel, *Misalignment-Beam Jitter Coupling in LIGO*, Ligo Note: LIGO-T960120-00-D.

[31] Yaron Hefetz, Nergis Mavalvala, Daniel Sigg, *Principles of calculating alignment signals in complex resonant optical interferometers*, Ligo Note: LIGO-P960024-A-D.

[32] Daniel Sigg and Nergis Mavalvala, *Principles of calculating the dynamical response of misaligned complex resonant optical interferometers*, Ligo Note: LIGO-P990005-C-D.

[33] Guido Mueller, *Effect of mirror misalignments on optical ray path in a ring resonator*, Journal of the Optical Society of Korea, Vol. 6,No. 3, September 2002.

[34] Guido Mueller, *Pointing requirements for Advanced LIGO*, Ligo Note: LIGO-T0900142_V2.

[35] Rich Abbott, Rana Adhikari, Stefan Ballmer, Lisa Barsotti, Matt Evans, Peter Fritschel, Valera Frolov, Guido Mueller, Bram Slagmolen, SamWaldman, *AdvLIGO Interferometer Sensing and Control Conceptual Design*, Ligo Note: LIGOT070247-01-I.

Acknowledgments

I would like to express my gratitude to my supervisor, Dr. Enrico Calloni, for having offered me the opportunity of coming to the Virgo and working on an exciting research project, that after three years finally culminated in this Thesis.
A special tanks is for the Prof. Leopoldo Milano for his encouragement.
I would like to thank the other members of the Virgo group of Naples, in particular Rosario De Rosa, Fabio Garufi, Mariafelicia De Laurentis, Luciano Di Fiore and in particular way Simona Mosca and Luca Forte for the amount of time and energy that you invested in guiding me throughout this work, your support in the most critical moments, the many enriching scientific discussions.
Furthermore, I would also like to thank the whole EGO team: Eric Genin, Benjamin Canuel, Daniel Sentenac, Antonino Chiummo, Gabriele Vajente, Richard Day and Marie Kasprzack. I am especially grateful to Julien Marque whose expertise, understanding, and patience, added considerably to my experience.
I would also like to thank my parents and my sisters for the support they provided me through my entire life and in particular.
I must acknowledge my husband, Fabio, without whose love, encouragement and editing assistance, I would not have finished this thesis and I would not have started this new adventure that awaits us and that appears very hard but also exciting!